SEARCH FOR RADIO PULSARS IN SUPERNOVA REMNANTS

A THESIS SUBMITTED TO THE UNIVERSITY OF MANCHESTER

FOR THE DEGREE OF MASTER OF SCIENCE

IN THE FACULTY OF SCIENCE AND ENGINEERING

March 2019

By

Susmita Sett

School of Physics and Astronomy

Contents

Abstract 9

Declaration 10

Copyright 11

Acknowledgements 13

1 Introduction 15

1.1 Discovery of pulsars . . . 17

1.2 What are pulsars? . . . 18

1.3 The journey of pulsars . . . 20

1.4 Main properties of pulsars . . . 23

1.4.1 Spin evolution . . . 23

1.4.2 Braking index and age estimate . . . 23

1.4.3 Magnetic field strength . . . 24

1.4.4 Dispersion measure . . . 25

1.4.5 Spectral Index . . . 26

1.5 Importance of pulsars . . . 27

1.6 Motivation of the project . . . 29

2 Details about the project 31

2.1 Supernova and supernova remnants . . . 32

2.1.1 Dynamical evolution of supernova remnant . . . 33

2.1.2 Types of supernova remnants . . . 34

2.1.3 Distances to SNR . . . 35
2.2 Targeted searches of supernova remnants . . . 37
2.3 SNR G53.6-2.2 . . . 39
2.4 SNR G78.2+2.1 . . . 42
2.5 SNR G89.0+4.7 . . . 44
2.6 SNR G116.9+0.2 . . . 47
2.7 SNR G156.2+5.7 . . . 50

3 Data processing : software, hardware and parameters 53
3.1 Search hardware . . . 54
3.2 Pre-requisites . . . 55
3.2.1 Dedispersion stage . . . 55
3.2.2 Fourier transform . . . 57
3.2.3 Harmonic summing . . . 58
3.2.4 Acceleration searches . . . 59
3.2.5 Signal to noise ratio, chi square statistic and significance of a signal . 60
3.3 Search software - PRESTO . . . 62
3.4 Analysis of the output of prepfold . . . 71
3.4.1 Subintegration and pulse profile . . . 71
3.4.2 Frequency and subbands . . . 72
3.4.3 Dispersion measure . . . 73
3.4.4 Period and period derivative . . . 73
3.5 Candidate selection . . . 75
3.6 Details of the observing parameters . . . 76
3.7 Processing of the data : parameters and steps. . . . 77
3.7.1 Data preparation . . . 77
3.7.2 Candidate optimization . . . 78

4 Results 79
4.1 Examples of prepfold plots . . . 80

4.1.1 Prepfold output - noise . . . 81
4.1.2 Prepfold output - RFI . . . 82
4.1.3 Prepfold output - Pulsar . . . 83
4.2 Analysis of the pulsar candidates with the help of corner plots . . . 84
4.3 Redections of known pulsars . . . 87
4.3.1 Redetection of J2047+5029 . . . 88
4.4 Flux density upper limits of the survey . . . 90
4.4.1 Flux density upper limit estimates of the known pulsars . . . 90
4.4.2 Flux density estimate of the five supernova remnants . . . 91

5 Discussion and conclusion **100**
5.1 Comparison of flux densities of pulsars . . . 101
5.1.1 J2021+4026 . . . 101
5.1.2 J2047+5029 . . . 101
5.2 Comparison of flux densities of SNRs . . . 102
5.3 Significance of redetection of pulsar and its possible association with the remnant . . . 104
5.4 Reasons behind the undetection of pulsar in the remnant . . . 105
5.5 Conclusions and future work . . . 108

Appendices **109**

A A brief overview of the theory of supernova remnants **110**
A.1 Radio morphology of SNR . . . 111

B Some of the corner plots of the five remnants **113**
B.1 53.6-2.2 . . . 114
B.2 78.2+2.1 . . . 115
B.3 89.0+4.7 . . . 118
B.4 116.9+0.2 . . . 123
B.5 156.2+5.7 . . . 127

C Calculation of the velocity of the pulsar **132**

List of Tables

2.1 List of targeted supernova remnants studied in the survey 38

3.2 Table of the data parameters for data preparation part of the pipeline 77

3.3 Table of parameter for candidate optimization part of the pipeline 78

4.1 Number of prepfold plots for each SNR 80

4.2 Ephemeris of the three known pulsars 87

4.3 Table of the measured and derived quantities of PSR J2047+5029 89

4.4 Table of the pointings of SNR along with position, observation time and total flux density estimate 93

4.5 Average flux sensitivity threshold of SNR. 99

5.1 Velocity of the pulsar to escape the remnant 107

List of Figures

1.1 First chart recorder output of CP1919 17
1.2 The lighthouse model of a pulsar 18
1.3 The period-period derivative diagram for pulsars 20

2.1 Radio image of SNR G53.6-2.2 40
2.2 Optical image of SNR G53.6-2.2 40
2.3 ASCA and ROSAT image of SNR G78.2+2.1 42
2.4 WENSS radio image of HB 21 overlaid with contours of ROSAT survey 45
2.5 ASCA image overlaid with contours of ROSAT image 45
2.6 Optical observations overlaid with radio contours. 48
2.7 Grey scale ROSAT observations superimposed with chosen contours of radio 51

3.1 Dispersed and dedispersed pulse for a signal 57
3.2 Dependance of pulsar signal's significance on the number of harmonics summed 59
3.3 Graphical output of DDplan.py in PRESTO 63
3.4 Graphical output of rfifind routine of PRESTO 65
3.5 Graphical output of realfft routine of PRESTO 67
3.6 Graphical output of prepfold routine of PRESTO 69
3.7 Parts of prepfold plot 70

4.1 Prepfold plot of a noisy candidate 81
4.2 Prepfold plot of radio frequency intereference (RFI) 82
4.3 Prepfold plot of a test pulsar 83

4.4 An example of corner plot 85
4.5 Detected pulsar, PSR J2047+5029 88
4.6 VLA image of SNR G53.6-2.2 overlaid with pointings with its flux density limits. 94
4.7 VLA image of SNR G78.2+2.1 overlaid with pointings with its flux density limits. 95
4.8 VLA image of SNR G89.0+4.7 overlaid with pointings with its flux density limits. 96
4.9 [VLA image of SNR G116.9+0.2 overlaid with pointings with its flux density limits. 97
4.10 VLA image of SNR G156.2+5.7 overlaid with pointings with its flux density limits. 98

5.1 X-ray luminosities as a function of age for known neutron stars in SNRs . . . 106

B.4 Corner plot of G78.2+2.1, pointing 5_0003 117

Abstract

The association of pulsars and supernova remnants has been an intriguing question even after decades of research. The search for pulsars in a supernova remnant is not always successful due to the uncertainties in the position of the pulsar. However, the discovery of a pulsar in a supernova remnant opens up new avenues of research.

In this project, five supernova remnants were searched for radio pulsars with the Green Bank Telescope at 820 MHz with a bandwidth of 200 MHz. The data was processed with the help of the pulsar search software, PRESTO, developed by Ransom et al. (2002) up to a dispersion measure of 2000 pc cm^{-3} with a step size of 0.3. Due to time constraints on data processing we were able to search the remnants for isolated pulsars only. All candidates with a high sigma value were folded and analysed. Further analysis was also done with the help of plots and individual folding of candidates at respective dispersion measures and period.

No new pulsars were detected in the survey. However, we were able to redetect J2047+5029. We were unable to detect the other known pulsars in the field of view of our survey. We calculated the flux density limits for the known pulsars in our field of view and compared it with the known flux density limits. We also calculated the flux density limits and compared its sensitivity with the known sensitivities of the remnants from previous surveys. We also discuss the reasons for the non-detection of a pulsar in the studied supernova remnants. We aim to perform an acceleration search on the data in order to make the survey sensitive to binary pulsar in the future.

Declaration

No portion of the work referred to in this thesis has been submitted in support of an application for another degree or qualification of this or any other university or other institution of learning.

Copyright

i. The author of this thesis (including any appendices and/or schedules to this thesis) owns certain copyright or related rights in it (the Copyright) and s/he has given The University of Manchester certain rights to use such Copyright, including for administrative purposes.

ii. Copies of this thesis, either in full or in extracts and whether in hard or electronic copy, may be made only in accordance with the Copyright, Designs and Patents Act 1988 (as amended) and regulations issued under it or, where appropriate, in accordance with licensing agreements which the University has from time to time. This page must form part of any such copies made.

iii. The ownership of certain Copyright, patents, designs, trade marks and other intellectual property (the Intellectual Property) and any reproductions of copyright works in the thesis, for example graphs and tables (Reproductions), which may be described in this thesis, may not be owned by the author and may be owned by third parties. Such Intellectual Property and Reproductions cannot and must not be made available for use without the prior written permission of the owner(s) of the relevant Intellectual Property and/or Reproductions.

iv. Further information on the conditions under which disclosure, publication and commercialisation of this thesis, the Copyright and any Intellectual Property and/or Reproductions described in it may take place is available in the University IP Policy (see http://www.campus.manchester.ac.uk/medialibrary/policies/intellectual- property.pdf), in any relevant Thesis restriction declarations deposited in the University Library, The University Library's regulations (see http://www.manchester.ac.uk/library/ aboutus/regulations)

and in The University's policy on presentation of Theses.

Acknowledgements

I would like to thank my supervisors Dr Rene Breton and Dr. Colin Clark for the support and knowledge they have provided me over the course of my MSc. Special thanks to my fellow MSc students, Dirk, Tom, Tony, David, Tracy, Suheil, Andrea and Shankar for being there during the hard times and making every hurdle an easy one to cross. It is great having people around who always make one smile no matter what the situation is. I would also like to thank my friend, Somnath, who has helped me to become better at programming. Special mention to the Spiders team and the Pulsar group of JBCA who were always there to help me solve any problem or answer any of my questions.

Chapter 1

Introduction

In this chapter, we give a brief introduction about pulsars and pulsar properties. We also discuss the importance of pulsars and how studying pulsars provides a better understanding of the universe.

1.1 Discovery of pulsars

In 1934, only two years after the discovery of the neutron, the existence of neutron stars was proposed by astrophysicists, Baade and Zwicky (1934). They suggested that neutron stars would be about 10km in diameter and would be formed in a supernova. Then, in 1967, Pacini (1968) proposed that the Crab Nebula was powered by a star which was highly magnetized, rotating and emitting electromagnetic radiation. These theories were later confirmed by Bell, Hewish and colleagues in 1967 when they discovered the first pulsar (Hewish et al., 1968). At the time they were working on a large radio telescope observing interplanetary scintillation. They observed pulses separated by 1.33 seconds that originated from the sky and kept to sidereal time. Several possible explanations were offered, including that it was generated by another civilisation which led them to name it LGM-1, i.e. little green men. It was not until a second pulsating source was discovered in a different part of the sky that the 'LGM hypothesis' was discarded (Bell Burnell, 2004). The pulsar was dubbed as CP 1919 (Hewish et al., 1968). The first chart recorder output of the periodic signal of the pulsar is given in figure 1.1 .

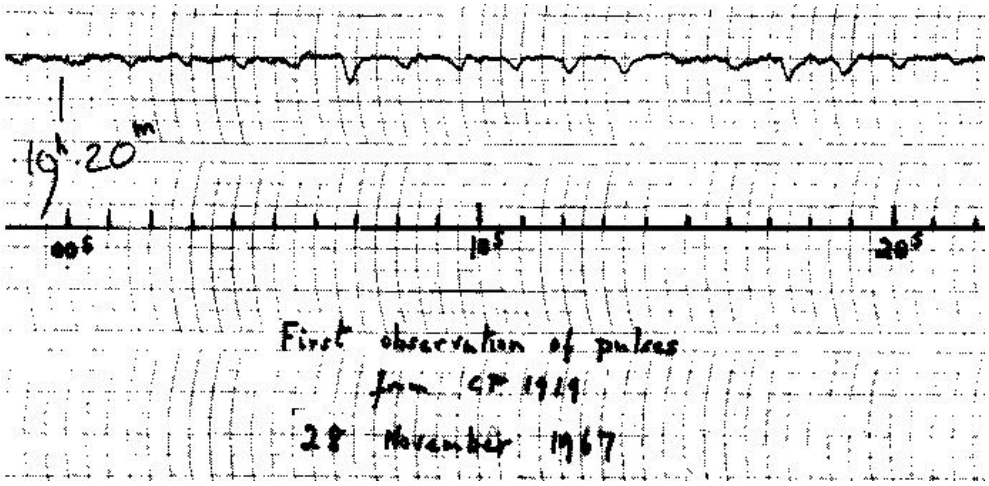

Figure 1.1: The above figure shows a copy of the chart recorder output on which are the first recorded signals from a pulsar, CP1919. This was the confirmation that the signals observed were periodic in nature and led to the discovery of pulsars (Hewish et al., 1968).

Subsequent discoveries helped astronomers understand the true nature of these strange objects which was theorized as rapidly rotating neutron stars and was supported by the discovery of Crab pulsar in the Crab Nebula (Pacini, 1968),(Backer et al., 1982).

1.2 What are pulsars?

An explosion caused due to the death of a massive star when it runs out of its fuel is called a supernova. The gravitational collapse compresses the core of the dead star past the white dwarf density to form a neutron star. Neutron stars are supported against further collapse by their neutron degeneracy pressure, similar to the electron degeneracy pressure preventing the collapse of white dwarfs. As the neutron star retains most of its angular momentum and has a very small fraction of its progenitor's radius, it is formed with a very high rotation speed. As the neutron star spins, charged particles are accelerated out along magnetic field lines in the magnetosphere. The acceleration causes particles to emit electromagnetic radiation, most readily detected at radio frequencies as a sequence of pulses. The pulses are visible as the magnetic axis crosses the observer's line of sight in each rotation. Such objects which emit electromagnetic radiation are called pulsars. The general picture of a pulsar is illustrated by the light house model as shown in figure 1.2

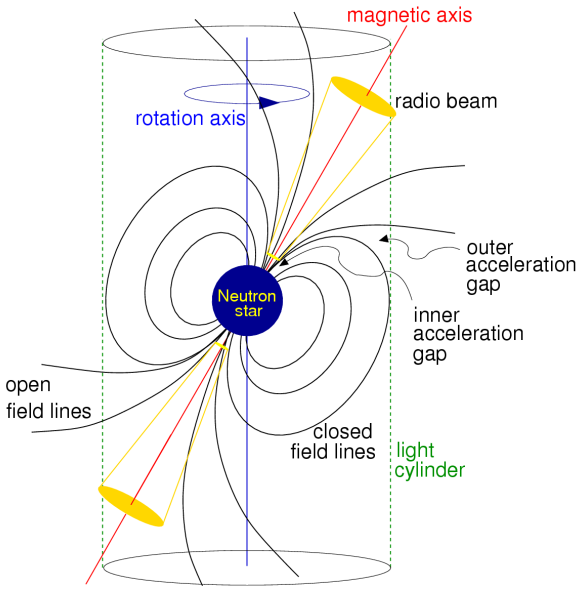

Figure 1.2: The lighthouse model shows a rapidly rotating central neutron star with a strong magnetic field, inclined to the rotation axis with radio emission emanating from the magnetic poles. The beam of radiation at the magnetic poles gives rise to pulses as the star rotates due to the misalignment of magnetic and spin axis (Lorimer and Kramer, 2004).

The spinning neutron star produces beams of radiation that sweeps across the line of sight like the light from a lighthouse beam does for a ship in the sea. In the **lighthouse model**, as shown in figure 1.2, the beam of radiation from the rapidly rotating central neutron star gives rise to pulses as it crosses the line of sight of the observer. The very precise interval between pulses that range from milliseconds to seconds makes them one of the most precise clocks of the Universe. The beam is radiated by high energy particles constrained to move along the field lines over a magnetic pole so that the beam is rigidly attached to the solid surface of the neutron star. The individual radio pulses from a particular pulsar are variable. The integrated pulse profile, the superimposition of hundreds of recorded pulses, is stable and characteristic for an individual pulsar (Liang et al., 2014).

These pulses are studied in various wavelengths, ranging from radio to X-ray. The waves propagating through interstellar medium encounter ionised gas. The interstellar medium is turbulent, with irregular structures and hence the waves do not propagate on a single ray path with a plane wavefront. This multiple propagation spreads the arrival time of an individual pulse and is referred to as *pulse smearing*. It is especially noticeable in the more distant pulsars in the galactic plane. In order to identify pulsars one has to account for smearing for proper results.

1.3 The journey of pulsars

The observed emission from a radio pulsar comes at the expense of the rotational kinetic energy of the neutron star. So, in addition to observing the pulsar spin period P , we also observe the corresponding rate of spin down, $\dot{P}$. These observations give us unique information into the spin evolution of neutron stars. The $P - \dot{P}$ diagram is given in figure 1.3 and shows the different kinds of pulsars on the $P - \dot{P}$ plane.

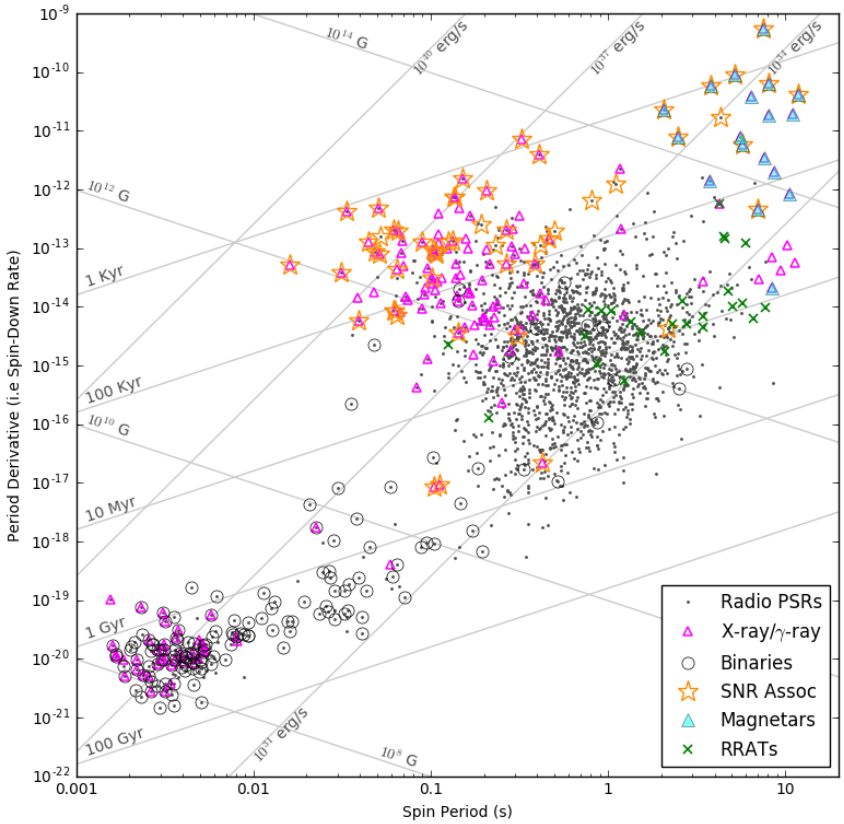

Figure 1.3: The period-period derivative diagram for pulsars is shown above and encodes a huge amount of information about the properties of pulsars. The diagram helps in distinguishing the normal and millisecond pulsars on the basis of their period and period derivative. This in turn helps in finding out the age and magnetic field strength of the two populations. The normal pulsars are shown as a cluster of points in the middle of the figure. The millisecond pulsars are located on the lower left part of the above figure. Rotating radio transients (RRATs) are represented by green cross. Magnetars lie in the top right grey region in the above figure. The figure also shows us the X-ray or gamma ray pulsars, binaries and supernova remnants associated with pulsars (Johnston and Karastergiou, 2017)

The P $-$ $\dot{\text{P}}$ diagram (figure 1.3) demonstrates clearly the distinction between the normal pulsars (P $\sim$ 0.5 s and $\dot{\text{P}} \sim 10^{-15}$ ss^{-1}) and the millisecond pulsars (P $\sim$ 3ms and $\dot{\text{P}} \sim 10^{-15}$ss^{-1}). The differences in P and $\dot{\text{P}}$ imply fundamentally different ages and magnetic field strengths for the two populations. Lines of constant magnetic field, B, and age of the pulsars, τ, helps us to infer more about the characteristic properties of pulsars. For example, from the diagram we know the typical magnetic field and age for normal pulsar is 10^{12} G and 10^7 yr and 10^8 G and 10^9 yr for a millisecond pulsar. The rate of loss of rotational kinetic energy $\dot{E}$ is also indicated. $\dot{E}$ is directly proportional to $\dot{P}$ and inversely to the cube of period, P. $\dot{E}$, as well as B and τ will be discussed in section 1.4. The rate of loss of rotational kinetic energy is the highest for the young and millisecond pulsars. The different kinds of pulsars that are shown in the figure 1.3 are discussed below.

Normal pulsars are shown as a cluster of points in the middle of figure 1.3. For majority of normal pulsars we find magnetic field of about 10^{12} G. A plausible evolutionary track for a normal pulsar would be birth at short spin periods followed by rapid spin down on a timescale of 10^{5-6} yr, eventually becoming too faint to be detectable after 10^7 yr (Wielebinski, 2002).

Millisecond pulsars are located on the lower left part of figure 1.3. They are short period pulsars and are distinguished from the normal pulsars by their period, very small spin down rates and high probability of being in binary systems. The first millisecond pulsar, PSR B1937+21, was discovered by Backer et al. (1982) in 1982, with a spin period of about 1.558 ms. The spin periods of these pulsars are extraordinarily stable and hence are very important as celestial clocks in wide variety of applications.

Rotating radio transients or RRATs are erratic pulsars discovered by McLaughlin (2006) in 2006. They are characterised by repeated bursts and are represented by green cross in figure 1.3. RRATs are easily discoverable in a search for bright single pulses rather than periodicity searches that uses Fourier transform (Keane and McLaughlin, 2011).

Magnetars are a class of young and highly magnetized neutron stars that exhibit variability ranging from few millisecond bursts to major month long outbursts. Magnetars lie in the top right grey region in figure 1.3. Its emission is powered by decay of enourmous internal magnetic fields, stressing and breaking the neutron star crust, which in turn twists the external magnetosphere and powerful magnetospheric currents (Kaspi and Beloborodov, 2017).

Gamma ray pulsars as the name suggest are pulsars that emit radiation in the gamma ray region and are shown as pink triangles in figure 1.3. Pulsars accelerate particles in their magnetosphere to high energies, which then emit gamma rays through curvature radiation (Arons, 1996).

The $P - \dot{P}$ diagram is essential in understanding the properties of pulsars on the basis of its position in the diagram. The main properties of pulsars are discussed in section 1.4.

1.4 Main properties of pulsars

The main properties of pulsars can be divided into two parts, namely, physical and observational properties. The physical properties include spin evolution, braking index, age estimate and magnetic field strength. The main observational properties are dispersion and spectral index. These physical and observational properties are discussed below.

1.4.1 Spin evolution

In reference to the $\mathrm{P} - \dot{\mathrm{P}}$ diagram shown in figure 1.3, we can clearly observe that pulse periods increase with time. The rate of increase $\dot{\mathrm{P}}$, can be related to a rate of loss of rotational kinetic energy (Lorimer and Kramer, 2004) as:

$$\dot{E} \equiv -\frac{dE_{\mathrm{rot}}}{dt} = \frac{d\left(\frac{I\Omega^2}{2}\right)}{dt} = -I\Omega\dot{\Omega} = 4\pi I\dot{P}P^{-3} \tag{1.1}$$

where $\Omega = \frac{2\pi}{\mathrm{P}}$ and is the rotational angular frequency and I is the moment of inertia. The quantity $\dot{\mathrm{E}}$ is called the *spin down luminosity* and represents the total power output by a neutron star. The bulk of the rotational energy is converted into magnetic dipole radiation, pulsar wind and high energy radiation.

1.4.2 Braking index and age estimate

According to classical electrodynamics (Jackson, 1962) a rotating magnetic dipole with moment m radiates an electromagnetic wave at its rotation frequency. The radiation power is given as :

$$\dot{E}_{\mathrm{dipole}} = \frac{2\ m^2\ \Omega^4\ \sin^2\alpha}{3\ c^3} \tag{1.2}$$

where α is the angle between the magnetic moment and the spin axis. By equating $\dot{E}_{\mathrm{dipole}}$ with the spin down luminosity in equation 1.1, we get the expected evolution of the rotation frequency as :

$$\dot{\Omega} = \left(\frac{2\ m^2\ \sin^2\alpha}{3Ic^3}\right)\Omega^3 \tag{1.3}$$

Expressing the equation with the help of a power law in terms of rotational frequency $\nu = 1/\mathrm{P}$ we get :

$$\dot{\nu} = -K\nu^n \tag{1.4}$$

where n is the braking index and K is a constant.

Expressing equation 1.4 in terms of the pulse period we get :

$$\dot{P} = K\, P^{2-n} \tag{1.5}$$

where n depends on the process braking the rotation. We obtain the age of the pulsar by integrating equation 1.5, assuming K is constant and braking index $n \neq 1$ as :

$$T = \frac{P}{(n-1)\,\dot{P}}\left[1 - \left(\frac{P_0}{P}\right)^{n-1}\right] \tag{1.6}$$

where P_0 is the spin period at birth. Assuming that the spin period at birth is much shorter than the present value and that the spin down is due to magnetic dipole radiation (n=3), equation 1.6 implies a characteristic age as follows :

$$\tau_c = \frac{P}{2\dot{P}} \simeq 15.8\ \mathrm{Myr}\left(\frac{\mathrm{P}}{\mathrm{s}}\right)\left(\frac{\mathrm{P}}{10^{-15}}\right)^{-1} \tag{1.7}$$

1.4.3 Magnetic field strength

Although no direct measurements are possible for radio pulsars, we can obtain an estimate of the magnetic field strength by assuming that the spin down process is dominated by dipole braking. The magnetic moment is related to the magnetic field strength according to $\mathrm{B} \approx |\mathrm{m}|/\mathrm{r}^3$ By rearranging equation 1.3, we obtain the field strength at the surface as :

$$B_S \equiv B(r = R) = \sqrt{\frac{3c^3 I P \dot{P}}{8\pi^2 R^6 \sin^2\alpha}} \tag{1.8}$$

For a neutron star with moment of inertia $\mathrm{I} = 10^{45}\mathrm{g\ cm}^2$ and radius R = 10 km, assuming $\alpha = 90^\circ$, we get

$$B_S = 3.2 \times 10^{19} G\sqrt{P\dot{P}} \simeq 10^{12} G\left(\frac{\dot{P}}{10^{-15}}\right)^{1/2}\left(\frac{P}{s}\right)^{1/2} \tag{1.9}$$

This is essentially an order of magnitude estimate as the value of α is usually unknown and also radius and moment of inertia are uncertain. Shapiro et al. (1983) pointed out that equation 1.9 gives the field strength at the magnetic equator and the magnetic field at the poles should be a factor of two higher.

1.4.4 Dispersion measure

Radio waves are the very low frequency form of light radiation and are oscillating electric and magnetic fields. In the presence of charged particles of the interstellar medium the electromagnetic interaction between the light and charged particles causes a delay in the propagation of light with the delay being a function of radio frequency and the masses of the charged particles. The components of each pulse emitted at higher radio frequencies arrive before those emitted at lower frequencies. This dispersion is mainly due to the free electrons which make the group velocity frequency-dependant (Lorimer and Kramer, 2004). The extra delay added at a frequency ν is given as :

$$t = k_{\mathrm{DM}} \times \frac{DM}{\nu^2} \tag{1.10}$$

where the dispersion constant k_{DM} is given as :

$$k_{\mathrm{DM}} = \frac{e^2}{2\pi m_e c} \tag{1.11}$$

and the dispersion measure, DM , is the column density of the free electrons i.e. the number density of electrons integrated over the path travelled by the photon from pulsar to the Earth and is given as :

$$DM = \int_0^{\mathrm{d}} n_{\mathrm{e}} dl \tag{1.12}$$

with units of parsec per cubic centimetre. For the delay between two frequencies ν_1 and ν_2 we use:

$$\triangle\, t = k_{\mathrm{DM}} \times DM \times (\nu_1^{-2} - \nu_2^{-2}) \tag{1.13}$$

From the measurement of the pulse arrival time at two different frequencies we can find out the DM along the line of sight to the pulsar. The DM can then be used to estimate the distance to a pulsar by numerically integrating it assuming electron density distribution of n_e. The electron density changes with distance and hence a model of n_e throughout the Galaxy is needed to estimate distances. The NE2001 Galactic electron density model (Cordes and Lazio, 2002) and the more recent YMW16 model helps in making an estimate of the pulsar distances (Yao et al., 2017).

1.4.5 Spectral Index

The spectral index of a source is the measure of the dependence of the radiative flux density on frequency. The mean flux density of pulsars have a strong inverse dependence with observing frequency (Bhat et al., 2018). For most pulsars observed above 100 MHz the power law is given as :

$$S_{\text{mean}}(f) \propto f^{\xi} \tag{1.14}$$

where f is the observing frequency and ξ is the spectral index. For pulsar spectra that fit the single power law, the range of observed spectral indices are broad with a mean value of -1.8 ± 0.2 (Maron et al., 2000).

1.5 Importance of pulsars

Pulsars which constrain physical models are unique objects that can be used to study an extremely wide range of astrophysical problems. One can study the gravitational potential and magnetic field of the Galaxy (Taylor and Weisberg, 1982), the interstellar medium (Porayko et al., 2019), binary systems and their evolution (Kramer et al., 2006) and the interior of neutron stars by studying pulsars (Demorest et al., 2010). Pulsars are considered as natural clocks emitting highly polarized coherent signals.

Pulsars are also unique objects for testing General Relativity (GR). Binary pulsar systems help to test GR in the strong gravitational field regime. By comparing the observed periastron advance to the value predicted by GR, one can test and constrain GR (Baade and Zwicky, 1934). Pulsar timing arrays help to detect the stochastic gravitational wave background predicted by various cosmological theories, from supermassive black hole mergers in the early Universe. These timing arrays compliment Earth bound gravitational wave detectors like LIGO (Jaffe and Backer, 2003b,a).

Pulsars as galactic objects and their interaction of their polarised emission with the magnetised-ionised interstellar medium (ISM) makes them excellent probes to study the properties and structure of the Milky Way. The dispersion measure of the pulsars help in mapping out the Galactic distributions of free electrons (Gupta, 2002). It is also possible to study the dynamics of the ISM on small time and length scales through regular monitoring of pulsars, for example, the 33 ms pulsar B0531+21 that powers the Crab supernovae remnant (Backer and Chandran, 2000).

The discovery of new pulsars is an important step towards knowing the rate of death and formation of stars in our Galaxy (Ghosh and White, 1999). The measurements of pulsar masses provide information about the properties of fundamental physics at extremely high densities. The motivation for probing deeper into the population of celestial objects

is to discover exotic pulsars and binary systems to better characterise the Galactic distribution and evolution of neutron stars. The understanding of these small compact objects help us to grow aware of the diverse array of objects in our Universe. However, extreme pulsars which help us constrain physical models are rare objects and therefore there is a need to find as many as possible.

1.6 Motivation of the project

In this project, we aim to study five supernova remnants to identify their neutron stars by their radio pulses alone. Our targets were selected based on the criterion that the supernova has to be near and well defined and should not be a type Ia supernova. We also have to make sure that the remnant should not already be associated with a radio bright neutron star and/or central synchrotron nebula in the frequency range that we are searching. The data obtained is then processed using pulsar searching software, PRESTO, developed by Ransom et al. (2002).

Two gamma-ray pulsars are believed to be associated with the remnants in this survey. We aim to find these gamma-ray pulsars and provide a new flux density limit for the pulsars. We also aim to provide a better survey sensitivity as compared to previous surveys of supernova remnants.

Our goal is to find new neutron stars in supernova remnants and explore its association with the remnant. These new detections will help to learn more about the pulsar emission mechanism which is still not understood very well. Our analysis will either allow an identification of a new faint source or set much stronger limits than presently possible.

Chapter 2

Details about the project

In this chapter, we provide a detailed discussion about the supernova remnants that were observed and analysed in this survey. The offline data processing is done with the pulsar searching tool, PRESTO which will be discussed in the next chapter.

2.1 Supernova and supernova remnants

A supernova is an astronomical event that occurs at the last stage of stellar evolution of a star. Supernovae can be broadly classified into two big groups depending on the explosion mechanism : the *Type Ia* and *Type Ib, Ic and II*. Type Ia are the result of a thermonuclear explosion of a degenerate carbon-oxygen stellar core. The type Ib, Ic and II are a result of gravitational core-collapse of massive stars (initial mass, $M \geq 8M_{\odot}$) that have exhausted all their nuclear fuel. If the stellar core is about 1.4 - 3 $M_{\odot}$, the compact remnant is a neutron star. If the mass of the core is greater than $\sim 3\ M_{\odot}$, then the compact is a remnant. (Dubner and Giacani, 2015).

After the explosion, about 10^{51} erg of mechanical energy are deposited in the interstellar medium and a huge amount of stellar mass is ejected. The outer layers of the star blow off in all directions and the enormous explosion imparts high velocities to the portions of the ejected envelope. Hundreds of years later, the ejected material slows down and eventually merges with the surrounding gas. However, for several thousands of years, a distinctive nebula, which we call a supernova remnant (SNR), persists and can be detected across the whole electromagnetic spectrum from radio to gamma rays. A SNR, or supernova remnant, consists of material ejected in the supernova explosion as well as interstellar material that has been swept up by the passage of the shock wave from the exploded star.

Before the development of radio astronomy, only two SNRs were known, the Crab Nebula and Kepler's SNR. Radio observations played a crucial role in the discovery and investigation of SNRs and their environments. Radio continuum surveys were the main means to identify new SNRs and study their characteristics. One of the best observed supernova remnants is SN1987A, a remnant in the Large Magellanic Cloud which was created by the explosion of a supernova in February 1987 (Benvenuto et al., 1987).

2.1.1 Dynamical evolution of supernova remnant

The evolution of SNR was first proposed by (Woltjer, 1972) and is generally defined as follows:

Free expansion phase : This stage occurs when the shock wave created because of the explosion moves outward towards the interstellar gas at high speed accumulating compressed interstellar gas behind the shock front. This material is separated from the ejected stellar material by the break of contact or contact discontinuity. Behind the contact discontinuity, a reverse shock starts to form in the ejected stellar material. After some time, the accumulated mass of the ISM compressed between the forward shock and the contact discontinuity equals the ejected mass of stellar material, and it starts affecting the expansion of the SNR, marking the beginning of the next stage.

The adiabatic expansion or Sedov Taylor phase : In this stage, after the passage of the reverse shock, the interior of the SNR is so hot that the energy losses by radiation are very small. Since all atoms are ionized, there is no recombination, and the cooling of the gas is only due to the expansion. This has an exact self similar solution given by (ref, 1950) and (SEDOV, 1959). Later, as the SNR expands and cools adiabatically, it reaches a critical temperature of about 10^6 K and the ionized atoms start capturing free electrons losing their excitation energy by radiation. The radiative losses of energy become significant, setting the end of the adiabatic expansion of the SNR. The efficient radiative cooling decreases the thermal pressure in the post-shock region and the expansion slows down. The SNR enters the next stage of evolution.

Snow plough or radiative stage : In this stage more and more interstellar gas is accumulated until the swept-up mass is much larger than the ejected stellar material. Finally, the shell breaks up into individual pieces, probably due to a Rayleigh-Taylor instability (hot thin gas pushes cool dense gas) and the SNR goes into the final phase.

Dispersion : In this last stage of the evolution of the SNR, the expansion velocity decreases to values typical of the interstellar gas and the SNR disperses into the ISM.

The stages discussed can be brief or may not occur at all. It may also happen that one or more stages occur simultaneously in different regions of the same remnant.

2.1.2 Types of supernova remnants

Supernova remnants have been classified into four categories based on their radio morphology. They are :

• **Shell type SNRs** : The appearance of this type of remnant is classified by a limb brightened shell or ring formed initially by the ejecta from the supernova and later swept up surrounding material. The diameter of the shell corresponds to the increasing shock wave produced by the explosion (Voelk, 2006).

• **Filled-center or plerions** : In these type of SNRs, the radio brightness is centrally concentrated and is often linearly polarized. Pulsar wind nebula (PWNe) is a prime example of this class of remnants. The synchotron emission from this type of remnant is associated with a pulsar that transfers the bulk of its rotational energy in a wind of relativistic particles resulting in a *Pulsar Wind Nebula*. The Crab Nebula is a prime example of this type of nebula. However, there are many plerionic remnants for which no pulsar is detected. For these cases, the detection of the nebula is a strong indication of an undetected pulsar as a powering source (Gaensler, 2001).

• **Composite SNRs** : Composite SNRs appear to have both a shell as well as an internal non-thermal pulsar driven nebula. The term *composite*, is also used in terms of defining a SNRs with radio shell as well as centrally brightened X-ray emission. Such SNRs are called mixed-morphology SNRs and will be addressed in the next morphological class (Temim et al., 2015).

• **Mixed-morphology SNR** : As mentioned in the previous class, mixed morphology or M-M SNRs have a synchroton radio shell along with a central thermal X-ray emission. In the compilation of Green (2014), 79 % of remnants are classified as shell type, 12 % as composite and 5% as plerions (Rho and Petre, 1998).

2.1.3 Distances to SNR

A precise estimate of the distance to SNRs is essential to determine the physical parameters and understand their nature. It is, unfortunately, one of the most difficult quantities to measure with accuracy. In general, for less famous sources, several methods have been used to measure distances to Galactic SNRs, including the $\sum -D$ (radio surface brightness-to-diameter) relation, kinematic distances through atomic and molecular absorption and emission, association with other objects with known distances (usually HII regions, OB associations, pulsars) assuming that they are neighbours, X-ray and optical observations, etc. In this section, we briefly describe the $\sum$ - D relation, kinematic distances and distances from X-ray observations.

$\sum$ **- D relation** - Although the application of this method is very controversial, it is described for its historical value and because in some cases it may provide a first guess when no other distance indicator is available. It is only applicable to shell-type SNRs. The basic assumption is that since at a first approximation $\sum_\nu$, the mean radio surface brightness at frequency ν, can be assumed as an intrinsic property of the SNR and a distance-independent observational parameter (Shklovskii, 1960). After reaching a maximum value shortly after the birth of the supernova, it may be expected that $\sum$ decreases monotonically with time, while the outer linear diameter, D, of the expanding SNR will increase monotonically with time. The basic idea is then to construct an empirical $\sum$ - D relation using calibrators with distances known by other methods (Clark and Caswell, 1976).

Kinematical distance - This method is based in the construction of an absorption HI spectrum by subtracting an average spectrum obtained from an area projected against a region with strong continuum emission of the target SNR, from a spectrum, or average spectrum, of an adjacent background region. Using the radial velocity of the absorption peak and by applying a Galactic circular rotation model to convert radial velocities into distances for the SNR (Tian and Leahy, 2008). Complications arise when the HI emission is patchy and cause spurious absorption features or when the continuum is faint and it is not possible to construct acceptable absorption spectra, with peaks noticeable at least at a 5-σ level. Kinematical distances can also be derived from the study of the ISM around the SNR. When there is evidence of interaction between the SNR and the surrounding atomic or molecular gas, the radial velocity at which the best signature is identified can be used to establish an approximate distance to the SNR.

Distances from X-ray observations - Dyer and Reynolds (1999) proposed a formula for shell-type SNRs to estimate distances in the cases where it can be assumed that the SNR shell is in the adiabatic expansion phase and that the measured X-ray temperature gives a reliable estimate of the SN shock velocity, and that an initial energy of the order of $E_0 = 10^{50}$ ergs is valid for all SNe. In these cases, the distance to a SNR could be derived as a function of the initial energy, the observed angular diameter of the SNR shell, the measured X-ray flux corrected for interstellar absorption, the thermal temperature of the X-ray emitting gas, plus a function that describes the power emitted by hot electrons in a low-density plasma via free-free emission.

The distances estimated for SNRs have to be considered with caution. Even in the best cases when more than one independent distance determination can be used, the derived distances are still imprecise, either because of observational inaccuracies or because of doubtful assumptions involved in the formulae used to calculate them.

2.2 Targeted searches of supernova remnants

The association of supernova remnants and radio pulsars has been an interesting topic for several years since the discovery of the Crab pulsar (Breen and McCarthy, 1995). Ever since this association, numerous deep surveys of supernova remnants for pulsations from young neutron stars have been carried out for example, the survey of SNR 1987A to search for pulsations by Zhang et al. (2018), a search for radio pulsars in southern supernova remnants by Kaspi et al. (1996). The main problems faced in surveys of similar kind has been the uncertain position of the putative pulsar, which could lie anywhere within or around the vicinity of the associated remnant. We may also notice that sometimes the characteristic age of the pulsar is much larger than the expected age of the supernova remnant. This can suggest that the pulsar may not be associated with the remnant at all. It can also be due to the initial spin period of the pulsar being similar to the spin period when its measured.

Identifying a pulsar and supernova remnant association leads to valuable conclusions about the properties of both components like distances, ages and evolution stages. Studying a composite supernova remnant which contains a pulsar wind nebulae helps us to estimate physical properties of the progenitor explosion, central neutron star and its pulsar wind that are hard to measure directly. Associations provide means of obtaining independant ages and distance estimates, which in turn can more accurately constrain the birth properties of neutron stars, namely, period, magnetic field, luminosity and velocity distributions.

The table 2.1 shows the selected supernova remnants along with details like distance, size, age and position as specified in the proposal for observation with the Green Bank Telescope. The supernova remnants studied in our survey are discussed in detail in the later sections.

SNR	Dist (kpc)	Size (')	Age (10^3 yr)	R.A. (HH : MM : SS)	Dec (+DD : MM : SS)
G53.6-2.2	2.8	33.0	7	19 : 38 : 50	17 : 14
G78.2+2.1	1.5	60.0	7	20 : 20 : 50	40 : 26
G89.0+4.7	1.7	105.0	16	20 : 45 : 00	50 : 35
G116.9+0.2	1.6	34.0	7	23 : 59 : 10	62 : 26
G156.2+5.7	1.3	110.0	15	04 : 58 : 40	51 : 50

Table 2.1: Supernova remnants without compact objects, with distances less than 3 kpc. Ages are from Sedov-phase approximation using X-ray temperatures. The RA and DEC are the coordinates for the centre of the supernova remnant where the pulsar is expected to be born.

Pulsars found in this survey are expected to be young pulsars and will be important to study and understand pulsar properties like braking. However, non-detection of a pulsar in the above remnants will lead us to investigate the reason behind the non-detection.

2.3 SNR G53.6-2.2

SNR G53.6-2.2 (also known as 3C 400.2) is a mixed-morphology SNR. It was first suggested to be an SNR by Holden and Caswell (1969).

An uncertain parameter of the remnant is its distance and consequently its size. The distance has been estimated by several authors (Milne, 1970), (Ilovaisky and Lequeux, 1972) based on their $\sum$ - D relation. The $\sum$ - D relation is the relation between the radio surface brightness and diameter of a supernova and is explained in detail in section 2.1.3. These estimates range from 4.3 kpc (Willis, 1973) to 6.3 kpc (Caswell and Lerche, 1979). The optical observations by Rosado (1983) implies a kinematical distance of 6.7 $\pm$ 0.6 kpc which is higher than the distance estimated by $\sum$ - D relation but in good agreement with the distance estimate of Caswell and Lerche (1979). The distance of the SNR is estimated as 2.8 $\pm$ 0.8 kpc according to observations of the remnant in HI region (Giacani et al., 1998). The age of the remnant is estimated to be in the range of (1.4-3.2) x 10^4 yr and is in agreement with the suggestion of Goss et al. (1975)] that 3C400.2 is an old SNR of age $\geq 10^4$.

The radio morphology of the remnant is described as the overlapping of two circular shells of diameter 14' and 22'(Dubner et al., 1994), resulting from a single supernova explosion (Saken et al., 1995),(Schneiter et al., 2006). The radio observations are consistent with the HI observations, showing a denser region in the north west (NW), where the smaller shell is located (Giacani et al., 1998). A VLA image of the remnant is given in figure 2.1.

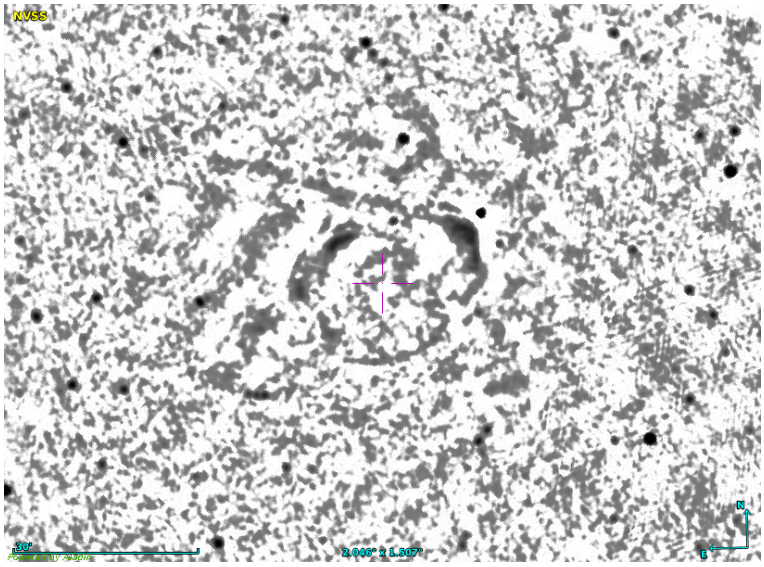

Figure 2.1: This is the radio image of SNR G53.6-2.2 by the NRAO VLA sky survey (Condon et al., 1998) overlaid with contours. We can see it has denser observations in the north west region of the SNR. The violet cross pointer shows the centre of the remnant.

The optical morphology is also characterised by a shell morphology but of a smaller radius of about 8' as shown in Fig 2.2 (Ambrocio-Cruz et al., 2006).

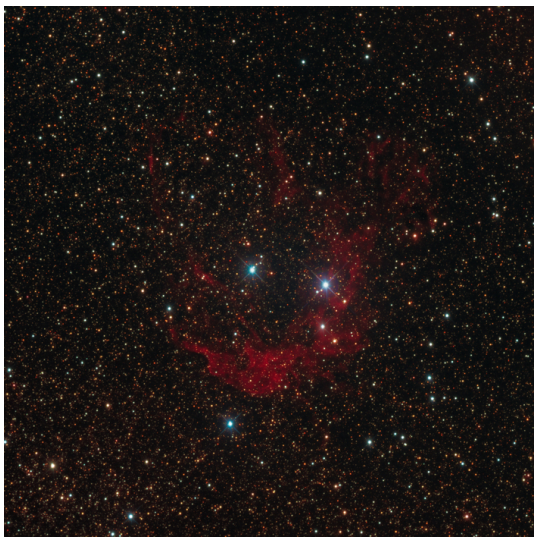

Figure 2.2: This is the optical image of SNR G53.6-2.2 (Abolfathi et al., 2018). It is a small but relatively bright region of emission and filaments. We can see a small and faint arc to the west. Two bright optical sources are also visible in the remnant.

HI void coincides with the geometrical centre of the optical shell (Giacani et al., 1998). Chandra observations of the remnant establish its class of mixed-morphology remnant (Broersen and Vink, 2015).

The remnant has been searched for pulsars using Arecibo 305 m telescope at 430 and 1420 MHz. They used long durations of observations (20 minutes to 2 hr) with rapid sampling to reach a high sensitivity of about 0.5 mJy. The duration of the observation varied per source transit and several sources were observed more than once. The pulse search used standard power spectral analysis. Dispersion measures up to 1500 pc cm^{-3} were used for 430 MHz data. However, no pulsars were detected in this survey (Gorham et al., 1996).

2.4 SNR G78.2+2.1

SNR G78.2+2.1 (also known as γ Cygni) is a shell type, degree size extended source which has been imaged in radio waves to γ-rays. The SNR is located in Cygnus X region of massive gas and dust complexes and very close to the powerful Cyg OB2 association (Leahy et al., 2013).

The radio diameter of the remnant is approximately 60 arcmin (Higgs et al., 1977). A distance of about 1.5 kpc was estimated from radio HI observations (Landecker et al., 1980). The Chandra spectra for G78.2+2.1 show that a Sedov model has an age of 6800-10000 yr (Leahy et al., 2013).

Archival ROSAT and ASCA observations showed that the remnant has a complex structure with ROSAT emission extending beyond the apparent SNR shell possibly indicating expansion into a progenitor star wind cavity (Lozinskaya et al., 2000). ASCA image of the centre of the remnant superimposed with contours constructed from the ROSAT data are given in figure 2.3.

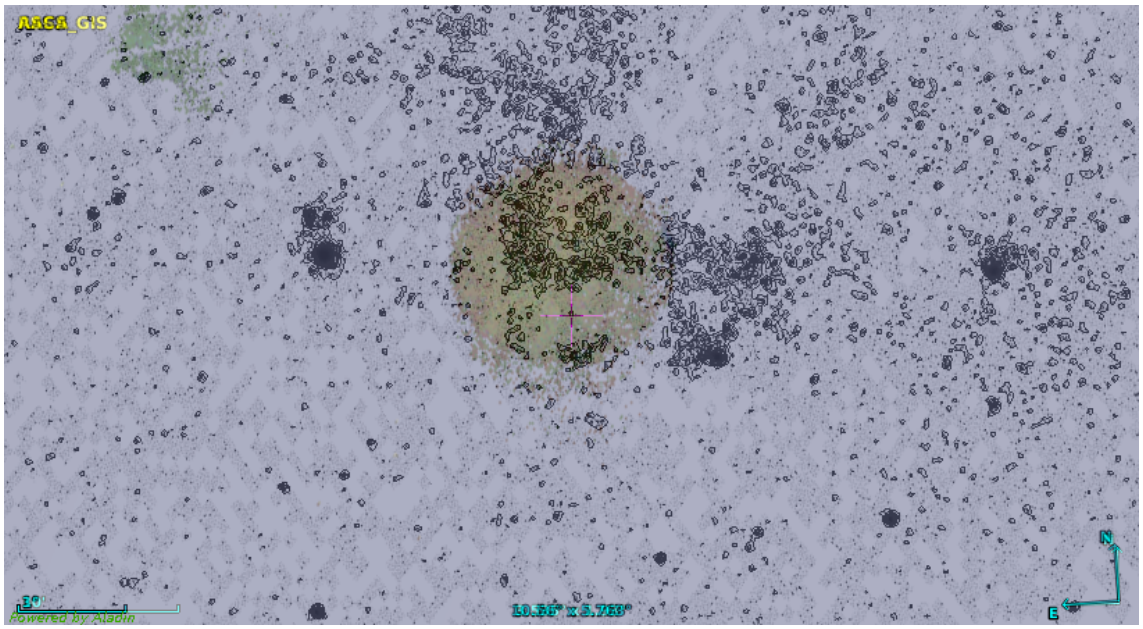

Figure 2.3: ASCA (Ueda, 1999) image of the central of the remnant formed from the sum of four pointings. It is superimposed with contours as constructed from ROSAT data (Voges et al., 1999).

Archival ASCA observations found X-ray emission above 4 keV in localized clumps in the Northern part of the remnant (Uchiyama et al., 2002).

The central north and the north west regions were studied by Chandra. Chandra observations show that most of the X-ray emission comes from a point source. The point source is thought to be a reddened main sequence star (Weisskopf et al., 2006).

A sensitive search was carried out by Lorimer et al. (1998) for young pulsar associated with the remnant. The observations were made with the 76m Lovell Telescope, at a frequency of 606 MHz with a total bandwidth of 8MHz. The survey reached a nominal sensitivity of ~ 1 mJy. 13 individual telescope pointings, each of 35 minutes were required to cover the remnants bigger than the beam of the telescope. The offline search included Fourier analysis of time sequence of dedispersed data in order to search for significant features in the power spectrum. Dispersion measure up to 995 pc cm^{-3} were searched. However, no pulsars were found to be associated with the remnant.

A high energy gamma-ray source, 2CG 078+2, was discovered in the field of the remnant with the COS B satellite (Swanenburg, 1981). This unidentified source was suspected to be a pulsar or interactions of accelerated energetic particles with matter and radiation (Sturner et al., 1997), (Gaisser et al., 1998), (Bykov et al., 2000). Using the Fermi LAT, a blind search established the unidentified source as a gamma-ray pulsar (Abdo et al., 2009). The radio quiet, X-ray pulsar, PSR J2021+4026, has a periodicity of ≈ 265.3 ms from a deep XMM-Newton observations and is located at the edge of the remnant (Lin et al., 2013). For G78.2+2.1, the XMM-Newton also studied the central and part of the south-eastern region with superior photon statistics. The column absorption deduced from the X-ray spectra of PSR J2021+4026 is consistent with the diffuse emission of the various part of the SNR. It indicates that the pulsar emission, diffuse X-ray emission and the radio shell are at the same distance. This supports the association between the pulsar and the supernova remnant (Hui et al., 2015).

2.5 SNR G89.0+4.7

SNR G89.0+4.7 (also known as HB 21) is a large, mixed-morphology SNR. It was discovered by Hanbury Brown and Hazard (1953) at 159 MHz. Strong linear polarizations in the radio band have been reported by Kundu et al. (1973). Polarizations measurements showed that the alignment of the magnetic field in the emission regions is neither radial nor tangential (Kundu et al., 1973).

G89.0+4.7 is middle aged SNR of about 5000-7000 years (Lazendic and Slane, 2006). Estimates of the distance of the SNR varies a lot. A range of 1.0 to 1.6 kpc is given by the references in Leahy (1987). All the distances are derived using the surface brightness-diameter relation for SNRs. Tatematsu et al. (1990) state that the SNR is a part of the Cyg OB7 association, which is at a known distance of 800 pc. However, the distance of HB 21 was suggested to be greater than 1.6 kpc due to the lack of direct evidence of interaction of the SNR with the OB association, combined with a low X-ray surface brightness (Byun et al., 2006). They combined all available distance estimates to arrive at a value of 1.7 kpc.

The remnant has been observed in radio and is suspected to be interacting with a molecular cloud because of its deformed shape in radio and the existence of nearby giant molecular clouds (Erkes and Dickel, 1969). The interaction was confirmed with the detection of broad CO emission lines near the edge and the center of the remnant (Koo et al., 2001). This detection also supported that the cloud evaporation might be responsible for the enhanced thermal X-rays in the central region (Leahy and Aschenbach, 1996). Radio and X-ray emission has also been compared in 2.4, which shows that there is no radio emission corresponding to the central X-ray emission. The fainter diffuse X-ray emission extend toward the radio limbs in all directions except for the east. Optical images also imply that extinction toward the eastern SNR region is higher than elsewhere.

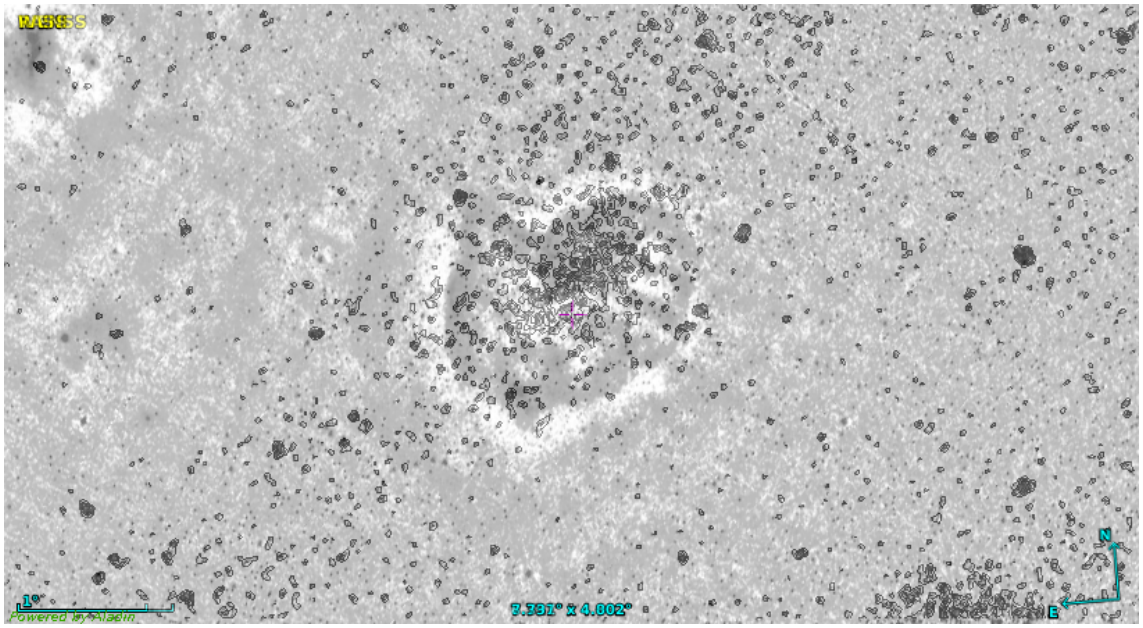

Figure 2.4: WENSS radio image (Rengelink et al., 1997) is overlaid with contours of the ROSAT image (Voges et al., 1999). There is no radio emission corresponding to the central X-ray emission. Faint emission is seen in the northern, southern and western limbs of the SNR.

HB 21 has also been studied with ASCA and ROSAT as shown in Fig 2.5. It has been observed that the X-ray emission is centrally concentrated and appears elongated in the northwest-southeast direction (Leahy and Aschenbach, 1996).

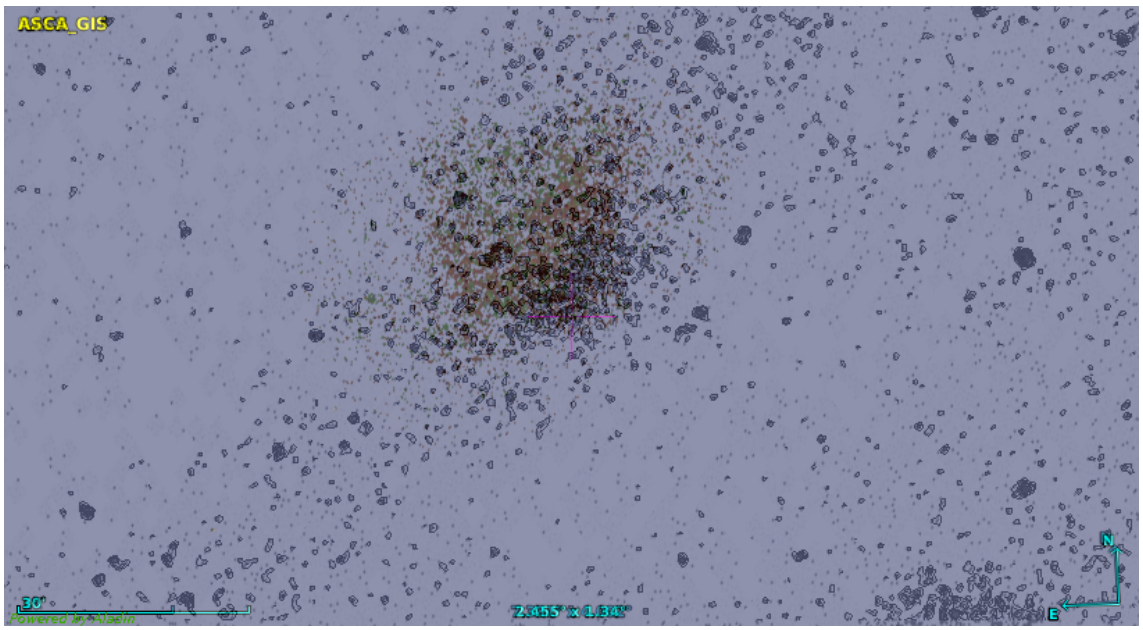

Figure 2.5: The ASCA image (Ueda, 1999) are overlaid with contours of ROSAT image (Voges et al., 1999). The faint ASCA observations are visible in the middle of the picture. The ASCA and ROSAT observations is in good agreement with each other.

The ASCA and ROSAT image are in good correlation. The X-ray emission appears clumpy in both images. The two brightened clumps of X-ray emission are located along the bright shell in the ASCA image, and then do not have corresponding bright emission in ROSAT (Lazendic and Slane, 2006).

HB 21 was searched for a radio pulsar down to a limit of 13 mJy (at 610 MHz) (Biggs and Lyne, 1996), but no pulsar was detected. The whole remnant was also searched by Lorimer et al. (1998) at 610 MHz, to a sensitivity limit of 0.66 mJy. However, they were unable to detect any pulsar. A pulsar, PSR J2047+5029, was detected by Janssen et al. (2009) with the Westerbork Synthesis Radio Telescope at a frequency of 328 MHz. The pulsar is not believed to be associated with the remnant. Detailed discussion about the discovery and its association with the remnant is done in sections 4.3.1 and 5.3.

2.6 SNR G116.9+0.2

SNR G116.9+0.2 (also known as CTB 1) (Wilson and Bolton, 1960) is a oxygen rich, mixed morphology type supernova remnant. It has an extended region of emission lying at the position of a fibrous ring-like nebula which van den Bergh (1960) suggested is a possible supernova remnant. At 750 MHz and 1400 MHz shows the remnant as a roughly circular source superimposed on an extended area of emission (Willis and Dickel, 1971). The circular source has a shell like appearance with a drop in intensity at the center and the strongest emission peak to the west at 1400 MHz (Willis and Dickel, 1971).

Wilson and Bolton (1960) observing at a frequency of 960 MHz, found that the radio source has a diameter of about 1 degree. The distance to CTB 1 as derived by bulk optical velocity and a galactic rotation curve is 3.1 kpc (Hailey and Craig, 1995).

The remnant has an almost complete shell in both optical and radio as shown in Fig. 2.6. The uniform optical and radio shells which define CTB 1 are indicative of a blast wave extending into a relatively uniform interstellar medium (Lazendic and Slane, 2006).

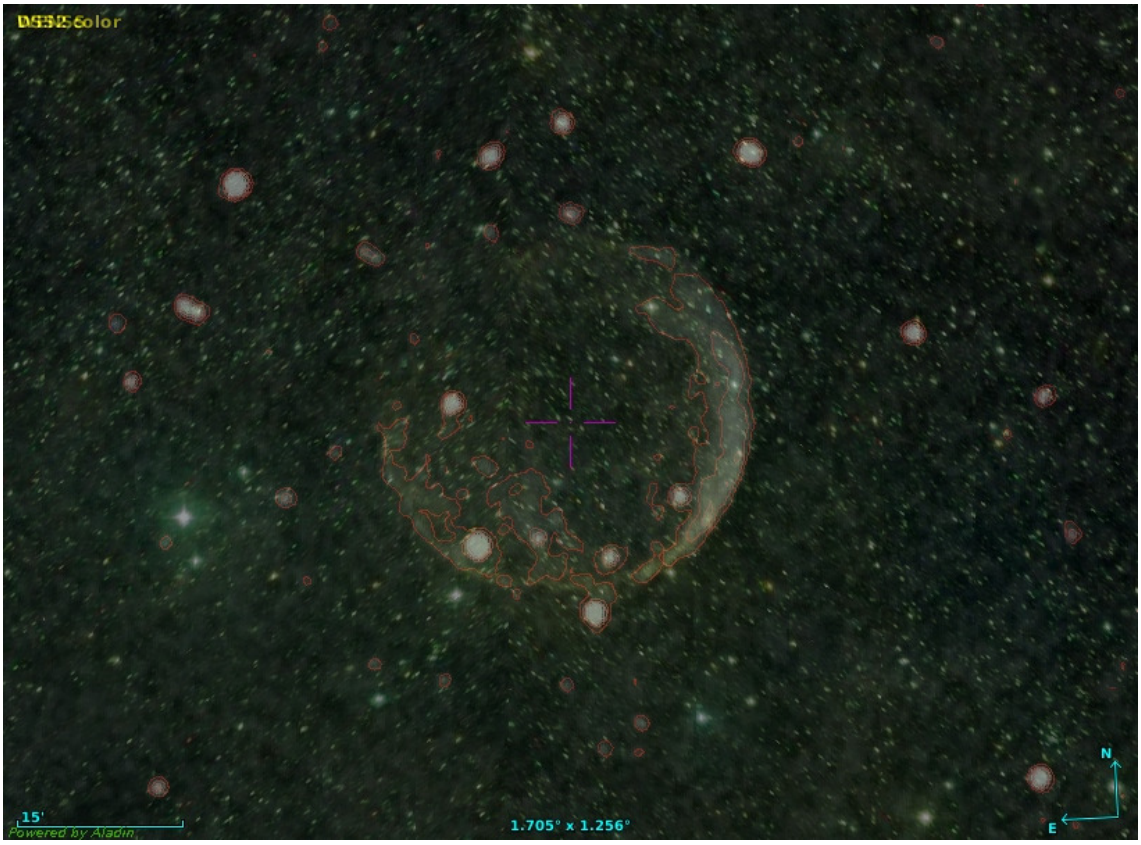

Figure 2.6: The figure shows the faint optical observations (Abolfathi et al., 2018) of CTB 1 overlaid with faint contours of radio observations (Condon et al., 1998). We can clearly see that it has complete shells in both optical and radio.

CTB 1 is observed at X-ray by ASCA. The ASCA images revealed a hard x-ray source which was speculated to be X-ray pulsar with possible association with the supernova remnant.

A radio survey of the remnant by Lorimer et al. (1998) with the 76 m Lovell telescope was carried out to detect pulsars. No pulsars were detected in the survey.

A gamma ray pulsar, J0002+6216 (Clark et al., 2017), was detected by the Einstein@Home survey of unidentified Fermi-LAT sources. It is believed to be associated with the remnant (Zyuzin et al., 2018). It is located near the edge of the remnant at an angular distance of only about 17 arcmin from the centre. The pseudo distance of 2.3 kpc is consistent with the SNR distance range of 1.5-4 kpc, favouring the association (Zyuzin et al., 2018). The pulsar is radio loud and has been observed in S and L band. It was detected in a two hour observation conducted at 1.4 GHz with the Efflesberg Telescope at a DM of 218.6 pc cm^{-3}

(Wu et al., 2018).

2.7 SNR G156.2+5.7

G156.2+5.7 (also known as RX04591+5147) was initially discovered in X-ray with ROSAT (Pfeffermann et al., 1991). G156.2+5.7 has a perfectly spherical shell and is one of the brightest SNRs in X-rays (Pfeffermann et al., 1991).

While Lazendic and Slane (2006) list the remnant as a mixed-morphology remnant, it does not fit the definition of the mixed-morphology SNRs in many ways: the X-ray shell is well formed and there are no CO clouds or OH masers in the vicinity. Prominent central concentrations of SI, S and Fe were detected from the ejecta component. Lighter elements of O, Ne and Mg were distributed more uniformly (Uchida et al., 2012).

The age of the remnant was estimated to be 26000 years, based on the Sedov model and is thought to be an evolved supernova remnant. The distance of the remnant is about 1.1 kpc and is large in size (100' in diameter) (Pfeffermann et al., 1991). Because of its near distance and large size it is easy to observe and study detailed plasma structure.

Radio continuum observations with the Effelsberg telescope of the X-ray detected SNR G156.2+5.7 found a weak highly polarized radio shell. The diameter of the remnant obtained in radio is larger than that obtained in the X-ray observations.

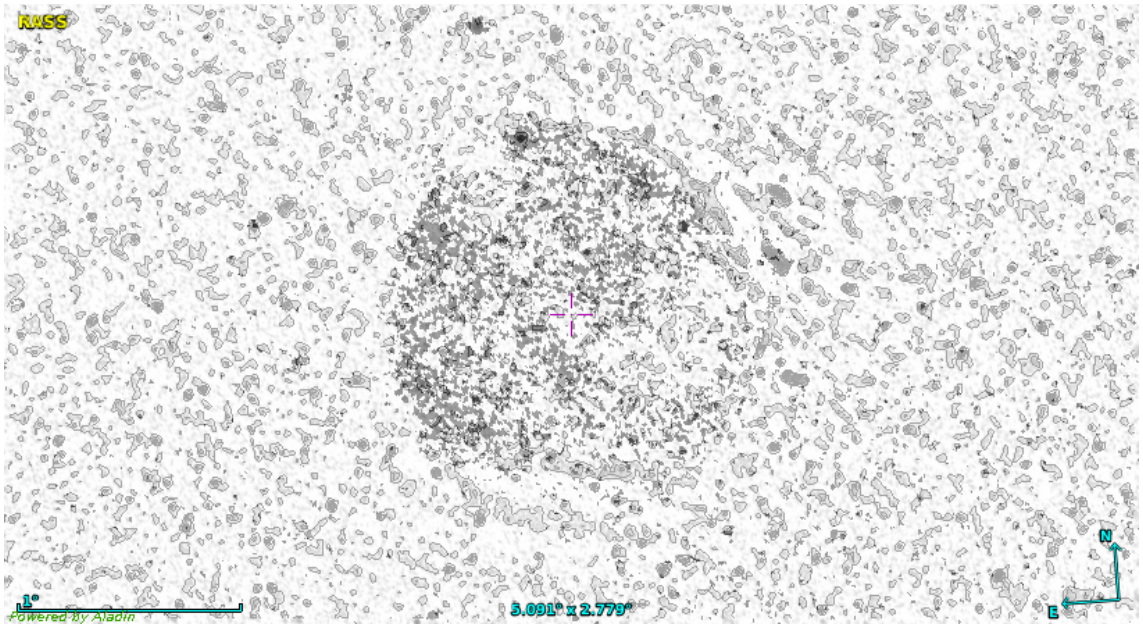

Figure 2.7: Grey scale ROSAT observations (Voges et al., 1999) superimposed with chosen contours of radio (Condon et al., 1998).

The polarization of the radio shell is rather high with typical values of 50% at 2695 MHz. We note from Fig 2.7 that the radio shell is slightly shifted towards the high galactic latitudes, which indicates a weak gradient either in the magnetic field or ambient density (Reich et al., 1992). The radio morphology show limb brightening in the northwest and southeast rim (Reich et al., 1992).

Lorimer et al. (1998) searched the remnant with 76 m Lovell telescope for pulsars. No pulsars were detected in this survey. There are no compact objects associated with the remnant to date.

Chapter 3

Data processing : software, hardware and parameters

In this chapter we discuss the hardware and software that was used to observe the remnants and analyse the data obtained. We also provide essential information about the data and the parameters and steps involved in the analysis of the data obtained.

3.1 Search hardware

The five remnants discussed in chapter 2 were observed with the Green Bank Telescope in Green Bank, West Virginia, US. The survey was conducted with the Prime Focus (PF1) receiver set to the 680-920 MHz frequency band with the 200 MHz bandwidth IF filter mode, feeding the GUPPI backend. GUPPI is the Green Bank Ultimate Pulsar Processing Instrument. It is a backend system used for nearly all pulsar observations at the GBT. The chosen configuration has a large beam size and hence minimize the pointings required for the complete survey. It also arguably provides a balance between background sky temperature and signal, given that pulsars are known to have fairly steep spectral indices (e.g. n = -1.4) (Bates et al., 2013).

The survey is capable of detecting pulsars with flux density ~ 0.2 mJy and luminosities comparable or lower to that of the faintest radio pulsars. The sensitivity achieved in the survey is of an order of magnitude better than previous targeted SNR surveys and is discussed in detail in section 5.2. It also provides an increased completeness over previous SNR surveys as it covers the spatial extent of the SNR rather than concentrating only on the remnant centres (Biggs and Lyne, 1996) (Gorham et al., 1996) (Lorimer et al., 1998) (Kaspi et al., 1996). The search software involved in data processing is discussed in section 3.2.

3.2 Pre-requisites

The first pulsar was discovered in 1967 by visual inspection of the total power output from a radio telescope (Hewish et al., 1968). However, only a small fraction of the currently known pulsars are strong enough to be detected by their individual pulses. In order to reveal the periodic nature of the pulses, we need to use sensitive telescopes and efficient techniques.

The telescope backend processes the raw baseband data and generates filterbank or fits files consisting of time series for a number of frequency channels. Pulsar searching is generally performed on total intensities only, although polarisation information can also be recorded. The time series is dedispersed and summed over frequencies.

Before we discuss how the software performs its various routines to analyse the data, it is important for us to understand the significance of some very important concepts: the dedispersion stage, Fourier transform, acceleration searches and profile significance tests like signal to noise ratio, chi-squared distribution and significance of a signal.

3.2.1 Dedispersion stage

Considering the raw data as a two-dimensional array of time samples and frequency channels, we write the j^{th} sample of the l^{th} frequency channel as R_{jl}. For n_{chans} frequency channels, the j^{th} sample of the dedispersed time series T_j is then

$$T_j = \sum_{l=1}^{n_{chans}} R_{j+k(l),l} \tag{3.1}$$

where k(l) is the nearest integer number of time samples corresponding to the dispersion delay of the l^{th} frequency channel relative to some reference frequency. Labelling the l^{th} frequency channel of the data by f_l, we can write k(l) as (Lorimer and Kramer, 2004) :

$$k(l) = \left(\frac{t_{samp}}{4.15 \times 10^6 \text{ ms}}\right)^{-1} \left(\frac{DM}{\text{cm}^{-3} \text{ pc}}\right) \left[\left(\frac{f_l}{\text{MHz}}\right)^{-2} - \left(\frac{f_1}{\text{MHz}}\right)^{-2}\right] \tag{3.2}$$

Here we have assumed that the channel ordering in R starts at the highest frequency and proceeds in decreasing frequency order. The channel frequencies are then given as :

$$f_l = f_1 - (l-1)\Delta f_{chans} \tag{3.3}$$

where f_{chans} is the channel bandwidth.

However considerations have to be made while choosing the appropriate interval between trial DM values. The DM value should not be so large that a real pulsar with true DM lying between two trial values is significantly broadened and sensitivity is lost. Conversely, the interval should not be so small that computing power is wasted on producing and searching dedispersed time series that are virtually identical for neighbouring time series. A sensible choice of DM step is to set the delay between the highest and lowest frequency channels equal to the data sampling interval. Apart from the sampling interval the DM steps also depend on center frequency, bandwidth and number of channels and subbands. A dispersed and a dedispersed pulse is shown in figure 3.1. The dispersed pulse was generated using mock data and was dedispersed using a dispersion measure of 150 pc cm^3.

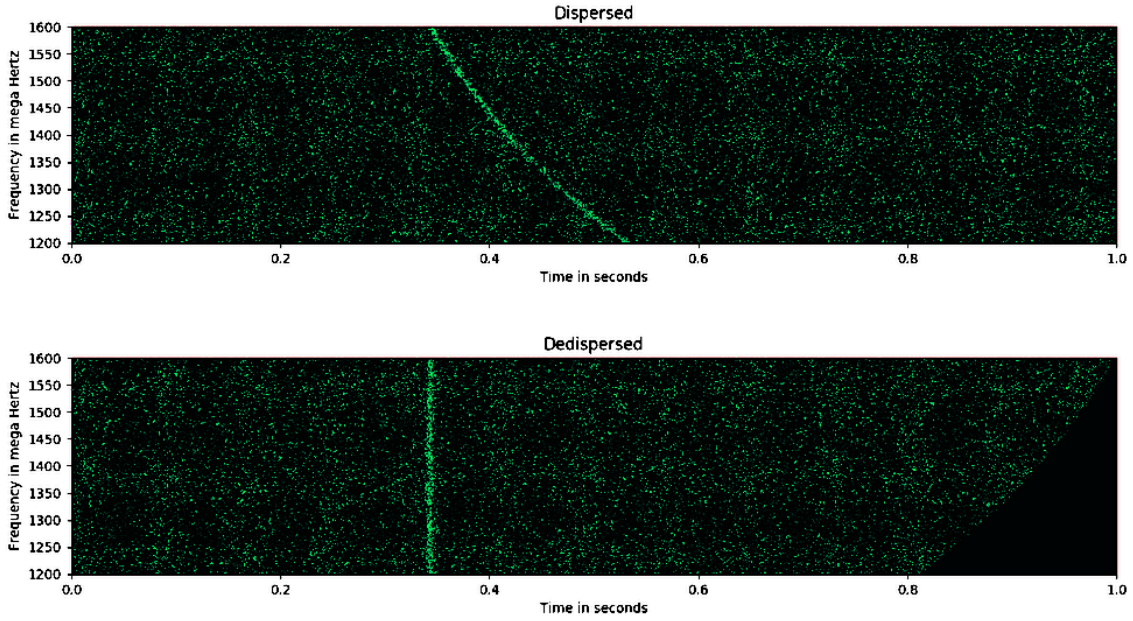

Figure 3.1: In this figure the first part shows a dispersed pulse generated from mock data. We see that the component of pulse in the higher radio frequencies arrives before those emitted at lower frequencies. This dispersion is mainly due to the free electrons in the interstellar medium which make the group velocity frequency dependant. The second part shows the dedispersed pulses with a value of DM (in this case 150) which corrects for the delay in the arrival of pulse.

3.2.2 Fourier transform

Given a dedispersed time series T_j, we need an algorithm to search it for the presence of periodic signals. One of the most efficient way to do so is by taking the Fourier transform of the time series and examine the Fourier domain. Since the dedispersed time series is a set of N independently sampled data points, we compute the Discrete Fourier transform (DFT) (Ransom et al., 2002). By definition, the k^{th} Fourier component of the DFT is given as :

$$F_k = \sum_{j=0}^{N-1} T_j \exp(-2\pi ijk/N) \tag{3.4}$$

where $i = \sqrt{-1}$ and N is the number of elements in the time series. It is apparent from the above equation that the computation of an N-point DFT requires N^2 floating-point operations. However as the value of N is very large in our computations it takes a lot of time. One of the ways to reduce the computation time is the Fast Fourier transform (FFT),

which requires only N $\log_2$ N operations to transform an N-sample time series. The highest frequency in the Fourier domain is nominally $\frac{1}{t_{samp}}$, the DFT is symmetric about the Nyquist frequency ν_{Nyq} for real-valued inputs. Nyquist frequency is the bandwidth of the sampled signal and is equal to half of the sampling frequency of the signal. It is the highest frequency that the sampled signal can unambiguously present. Fourier components above ν_{Nyq} are just the conjugates of their lower frequency counterparts. This can be exploited to calculate the FFT of two N-point real data sets simultaneously or a single data set of length N/2 (Press, 1998).

Before attempting to estimate the level of signal present in the data, it is standard practice to whiten the spectrum so that the response to noise is as uniform as possible. The most common practice is to break the spectrum into a number of pieces, calculating the mean and root mean square value for each one. Care should be taken that the outlying points do not bias the mean and root mean square values. Subtracting a running median and normalizing the local root mean square will result in the whitened spectrum having a zero mean and unit root mean square.

3.2.3 Harmonic summing

The power of most pulsars is spread over multiple harmonically related peaks in the Fourier spectrum. To maximize sensitivity to a pulsar, the power from all significant harmonics should be summed. The number of significant harmonics depend on the shape of the pulse profile, scaling roughly as $N_{harm} \approx \frac{P}{W}$, where P is the pulsar's period and W is the width of the profile. Pulsars with wider profile have their Fourier power concentrated in a small number of harmonics, whereas pulsars with narrower profiles have more significant harmonics and a flatter distribution of powers.

Fig 3.2 shows an example of how the significance of a pulsar signal grows as more harmonics are summed.

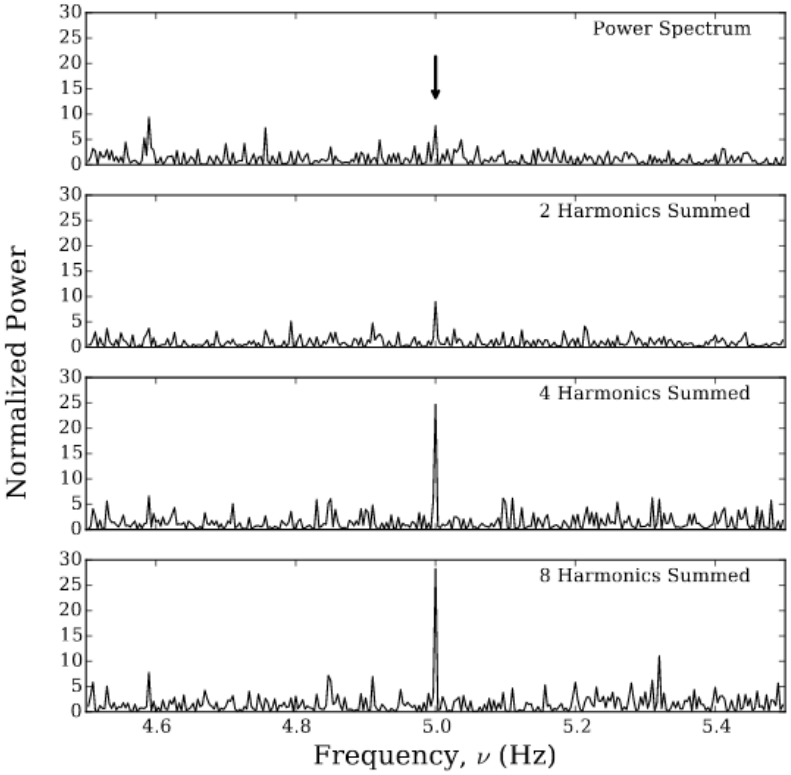

Figure 3.2: The dependance of a pulsar signal's significance on the number of harmonics summed is shown in this figure. Harmonic summing is necessary to collect the signal power of these harmonics and increase the detection significance of the pulsar signal (Lazarus, 2015)

When searcing for pulsar signals, both fundamental frequency and number of significant harmonics are unknown. Therefore, harmonically summed spectra are computed for all frequency bins. Bins is a cluster of similar valued points. It helps in reducing the data to be processed. Periodic signals in the observation are found by searching these harmonically summed spectra for peaks. In practice, it is common to search summed spectra consisting of 1, 2, 4, 8 and 16 harmonics.

3.2.4 Acceleration searches

The periodicity searches described in 3.2.2 using the Fourier transform fails in the case of binary pulsars as the high orbital acceleration attained by fast relativistic binaries result in a Doppler shift in the spin frequency of the pulsar as a function of the orbital phase (Ng et al., 2015). Hence the recovered power spreads over neighbouring frequencies and

has a significant effect on the amount of power recovered and can prevent detection. In order to prevent this the method called acceleration search is introduced. An acceleration search assumes constant acceleration for a small fraction of the orbital period. Due to acceleration, the amplitude of the signal in the computed spectrum will be spread out and it will be difficult to detect the pulsar. A search over a number of trials for different constant acceleration values can then show increased detection at trials corresponding to an accelerated pulsar (Dimoudi and Armour, 2015).

There are two main acceleration search techniques in practice. One of them works in the time domain by re-sampling the time series according to a time offset caused by the constant acceleration, followed by a standard periodicity search for each acceleration value. However, this is computationally demanding as it requires the calculation of many long FFTs. A different approach is to create a set of Finite Impulse Response (FIR) filters in the Fourier domain that describe the effect of constant frequency drift and then correlate each one with the signal. This technique is called correlation technique and is more efficient due to small filter size and is computationally easier as many computations can be performed in parallel as short independent Fourier transforms and convolutions (Dimoudi and Armour, 2015). The acceleration search technique for instance has been of use in the High Time Resolution Universe Pulsar Survey (HTRU) leading to the discovery of 60 binary pulsars (Ng et al., 2015) and also in the Parkes multi-beam survey which led to the discovery and timing of 16 binary pulsars (Eatough et al., 2013).

3.2.5 Signal to noise ratio, chi square statistic and significance of a signal

The most commonly used measure of pulse profile significance is the signal to noise ratio, S/N. For a pulsar to be detectable, its signal must exceed significantly the noise fluctuations in the receiver system. The S/N ratio in this survey, is calculated from the FFT. Signal to noise ratio is given as :

$$\frac{S}{N_k} = \sqrt{|F_k^2|} \tag{3.5}$$

where F_k is the Fourier transform after normalisation. Normalisation refers to the flattening of the spectrum in order to remove noise. It generally involves dividing short portions of the power spectrum by locally determined average power level. Proper normalization of powers is important for an accurate estimate of a signal's statistical signal or the lack of it Ransom et al. (2002).

Significance of a signal is denoted by σ and is the confidence level of our detection. It is a measure of how far the signal fluctuates from the mean. Sigma is given as (Zhu, 2008):

$$\sigma^2 = \frac{1}{n_{bins}-1} \sum_{i=0}^{n_{bins}-1} \left(p_i - p\right)^2 \tag{3.6}$$

For example, a 68 % confidence level refers to a 1 σ detection. This can be extended to a large number of free parameters and degrees of confidence. Harmonically summing of the signal in order to obtain a strong pulse increases the significance of the signal.

An alternative measure of the pulse profile's significance is to consider the deviation from the pure Gaussian noise with mean $\bar{p}$ and variance σ_p^2. It is useful for searches of narrow pulse characteristic. The chi-squared test was popularised by Leahy (1987) for folding data analyses of pulsed emission from globular clusters. χ^2 is given as :

$$\chi^2 = \frac{1}{{\sigma_p}^2} \sum_{i=1}^{n_{bins}} \left(p_i - \bar{p}\right)^2 \tag{3.7}$$

having n_{bins} - 1 degrees of freedom.

3.3 Search software - PRESTO

The data obtained has to be analysed in order to produce a result. The analysis of such data is computationally intensive and hence is done with the help of softwares and programs. The software used for searching for new pulsars in this project is PRESTO (Ransom, 2001). It is a large suite of pulsar search software and can handle data from any individual time series composed of single precision single point data. PRESTO modules are compatible with Python and lead to easy processing of data.

Before we start analysing our data for pulsars, we need to prepare the data. The preparation of the data comprises of getting an appropriate dedispersion plan and removing radio frequency interference. The data is then dedispersed to form a number of time series spanning a wide range of trial DM values. Each time series then can be independently searched for the presence of periodic signals. The best candidates from the analysis are then saved and the whole process is repeated for another trial DM. After processing all the time series this way, a list of pulsar candidates is compiled and the dedispersed data is folded modulo each candidate period for further inspection. The aforementioned processes performed by the software, PRESTO, are described in this section.

Dedispersion plan

In order to maintain sensitivity to the undiscovered pulsars a wide range of trial DMs are used. In order to dedisperse the data without any significant loss of sensitivity, a dedispersion plan is generated according to which the whole data is dedispersed into subbands. The dedispersion plan gives a document which tells us what DM values and what DM steps are to be taken when dedispersing the data into subbands. It also produces a graph, shown in figure 3.3. It shows the contribution of various smearing as a function of dispersion measures.

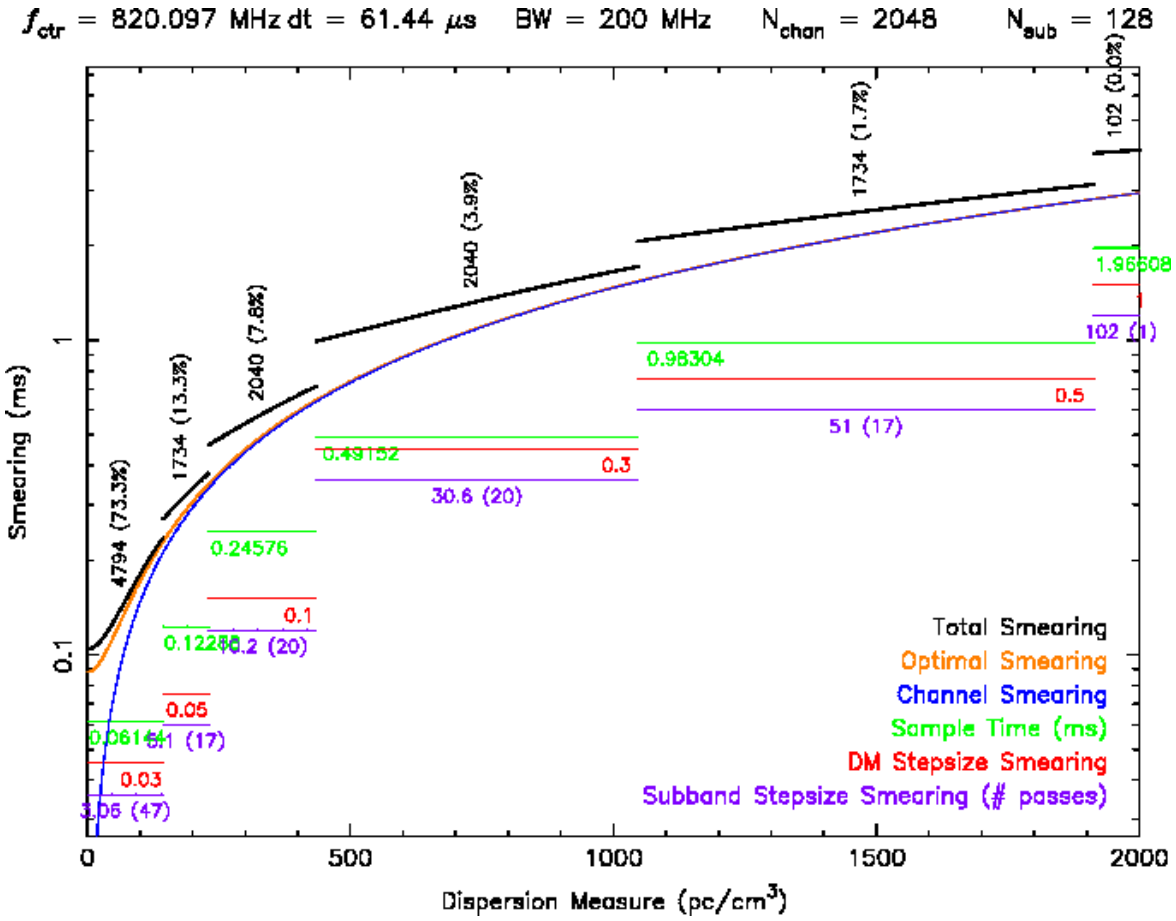

Figure 3.3: The above figure shows the smearing of the pulses in the y axis and dispersion measure in the x axis. It shows optimal step-size, channel, DM step-size, subband and total smearing. It also shows the sample time in ms. The parameters used to generate this graph are given at the top of the graph. The parameters are : f_{ctr} stands for central frequency, dt is sample time, BW is bandwidth, N_{chan} is number of channels and N_{sub} is number of subbands. Corresponding to the graph the program also creates a text file. The dedispersion stage takes the parameters from the text file as an input to perform dedispersion.

The dedispersion plan is generated by running a pre-programmed script called *ddplan.py*. It is determined by balancing the various contributions to pulse broadening that can be controlled, namely, the duration of each sample, sample time; the dispersive smearing within a single channel, channel smearing; the dispersive smearing within a single subband due to approximating the DM, subband stepsize smearing and the dispersive smearing across the entire observing band due to the finite DM step-size, DM step-size smearing. The amount of scatter broadening depends on the DM, observing frequency and line-of-sight. The total residual pulse broadening, total smearing, is estimated by summing the above smearings. Above a DM of 500 pc cm^{-3} scattering

begins to dominate. At higher DM, the step-size between successive DM trials is increased. Therefore, the extra computing required to go to high DMs is relatively small compared to what is required to search for pulsars at low DMs. Searching the data up to a high DM value ensured that we do not miss any significant signal and provides completeness to the survey.

Removal of radio frequency interference

Before we use the dedispersion plan and dedisperse the data into subbands, we need to make sure that the data is free of radio frequency interference (RFI). RFI is a source of transmission within the observed frequency band which is of terrestial origin. As a consequence of high sensitivity of radio telescopes, they are also susceptible to interfering signals from transmitters in adjacent and nearby bands. The influence of RFI can range from total disruption from saturating the receiver to very subtle distortions of the data. In our case, RFI may mimic the pulsation of the pulsar and lead to false detections. Hence, it is very useful to get rid of as much RFI as possible before we process the data further.

Removal of RFI is done with the help of a routine called *rfifind* in PRESTO. The routine rfifind searches the raw data in both frequency and time domain for interference. Each channel is analysed for short time intervals throughout the observation. PRESTO's rfifind by default considers 1s long blocks of data in each frequency channel separately. For each block of data time-domain statistics are computed: the mean of the block data value and the standard deviation of the block data values. Blocks where the value of one or more of the two statistic is sufficiently far from the mean are flagged as containing RFI. The output of figure is the resulting graph of flagged blocks used to mask out RFI as shown in figure 3.4 .

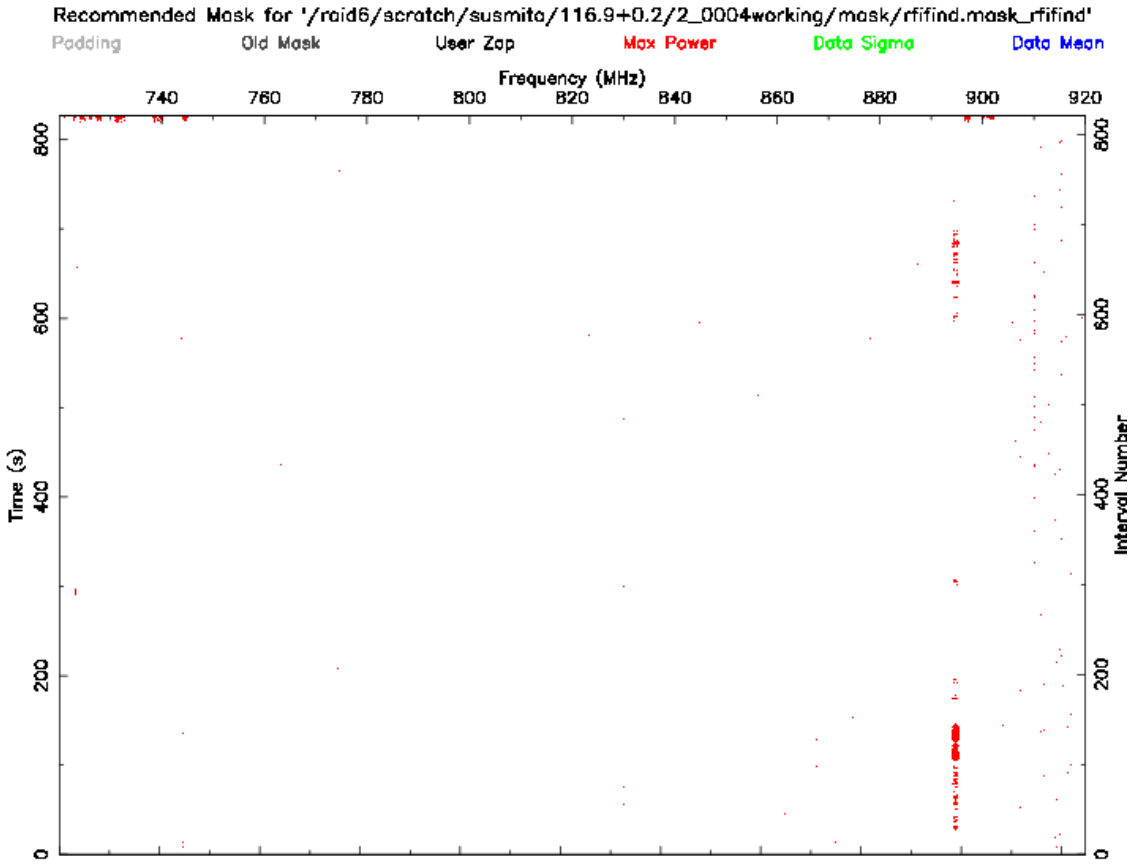

Figure 3.4: The above graph shows the channels to be masked (in red) because of possible radio frequency interference. Once the mask is obtained it can be implemented such that all further processes take into account the channels that have high interference. It helps in removing the noise as much as possible before actually processing the data and is useful for increasing efficiency of the results obtained.

The data are then masked based on the output of rfifind. Masked blocks are filled with constant data values chosen to match the median bandpass. Channels that are more than 30% corrupted with RFI are completely masked. The masked data are now used for further processing and analysing.

Dedispersing into subbands

After the removal of radio frequency interference and producing a dedispersion plan, the next step is to dedisperse the data into various time series called subbands. Dedispersing into subbands increases the computational efficiency. This is a part of incoherent dedispersion. This method requires splitting the full bandwidth of the signal into larger chunks and shifting each of these subbands by an appropriate amount of time delay to allow the

subbands to align properly. However, it does not correct for the dispersion delay inherent inside each of these subbands.

Using the existing routine called *prepsubband* we dedisperse the data into subbands. It takes the parameters from the dedisperion plan and dedisperses, barycenters and pads raw data into numerous time series over a range of trial DMs.

Periodicity searches using Fast Fourier transform

After the removal of radio frequency interference and dedispersing the data into subbands, we use FFT to produce a timeseries of the summed dedispersed subbands in order to search for periodicity. Prior to searching for peaks, it is normalised to have zero mean and unit variance. In PRESTO, we use *realfft* to perform a single precision FFT depending on the length of time series to be transformed and the output of the process is given in Fig. 3.5.

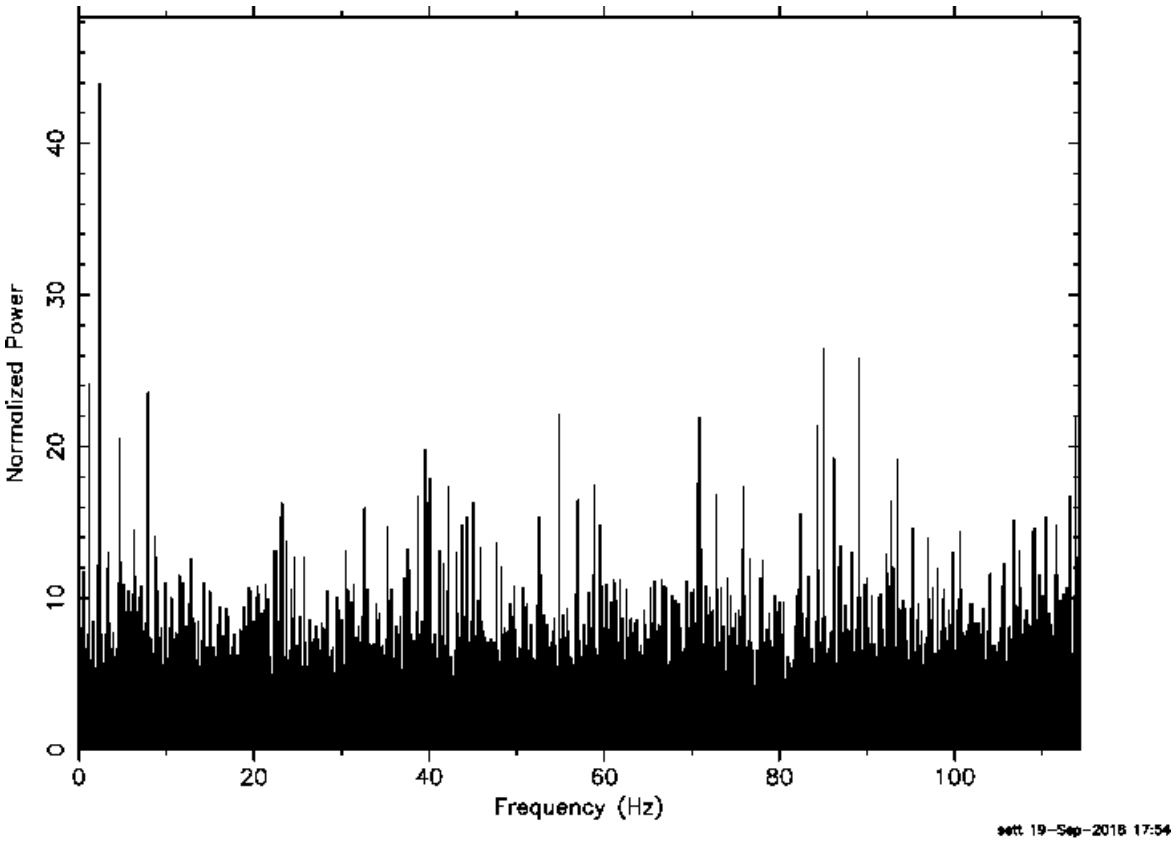

Figure 3.5: The above figure shows the result of performing realfft on the data. It performs a single precision fast fourier transform and takes the square modulus of the output giving a power spectrum as above as a result of the FFT performed.

After the data is prepared, we search the data for periodic signals using acceleration search.

Acceleration search

Acceleration search or periodicity search in PRESTO is done with the use of routine *accelsearch* which makes use of a pre-programmed script. It searches the FFT or short series for pulsars using Fourier domain acceleration search. It takes the number of harmonics to sum and the maximum Fourier frequency derivative to search and find periodic signals. The results produced by acceleration searches is used for candidate optimization. It is done for all periodicity searches irrespective of the acceleration value of the search.

Acceleration search with a non zero value of acceleration is mainly used to find binary pulsars. To improve the significance of the narrow signals, power from harmonics is

summed with that of the fundamental frequency. The harmonic summing procedure also improves the precision of the detected frequency.

However, due to time constraints on our project, we search the data using zero accleration, making the survey sensitive to isolated pulsars only. After all the processing of the data is completed, the last step is selection of the most suitable candidates.

Candidate optimization

The output of periodicity searching is a set of files, the zero-acceleration candidates lists for each DM trial, containing the frequency of significant peaks found in the Fourier transformed time series, along with other information about the candidate. These signal candidates are sifted in PRESTO with the help of pre programmed script *sifting.py* to identify the most promising pulsar candidates, match harmonically related signals and reject RFI-like signals.

The first stage of the sifting process is to remove short-period candidate signals (P < 0.5 ms), which contribute a large number of false positives as well as to ensure no candidate signals with periods longer than 15 seconds are present. Weak candidates with Fourier-domain significance or sigma less than 6 are also removed.

The next stage of sifting is to group together candidates with a similar periods (less than 1.1 Fourier bins apart) found in different DM trials. When a duplicate period is found, the candidate with less significance is removed from the main list and its DM is appended to a list of DMs where the stronger candidate was detected. At this stage, for each periodic signal, there is a list of DMs at which it was detected.

The next step is to remove candidate with suspect DM detections. Specifically, candidates not detected at multiple DMs, candidates that were most strongly detected at DM ≤ 2 pc cm^{-3} and candidates that were not detected at consecutive DM trials are all removed

from subsequent consideration. The sifiting process results in ≈ 200 good candidates per beam, which can be folded for further analysis.

Folding of the candidates

Once the master file with the possible pulsar candidates are produced, we fold the selected candidates. As pulsars are generally very weak radio sources, the addition or folding of many pulses so that the signal is visible above the background noise is vital for studying them in detail. Folding in PRESTO is done by using the routine *prepfold*. PRESTO's prepfold performs a limited search over period, period-derivative and DM to maximize the significance of the candidate. For each folded candidate, a prepfold plot as given in Fig. 3.6, is generated.

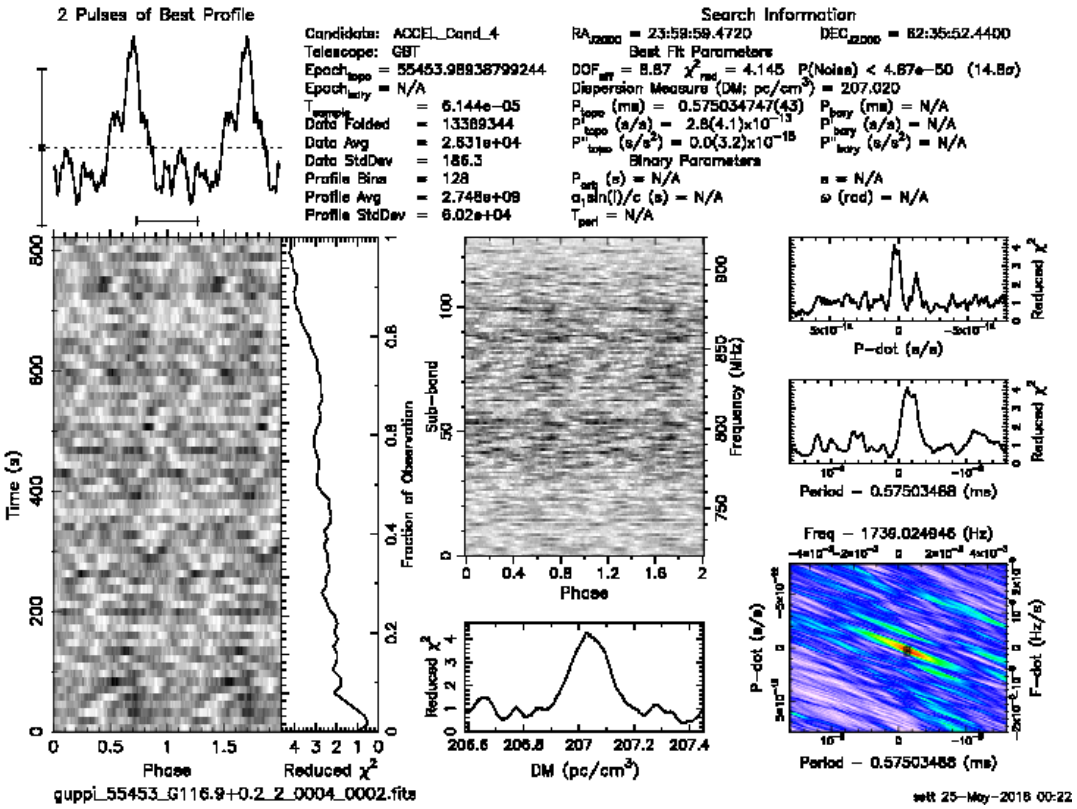

Figure 3.6: The above figure shows the output of the prepfold routine of PRESTO. It is a combination of various diagnostic graphs as described in the following figures.

As shown in 3.6, the prepfold graph is a combination of various graphs, which are shown 3.7, each of which contributes to the analysis of the candidate as a probable pulsar or RFI and noise.

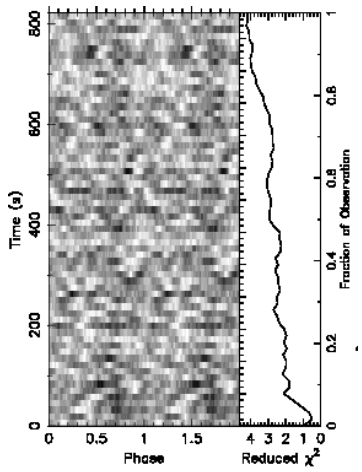

(a) Subintegration graph of prepfold routine.

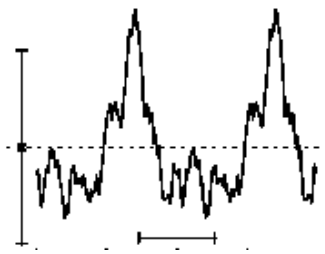

(b) Pulse profile graph of prepfold routine.

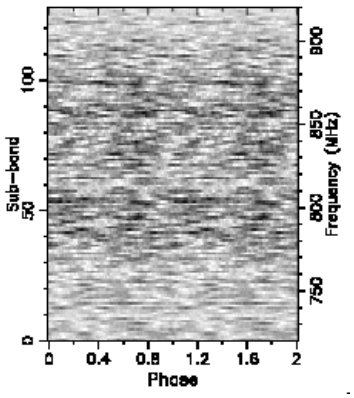

(c) Frequency and subbands graph of prepfold routine.

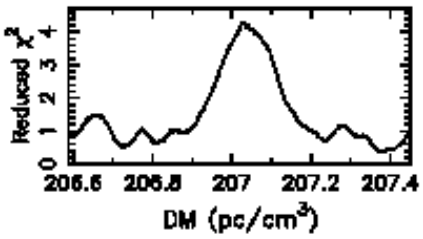

(d) Dispersion measure graph of prepfold routine.

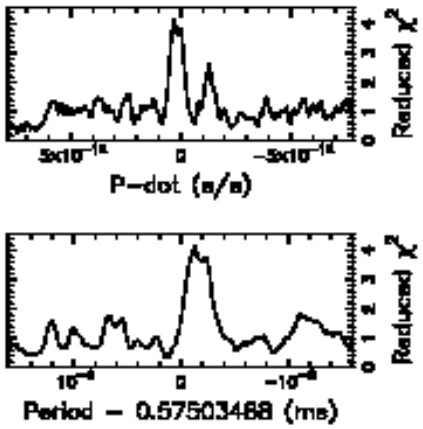

(e) Period and period derivative graph of prepfold routine

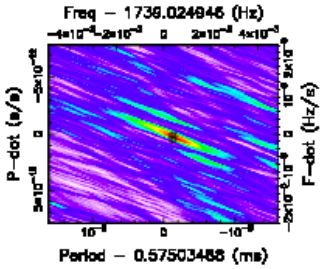

(f) Result of combination of period and period derivative graph

Figure 3.7: (a) Subintegrations graph - dark vertical lines in this graph indicate strong signal. (b) Pulse profile graph - peaks represent the portions of the observation where the signal that may represent a pulsar is present. (c) Prepfold frequency vs subband graph - represents signals in the form of dark vertical lines. (d) Prepfold DM vs reduced χ^2 graph. (e) Prepfold period and period derivative graph - Shows how well the period of the pulsar was measured. True pulsars exhibit a sharp peak on the $\dot{P}$ and reduced χ^2 graph.(f) A single, well defined region of red signifies a potential pulsar candidate in this graph.

3.4 Analysis of the output of prepfold

Millions of optimized, folded candidates are generated over the course of a large scale pulsar survey. Despite the thorough RFI mitigation and sophisticated searching strategies employed, the overwhelming majority of candidates are not of astrophysical origin. Finding the relatively small number of pulsars, especially the faint, previously undiscovered ones, is exceptionally challenging. Folding produces a pulse profile that can be viewed to decide the appropriate candidates for follow up.

There are several sections into which the prepfold plots are divided. The main categories are the search information section at the top-right which consists of textual data and the graphical section which presents information about the structure of the pulse.

The graphical section can be broken down into four subcategories. They are :

- Subintegration and pulse profile
- Frequency and subbands
- Dispersion measure and
- Period and period derivative.

Each of the above subcategories consists of one or more graphs which help the reviewer to determine its viability as a potential pulse profile of an actual pulsar. These graphs are explained in more details in the following sections.

3.4.1 Subintegration and pulse profile

One of the most important section of the PRESTO plot is the subintegration and pulse profile. This set of graphs provide a visual representation of the strength of the signal over time and phase as shown in figure 3.7a. The subintegration plot represents the strength of the signal at a point in time of a portion of the data within the measured pulse. Each bin is shaded with a grayscale value where the white indicates absence of signal and darker

bins indicate stronger signal.

The X-axis is the phase of the candidate pulsar, which encompasses two full rotations of the candidate pulsar. The Y-axis is the time in seconds from the start of the observation. Dark vertical lines in the time series occur from the start to the end of the observation represent pulsars as the signal remained strong at that phase throughout the observations. Absence of these dark vertical lines helps to classify the candidate as RFI.

Figure 3.7b represents the strength of the pulse as a function of phase. It is the integrations of the results of the sub-folds within the subintegrations plot as shown in 3.7a. The spikes in the graph represent portion of the period within the observed signal that could represent the pulsar beam pointing toward the telescope while the rest of the graph displays background noise. Absence of sharp peaks makes the candidate potential RFI. However, we also expect broad peaks from millisecond pulsars, hence, this diagnostic plot is not enough. So, we also investigate the other plots in order to detect a potential pulsar.

3.4.2 Frequency and subbands

RFI is exhibited by pulsars typically across a broad spectrum. The plot 3.7c helps display the strength of the signal across the frequency. This graph is structured very similarly to the subintegrations graph in that data are still discretized and darker bins represent stronger signal strength.

However, the Y-axis of the graph has been replaced with frequency and shows the observation frequency range over which the signal has been observed. The signal is also broken down into subbands as labeled along the left vertical axis. The shaded bits represent the power collected in a single subband over the duration of the entire observation. We should be able to see the increase in signal strength at the same phase location as that displayed in the time domain plot. This is represented by dark vertical lines in the graph.

There will be no dark vertical lines in case of RFI as the signals are not strong enough to be detected above the noise of the background.

3.4.3 Dispersion measure

The dispersion measure portion of the plot consist of one graph with an X-axis labeled DM and Y-axis of reduced χ^2 as shown in figure 3.7d.

DM is the integrated electron density along the line of sight between the pulsar and the Earth. The reduced χ^2 value is the statistical measure of the fitness of a model to a set of observations and tells us how well a particular DM dedisperses the signal.

The DM plot takes the range of DMs that prepfold searches over and tells us which DM is most likely to dedisperse the signal. The better the DM dedisperses the signal, the higher the χ^2 value. The top of the parabolic peak represents the best DM value and as you move further away from the peak of the parabola the DM is less likely to dedisperse the signal.

A DM that peaks at 0, means that the signal did not undergo any dispersion and hence is generated by electrical systems on Earth. The absence of a peak signifies that the signal is not coming from a distinct point in space and hence is not a pulsar.

3.4.4 Period and period derivative

The last subcategory of the candidate plot is of the period and period derivative plot and is a combination of three plots.

The first two graphs of figure 3.7e provide information relative to the rotational period of the pulsar. The period plot provides a measure of how well the period was measured while the $\dot{P}$ graph provides a measure of acceleration and deceleration of the pulsar period. The $\dot{P}$ graph should peak near 0 as a pulsar's rotation is generally stable. However, it is possible to see a $\dot{P}$ reading where the pulsars period is increasing or decreasing in

binary pulsar systems or pulsars with orbiting planets.

The third graph in figure 3.7f is a visual combination of the previous two graphs. It uses colour to represent the reduced χ^2 value, with the red end of the spectrum representing higher values. If the candidate is truly a potential pulsar, then only a single, well defined region of red should exist indicating good measurement of period and $\dot{P}$ instead of random RFI.

3.5 Candidate selection

Apart from carefully examining the PRESTO candidate plot output of prepfold, there are other criteria which should also be taken into account for choosing probable pulsar candidates.

For example, we also have to check that the S/N peaks at a non-zero DM. Peaking of DM at a zero value means that the signal does not undergo any dispersion and hence is considered possible RFI. The plot of reduced chi-squared value vs DM should have a profile similar to a Gaussian peak. Dark vertical lines in the time domain graph should be visible corresponding to the peaks in the pulse profile.

All of the aforementioned checks are done manually and some significant features may be missed. In order to carefully examine the candidates we resort to profile significance test that help us to provide a better analysis and results. As discussed before, profile significance is an important step to decide the possible candidates for follow up. Profile significance tests consists of checking chi-squared distribution, signal to noise ratio and significance of the signal as described in 3.2.5 of the candidates generated via our pipeline. It is generally done with the help of plots that help to visualize how one parameter change with the other. Once all the processes are done, the most suitable candidates are followed up.

3.6 Details of the observing parameters

The five nearby, young supernova remnants are observed with the Green Bank Telescope at an observing frequency of 820 MHz with 200 MHz bandwidth. The details about the receiver and filter mode of the telescope is discussed in 3.1. A minimum integration time of 5 minutes per pointings is taken. Table 3.1 shows the SNR, the number of pointings required to cover the whole remnant and the total amount of time the remnant has been surveyed, using two pointings per beam and a minimum integration time of 5 minutes per pointing.

SNR	No. of pointings	Total observation time (hr)
G53.6-2.2	2	4.5
G78.2+2.1	5	6.8
G89.0+4.7	10	7.0
G116.9+0.2	7	2.3
G156.2+5.7	27	7.3

Table 3.1: This shows the SNR, the number of pointings per SNR to cover the spatial extent of the SNR and the total time each remnant has been observed.

The observations cover the spatial extent of the SNR and provide better sensitivity than previous surveys. The details of the parameters and steps involved in our data processing is discussed in section 3.7.

3.7 Processing of the data : parameters and steps.

The various steps described in the previous sections are long and tedious to run manually, hence, they are automated via a python pipeline, which we describe below.

3.7.1 Data preparation

A dedispersion plan best suited for our searching is generated. After that, we searched and removed persistent radio frequency interference. After the removal or masking of RFI, we dedisperse the data into trial DMs. We then perform single precision Fast Fourier Transform (FFT) on the dedispersed data. The parameters involved in doing the above processes are listed below:

Parameter	Parameter value
DM step size	0.03
Low Channel (MHz)	720.097
Total bandwidth (MHz)	200
Number of channels	2048
Sample time (μs)	61.44
Maximum DM searched	2000
Number of subbands	128

Table 3.2: This table provides information about the data parameters for the survey. This specifies the information given by us for the data preparation part of the pipeline.

A DM of 2000 pc cm^{-3} is searched for the survey. The NE2001 model (Cordes and Lazio, 2002) predicts a maximum DM of 500 pc cm^{-3} for all of the remnants in this survey. In order to account for extra contribution of dispersion from the interstellar medium and the supernova remnants, we have chosen a high value of 2000 pc cm^{-3} in order to not miss any significant signals. A subband of 128 is chosen to strike a balance between computational efficiency without missing any prominent signals.

3.7.2 Candidate optimization

Periodicity search at zero acceleration is done after the above processes. The above parameters are used for periodicity search. The additional parameters used for acceleration are given in table 3.3.

Parameter	Parameter value
Number of harmonics	16
Sigma value	6.0

Table 3.3: The above table provides the parameters for candidate optimization part of the pipeline

After the acceleration search we sift the candidates. The sifting reads all the candidates and removes candidates that are duplicated in other acceleration files and with DM problems. It also removes candidates which are harmonically related to each other. It then writes the candidates to a text file. The text file contains the candidate name, DM, signal to noise ratio, sigma, number of harmonics summed and period. The parameters used for the sifting algorithm are listed below.

- Minimum DMs a candidate has to be detected to be considered good - 2
- Lowest DM to consider as a real pulsar - 3.0
- Ignore candidates with a sigma less than - 6.0
- Ignore candidates with a coherent power less than- 100.0
- How close a candidate has to another to be considered as the same candidate (Fourier bins) - 1.1
- Shortest period candidate to consider (s) - 0.0005
- Longest period candidate to consider (s) - 15.0
- Ignore any candidate where at least one harmonic does not exceed this power - 8.0

After obtaining the text files with the most probable pulsar candidates, we folded the data with the mask information (RFI) and known DM and period (from text file). The last part is analysing the folded profiles to identify potential pulsar candidates.

Chapter 4

Results

In this chapter, we present the results of our analysis. We provide examples of RFI, noise and pulsar prepfold plots and also discuss the analysis of the candidates with the help of corner plots. We also calculate the estimated flux density upper limits for the known pulsars in our field of view and of the studied supernova remnants.

4.1 Examples of prepfold plots

The folding of the candidates produces numerous prepfold plots. The approximate number of prepfold plots produced for each remnant is given in table 4.1. A total of approximately 12673 prepfold plots were generated in this survey.

SNR	No of pointings	Total number of prepfold plots
53.6-2.2	2	124
78.2+2.1	5	596
89.0+4.7	10	2705
116.9+0.2	7	2392
156.2+5.7	27	6856

Table 4.1: This shows the number of pointings and the number of prepfold plots that were generated for each SNR. All of the prepfold plots are carefully analysed and segregated into RFI, noise and possible pulsar candidates.

We carefully analyse the plots and divide them into potential RFI, noise and probable pulsar candidates. An example of each of these plots are discussed in this section.

4.1.1 Prepfold output - noise

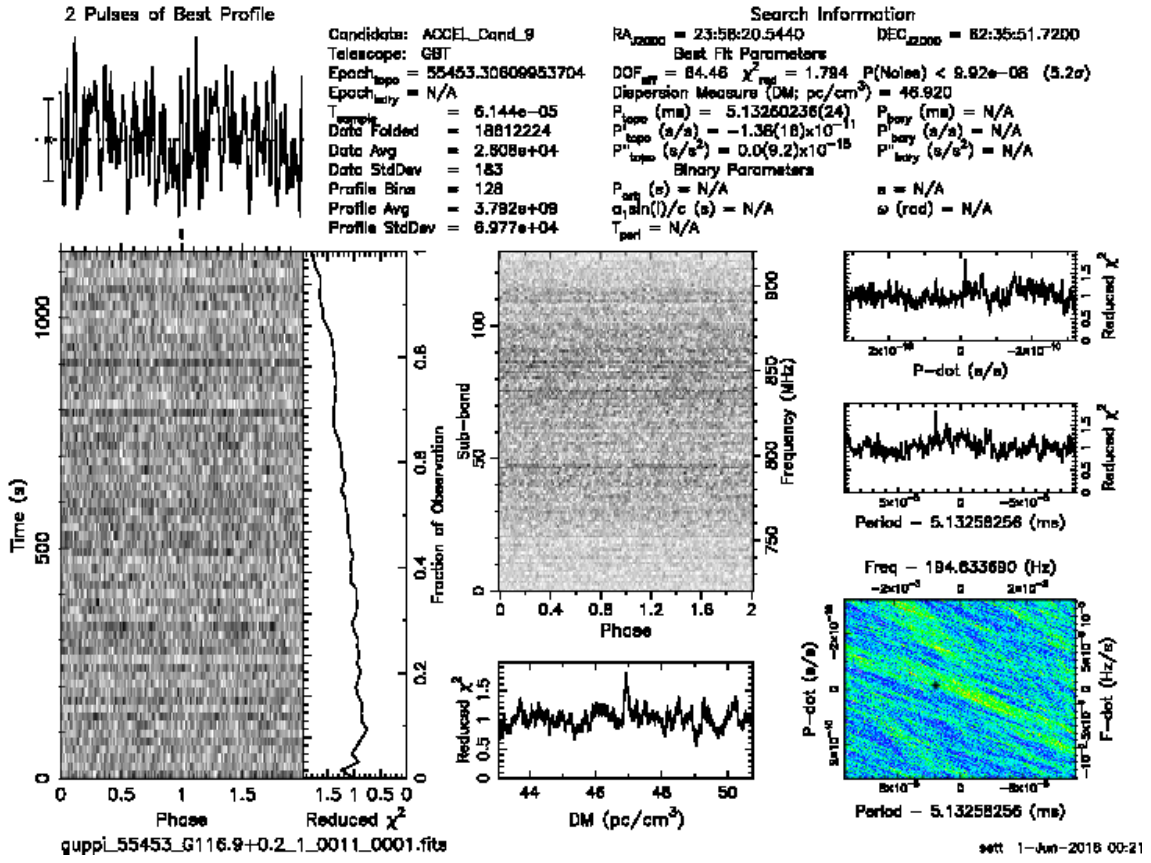

Figure 4.1: This is an example of prepfold plot which shows us that the candidate picked up by the pipeline is noise. There are no prominent peaks or dark vertical lines.

Figure 4.1 shows us the prepfold plot one candidate as picked up by the pipeline. We can clearly see that it is a promising candidate but not a significant one. It does not have any significant peaks in the pulse profile section. There are no dark vertical lines in the time domain plot. The reduced χ^2 vs DM graph does not have have a Gaussian profile. It is mainly a noisy pattern. Lastly, the period and the period derivative graph does not have one significant peak which is characteristic of a pulsar candidate.

4.1.2 Prepfold output - RFI

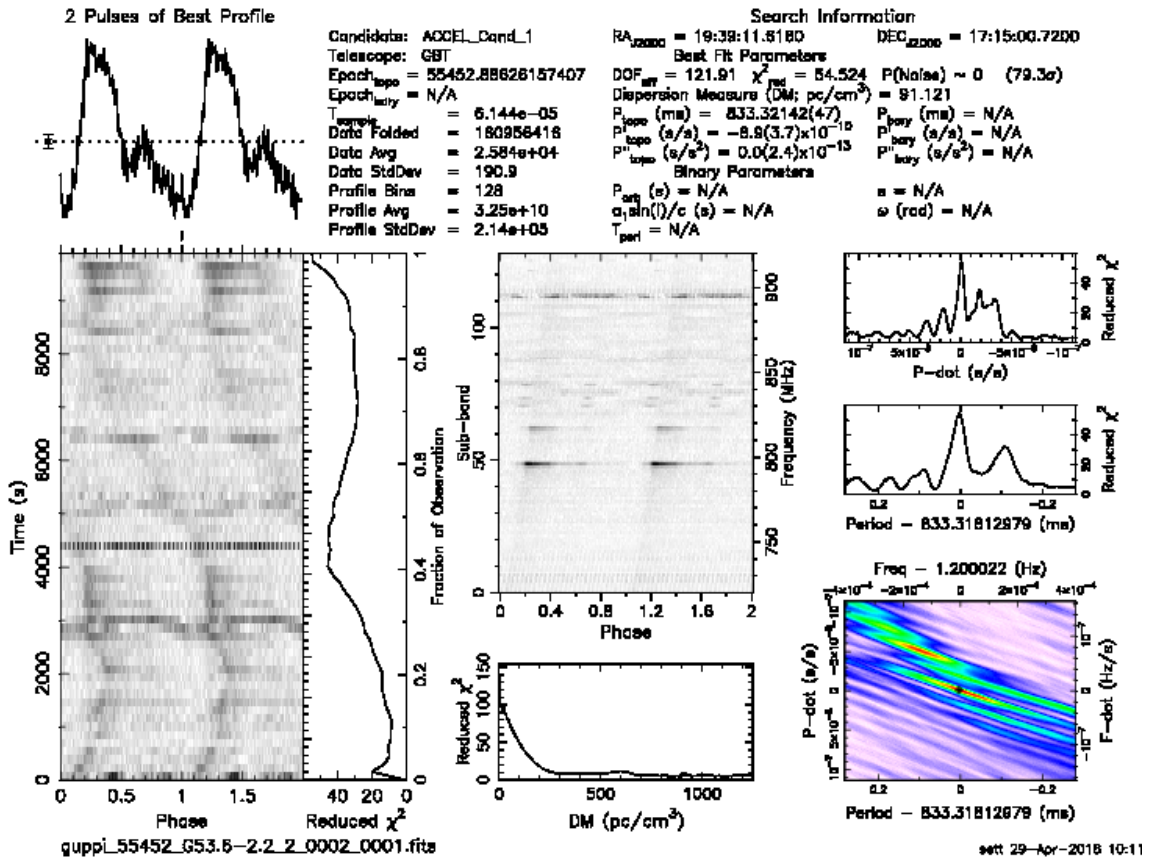

Figure 4.2: This is the resultant prepfold plot of a candidate which is potential RFI. We see that even the pulse profile may be similar to that of a pulsar, the graph of reduced χ^2 vs DM peaks at zero DM which is characteristic of potential RFI.

Figure 4.2 shows us the result of prepfold on one of the candidates. A quick look at the pulse profile may seem that it is a possible pulsar candidate. The dark features visible in the time domain plot indicate that a signal is present irrespective of the narrow frequency spikes but the "wiggles" show that it is time varying signal and hence is not pulsar like. If we look at the reduced χ^2 vs DM plot we see that the graph peaks at zero DM. It signifies that the signals are not dispersed at all and can be deduced to be coming from Earth or being man-made and hence is RFI. We can also see that there are dark lines in the time domain plot. But the dark lines are not constant in phase. The period and period derivative graph do not have a single peak. We also do not see a single prominent red region in the combined plots of period and period derivative. All of the above conclusions lead us to believe that even though the folding of the candidates may give us a prominent

peak, the analysis of the other parts of the graph shows that it is persistent radio frequency intereference which is imitating the pulse profile of a pulsar.

4.1.3 Prepfold output - Pulsar

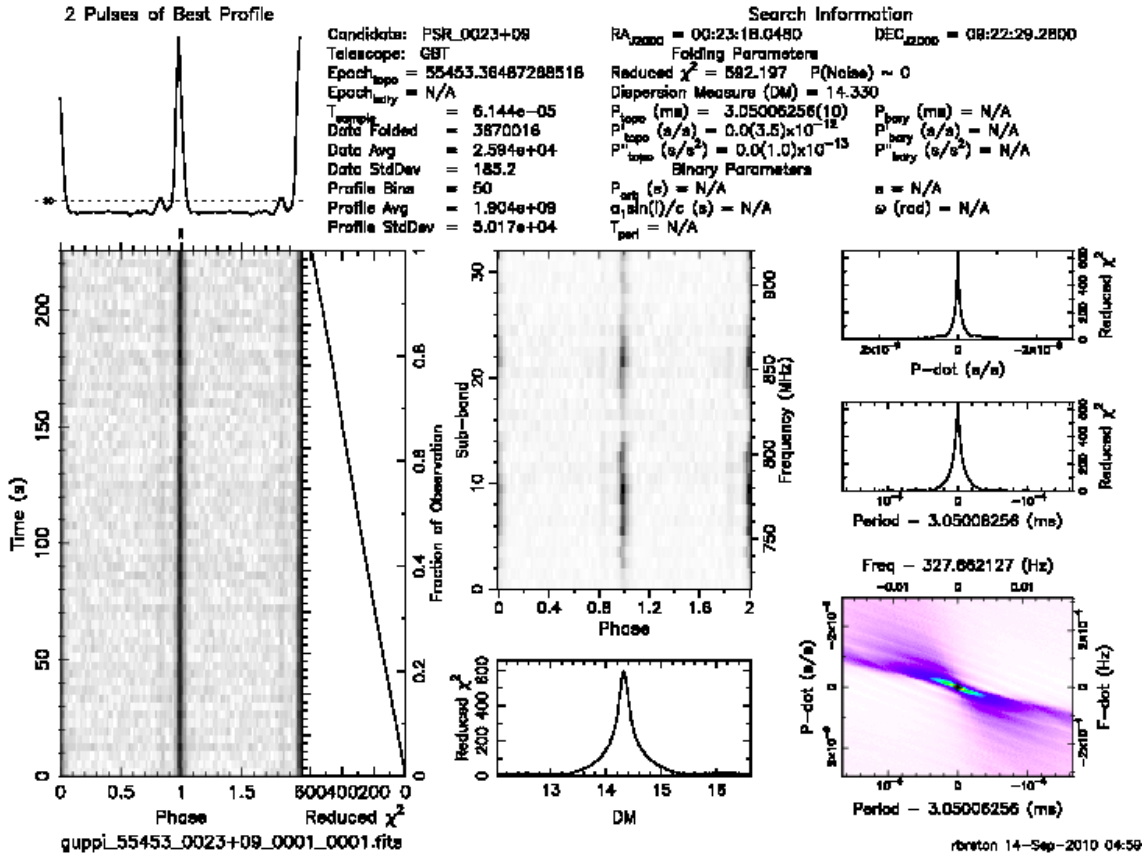

Figure 4.3: This is the folded profile of a test pulsar in our survey. It has one prominent peak in the profile along with dark vertical lines in the time domain plot.

Figure 4.3 shows us the folded profile of a test pulsar called PSR J0023+09. It has a very prominent peak with dark vertical lines in the time domain plots. The reduced χ^2 vs DM plot has a peak at a DM of 14.33. The shape of the DM curve changes depending on the period and width of the pulsar. The period and the period derivative graph has a peak at 0 and the combination of the graphs shows one red region which shows that the period and period derivative are measured very precisely. If we detect any of our candidates as a possible pulsar, the prepfold plot of the candidate will show very similar characteristics as the graph in figure 4.3.

4.2 Analysis of the pulsar candidates with the help of corner plots

As discussed in section 4.1, the prepfold routine gives us numerous folded pulse profiles of the candidates which are analysed to find any possible pulsar signal. However, it may happen that some candidates with a high significance are missed by our pipeline due to the parameter thresholds put in our folding pipeline. In order to provide completeness to our survey, we reanalyse our candidate list with the help of corner plots.

Corner plots are produced with the help of matplotlib in python. It uses matplotlib to visualize multidimensional samples of data using a scatterplot matrix and to highlight outliers. In these plots, the data is plotted to reveal covariances that helps us to understand the relation of one parameter to another in our observation.

Figure 4.4 is an example of the graphs produced by the corner plot routine of python with our candidate list parameters as input. For the graph in figure 4.4, the input paramerters were : signal to noise ratio, sigma, logarithmic value of dispersion measure and period.

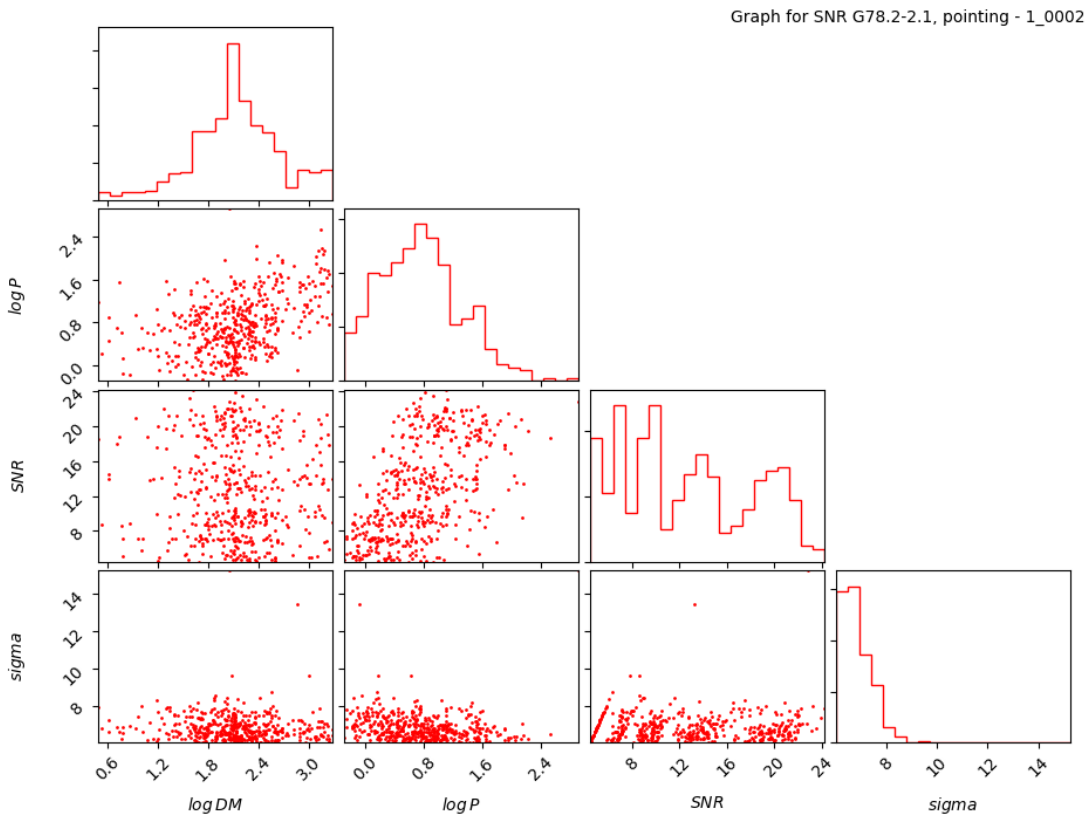

Figure 4.4: Corner plot of one of the pointing of remnant SNR G78.2+2.1. It shows how the parameters are related to one another. It helps us to get a better visualization of the relation betweeen one parameter with another.

We choose candidates with a highly significant sigma value, by analysing the sigma vs log DM part of 4.4. Any points that lie out of the distribution, are chosen and the values of sigma and log DM are noted. We search for similar points in the sigma vs log P graph in order to know the period of the candidates with high sigma. Once both DM and period are known for the outlying points, we fold the candidates with the DM and the period. The prepfold plots obtained along with the previous prepfold plots obtained from the pipeline are then categorized into noise, radio frequency interference and possible pulsar candidates.

The sigma vs SNR part is essential in choosing a minimum signal to noise ratio above which the possible candidates will be analysed and folded. A sensible signal to noise ratio below which most of the candidates lie is chosen to derive the upper limit on the pulsar flux density. It is the maximum flux density a pulsar could have and still remain

undetected by the survey.

4.3 Redections of known pulsars

Three pulsars, namely, J2021+4026, J2047+5029 and J0002+6216 have already been detected near remnants G78.2+2.1, G89.0+4.7 and G116.9+0.2 respectively (Abdo et al., 2009) (Janssen et al., 2009) (Clark et al., 2017).

J2021+4026 and J0002+6216 are believed to be associated with their respective remnant (Hui et al., 2015) (Zyuzin et al., 2018). The potential association of J2047+5029 with SNR G89.0+4.7 is discussed in section 5.4. J2047+5029 and J0002+6216 are radio loud and we were able to detect the former in our survey. However, we were unable to detect J0002+6216 as it was outside the pointings that covered G116.9+0.2. J2021+4026 is a gamma-ray pulsar that has been searched extensively in radio. However, it has never been detected in radio. We were also not able to find it in our survey even though the position of the pulsar as given by the X-ray observations lie in two of our pointings covering remnant G78.2+2.1. The pulsar is known to be radio-quiet and hence it was not detected in our survey. The ephemeris for the three pulsars are given in table 4.2 and redection of J2047+5029 is discussed in section 4.3.1. The flux density limits for the three pulsars are calculated in section 4.4.

PSR name	J2021+4026	J2047+5029	J0002+6216
RAJ (J2000)	20:21:29.99	20:47:54.6400	00:02:58.17
DECJ (J2000)	+40:26:45.1	+50:29:38.17	+62:16:09.4
P0 (sec)	0.26	0.44	0.11
P1	5.47E-14	4.17E-15	5.97E-15
F0 (Hz)	3.77	2.24	8.67
F1	-7.77E-13	-2.01-14	-0.45E-12

Table 4.2: This gives us the position, period, period derivative, frequency and frequency derivative of the three known pulsars.

4.3.1 Redetection of J2047+5029

PSR J2047+5029 was first detected at its second harmonic by Janssen et al. (2009) with the Westerbork Synthesis Radio Telescope at a central frequency of 328 Mhz with a bandwidth of 10 MHz. Previous surveys of HB 21 by Biggs and Lyne (1996) down to a limit of 13 mJy and by Lorimer et al. (1998) to a sensitivity limit of 0.66 mJy were unable to detect any pulsar in HB 21. This pulsar was redetected in our survey with the Green Bank Telescope at a central frequency of 820 MHz with a bandwidth of 200 MHz. The prepfold plot of the pulsar is given in figure 4.5.

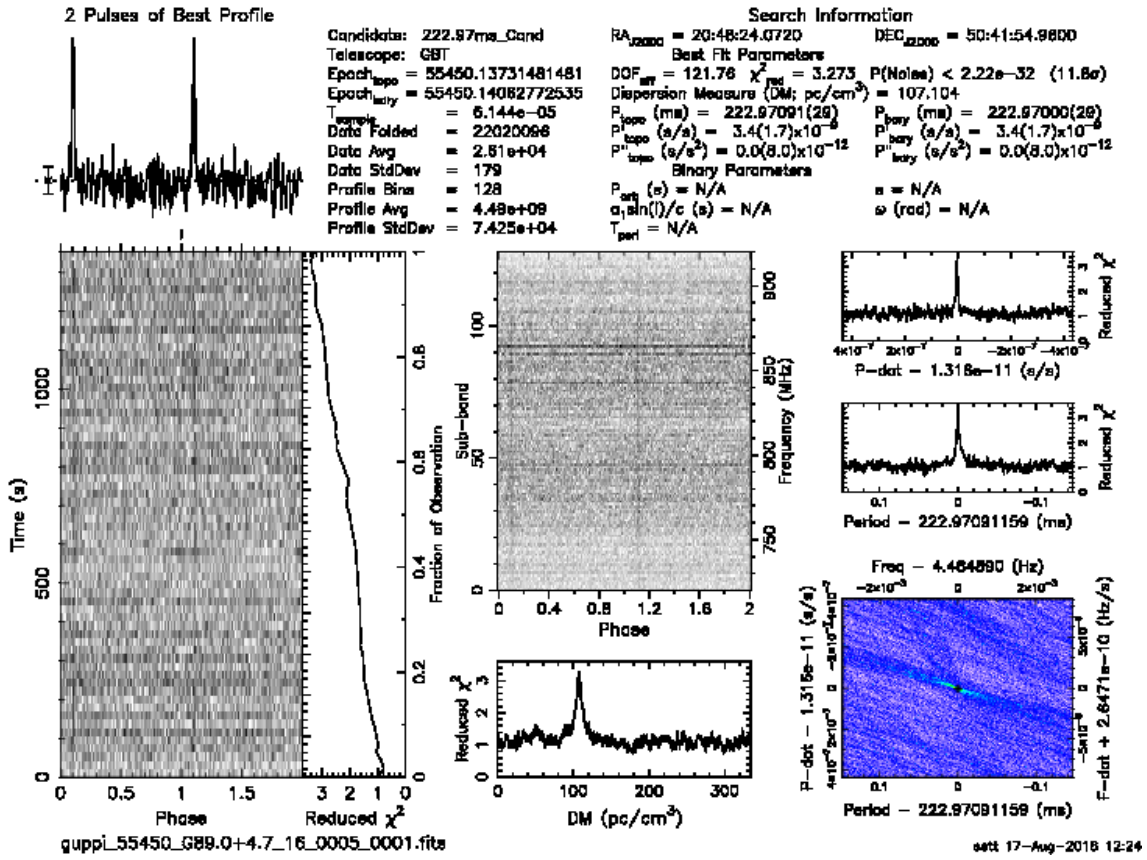

Figure 4.5: This is the prepfold output of the redected pulsar, PSR J2047+5029. It is redetected at its second harmonic at a DM 107.104.

Derived quantities like characteristic age, distance, surface magnetic field strength and spectral index are calculated from the pulsar. The table of the measured and derived quantities are given in table 4.3.

Measured quantities	
Right ascension (J2000)	20:48:24.0720
Declination (J2000)	50:41:54.9800
Pulse frequency (s^{-1})	2.24
Dispersion measure (cm^{-1} pc)	107.1

Derived Quantities	
Characteristic age (Myr)	1.7
Distance, d (kpc)	4.4
Surface magnetic field strength, B (10^{12} G)	1.4
Spectral index	-0.8

Table 4.3: This is the table of measured and derived quantities of PSR J2047+5029. The derived quantities are calculated with the help of the formula mentioned in 1.4

PSR J2047+5029, has a characterisitic age of 1.7 Myr and is at a distance of 4.4 kpc. It is relatively bright at 21 cm and has an approximate spectral index of -0.8. The interpulse of the pulsar is about 50 % as strong as the main pulse. It is detected at a dispersion measure of 107.1 pc cm^{-3} which is almost similar to the published DM of 107.6 pc cm^{-3} (Janssen et al., 2009). The possible association of PSR J2047+5029 with the supernova remnant G89.0+4.7 is discussed in section 5.3

4.4 Flux density upper limits of the survey

The flux density is estimated using the radiometer equation. It is given as (Lorimer and Kramer, 2004) :

$$S_{\text{min}} = \frac{K\sqrt{\text{D}}}{\sqrt{nBt}}\left(\frac{T_{\text{sys}} + T_{\text{sky}}}{G} + S_{\text{snr}}\right) \tag{4.1}$$

where K = $\beta\left(\frac{S}{N}\right)_{\text{min}}$ and is determined by the minimum signal to noise ratio at which the pulsar is detected or expected to be detected and β is a predetermined factor due to losses and system imperfections. For our survey, we assume the value of β is 1.5. D is the pulsar duty cycle. The pulsar duty cycle is the ratio of the width of the pulse to the period of the pulsar. For known pulsars, we can calculate the pulsar duty cycle, whereas we assume a value of 0.05 for unknown pulsars. The number of polarisations of our survey is denoted by n and has a value of 2, the bandwidth of observation is denoted by B and has a value of 200 MHz and t is the total integration time of our survey. The value of t depends on the total time the pulsar is observed. T_{sys} is the system temperature. The system temperature is the parameterisation of the noise generated by the parts of the telescope like antenna and receiver and is held as 29 K . T_{sky} is the sky temperature. The sky temperature is calculated from Haslam et al. (1982) assuming a spectral index of -2.6 and 820 MHz observing frequency. The gain of the telescope is assumed to be 2 K Jy^{-1} and is denoted by G. S_{SNR} is the flux of the supernova remnant per beam and is calculated using data from Green (2014).

4.4.1 Flux density upper limit estimates of the known pulsars

Using equation 4.1, we estimate the flux density limits of the pulsars. J0002+6216 was not in the field of view of our survey and hence the flux density limit for this pulsar cannot be estimated. The calculations of the limiting flux density for, J2021+4026 and J2047+5029 are discussed below.

Flux density upper limit estimate of PSR J2021+4026

J2021+4026 was present in one of the pointing of the remnant G78.2+2.1. Using equation 4.1 we are able to provide an estimate for the flux density limit for this pulsar. As the pulsar was not actually detected, we hold the pulsar duty cycle as 0.05. The pointing was observed for 5154.08 seconds with 2 polarizations and bandwidth of 200 MHz. The sky temperature for the pointing is 39.56K and the flux of the remnant for the beam is 22.13 Jy. Putting all these values in equation 4.1 we get a flux density limit of 0.08 mJy. The comparison of the estimated flux density limit of the pulsar in our survey with previous surveys of the pulsar is discussed in section 5.1.

Flux density estimate of PSR J2047+5029

J2047+5029 was redetected in our survey of SNR G89.0+4.7. We calculate the pulsar duty cycle by taking the ratio of the pulse width and the period of the pulsar. The pulse width of the pulsar is 0.02 in phase for one rotation. The pulse duty cycle, D, is 0.02. The pulsar was observed for 1610.65s with 2 polarizations and bandwidth of 200 MHz. The sky temperature for the pointing is 16.41 and the flux of the remnant for the beam is 3.71. The resultant flux density estimate of J2047+5029 is 0.3 mJy. The comparison of the resulting flux density of the pulsar in our survey with previous detections of the pulsar is discussed in section 5.1.

4.4.2 Flux density estimate of the five supernova remnants

We use equation 4.1 to calculate the flux densities of the pointings of the remnants. The value of D, T_{sys}, G, n and B remains the same for all the pointings. The varying parameters along with the calculated minimum flux density for each pointing is given in table 4.4.

SNR	Pointings	RA (deg)	DEC (deg)	t (s)	S_{min} (mJy)
53.6-2.2	2_0002	294.7984	17.2502	9986.03	0.07

continued on next page

Table 4.4 – continued from previous page

SNR	Pointings	RA (deg)	DEC (deg)	t (s)	S_{min} (mJy)
	1_0006	294.6112	17.315	6442.6	0.15
78.2+2.1	1_0002	305.1879	40.5646	5154.08	0.17
	2_0009	305.43	40.5645	5154.08	0.16
	4_0002	305.18	40.23	4187.69	0.13
	5_0010	305.0631	40.3999	5154.08	0.18
	7_0003	305.5	40.39	4831.95	0.10
89.0+4.7	0_0004	311.4998	51.0289	2899.17	0.08
	3_0006	311.0482	50.8637	2899.17	0.15
	4_0003	311.2005	50.6995	966.39	0.17
	4_0004	311.2	50.6997	2899.17	0.12
	5_0009	311.3497	50.8638	2577.04	0.14
	6_0008	311.0514	50.5348	2899.17	0.08
	9_0003	311.4999	50.6998	2899.17	0.13
	12_0007	311.9516	50.8637	2899.17	0.14
	16_0005	312.1003	50.6986	1610.65	0.24
	18_0005	311.5002	50.3709	2899.17	0.16
116.9+0.2	0_0002	359.792	62.4333	1288.52	0.23
	1_0011	359.5856	62.5977	1288.52	0.20
	2_0004	359.9978	62.5979	966.39	0.14
	4_0003	359.5875	62.2687	1288.52	0.1
	5_0005	359.3813	62.4327	1288.52	0.12
	7_0002	0.2023	62.4328	1288.52	0.23
	8_0006	359.9959	62.2688	966.39	0.29
156.2+5.7	0_0003	74.6668	51.8332	966.39	0.2
	1_0008	74.7995	52.32	966.39	0.19
	2_0010	74.5339	52.3202	966.39	0.15
	3_0004	74.6665	52.1625	966.39	0.11

continued on next page

Table 4.4 – continued from previous page

SNR	Pointings	RA (deg)	DEC (deg)	t (s)	S_{min} (mJy)
	4_0004	74.3573	52.1621	966.39	0.15
	5_0014	74.0458	52.1457	966.39	0.09
	6_0006	74.2035	51.9968	966.39	0.22
	7_0011	73.9062	51.987	644.26	0.09
	8_0004	74.0519	51.8316	966.39	0.24
	9_0008	74.2071	51.6678	966.39	0.11
	10_0010	73.9118	51.6747	966.39	0.29
	10_0011	73.912	51.6747	966.39	0.16
	12_0005	74.6668	51.5041	966.39	0.12
	13_0002	74.3591	51.8332	966.39	0.10
	14_0007	74.976	52.162	966.39	0.10
	16_0005	74.8209	51.9978	966.39	0.09
	17_0012	75.4272	51.987	966.39	0.13
	19_0013	75.288	52.1455	966.39	0.15
	20_0005	74.9743	51.8327	966.39	0.12
	22_0003	75.2814	51.8317	966.39	0.15
	23_0008	74.5132	51.6686	966.39	0.19
	25_0007	74.8202	51.6687	966.39	0.16
	26_0015	74.0542	51.5179	966.39	0.16
	28_0006	74.3612	51.5039	966.39	0.22
	31_0009	74.7968	51.3464	966.39	0.12
	32_0009	74.9717	51.5039	966.39	0.22
	35_0013	74.4215	51.6749	966.39	0.18

Table 4.4: This table shows the pointings, the positions of the pointings, the total time each pointing is observed and the total flux density estimate of each pointing. The flux density estimate of the pointings are calculated using equation 4.1. It is an approximation of the flux density limit. Any pulsar in our pointings with a flux density higher than the value of S_{min} should be detected by our survey.

Figures 4.6 to 4.10 shows plots for the five remnants with the number of pointings and the flux density estimates for the pointings. These plots helps us to visualize the spatial coverage of the remnants and the minimum flux density estimates of the pointings. The pointings are overlaid on VLA radio images of the supernova remnants. The pointings for individual remnants are represented by circles with the size of the circles representing the beam width at half power and the colour determined by the minimum flux density limit estimates of the pointings.

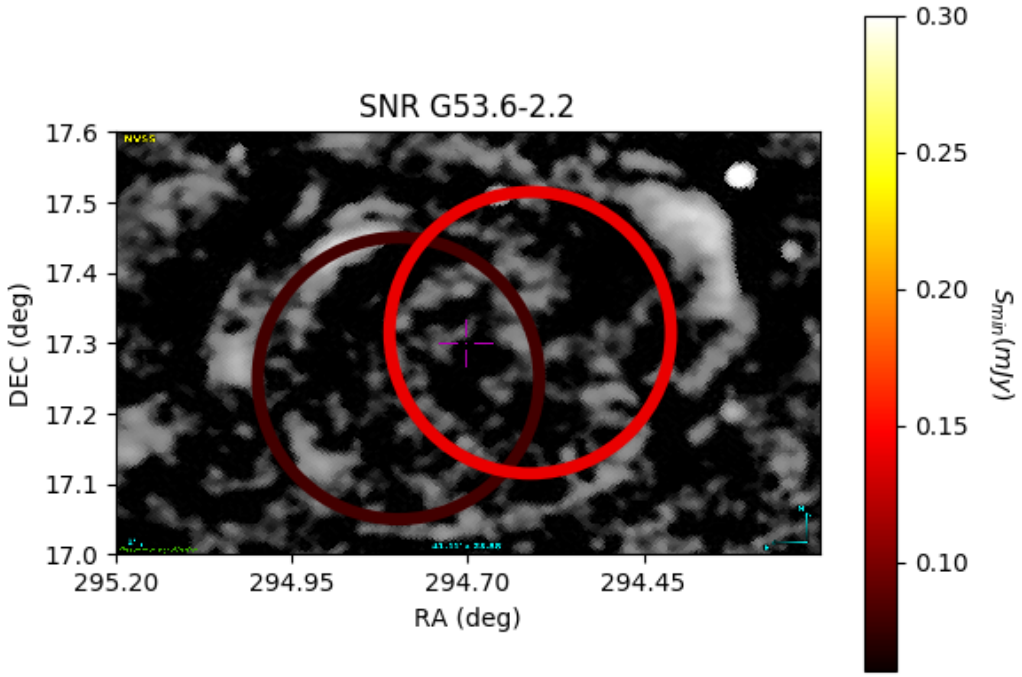

Figure 4.6: SNR G53.6-2.2. It has 2 pointings represented by circles overlaid on the VLA radio image covering the whole remnant. The size of the circles represent the beam width at half power. Both the pointings have a moderately low flux density limit.

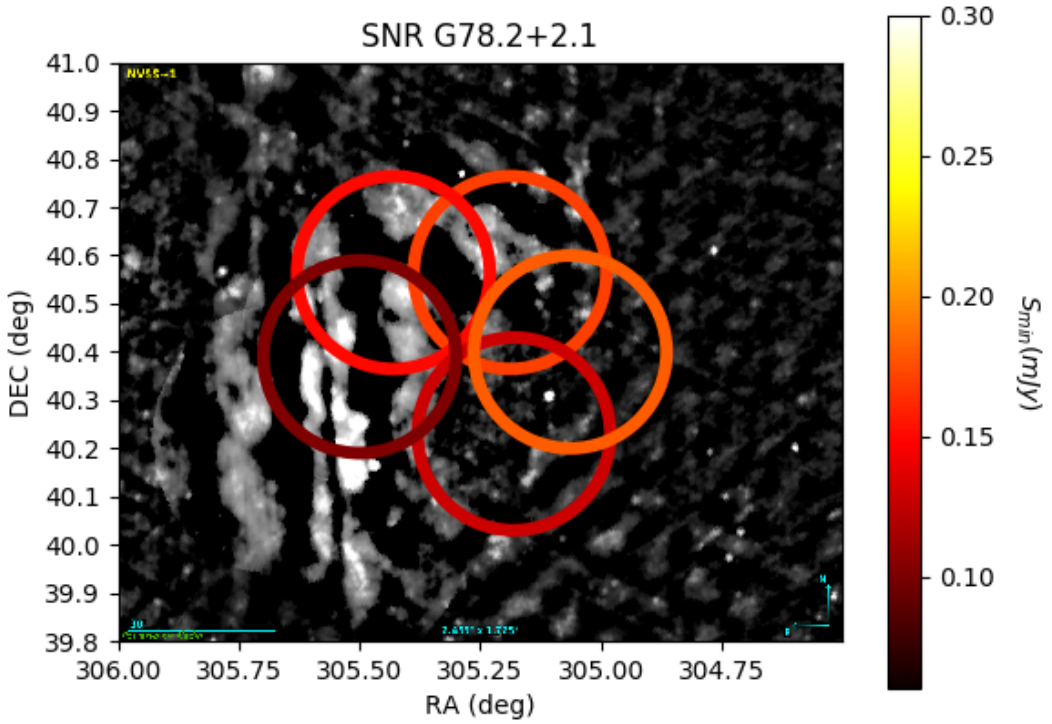

Figure 4.7: SNR G78.2+2.1. It has 5 pointings represented by circles overlaid on the VLA radio image covering the whole remnant. The size of the circles represent the beam width at half power. Two out of the five pointings have a low flux density threshold.

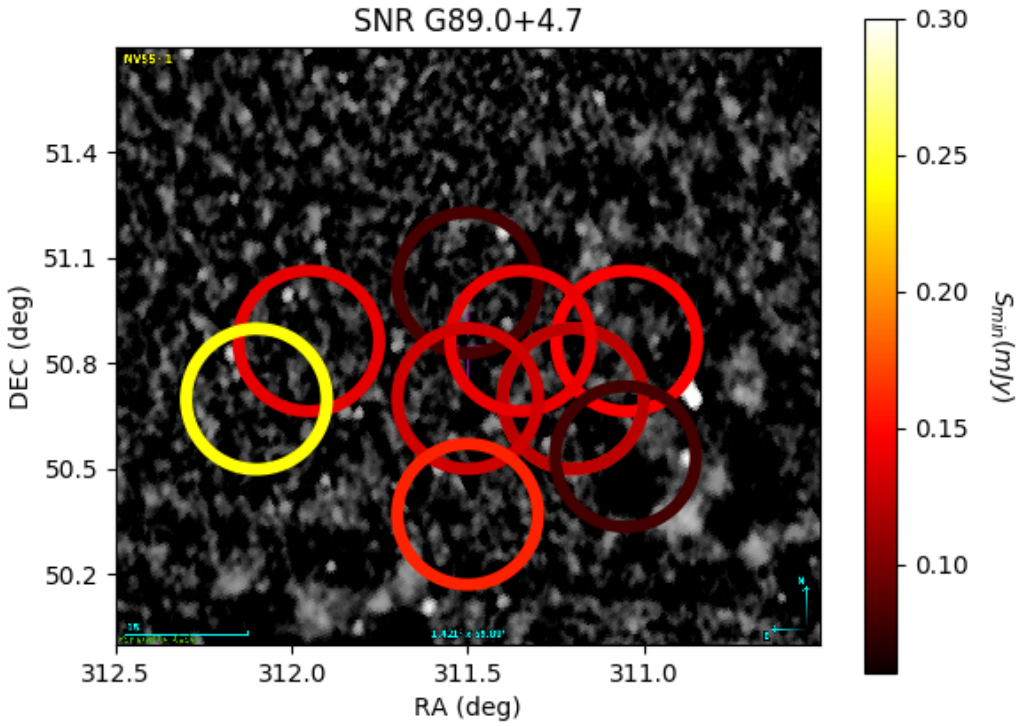

Figure 4.8: SNR G89.0+4.7. It has 9 pointings represented by circles overlaid on the VLA radio image covering the whole remnant. The size of the circles represent the beam width at half power. Two pointings have a low flux density limits and hence are most sensitive. Six of them have a medium flux density. One of the pointings have a high flux density. The pointings with the high flux density threshold has a high minimum detectable signal to noise ratio.

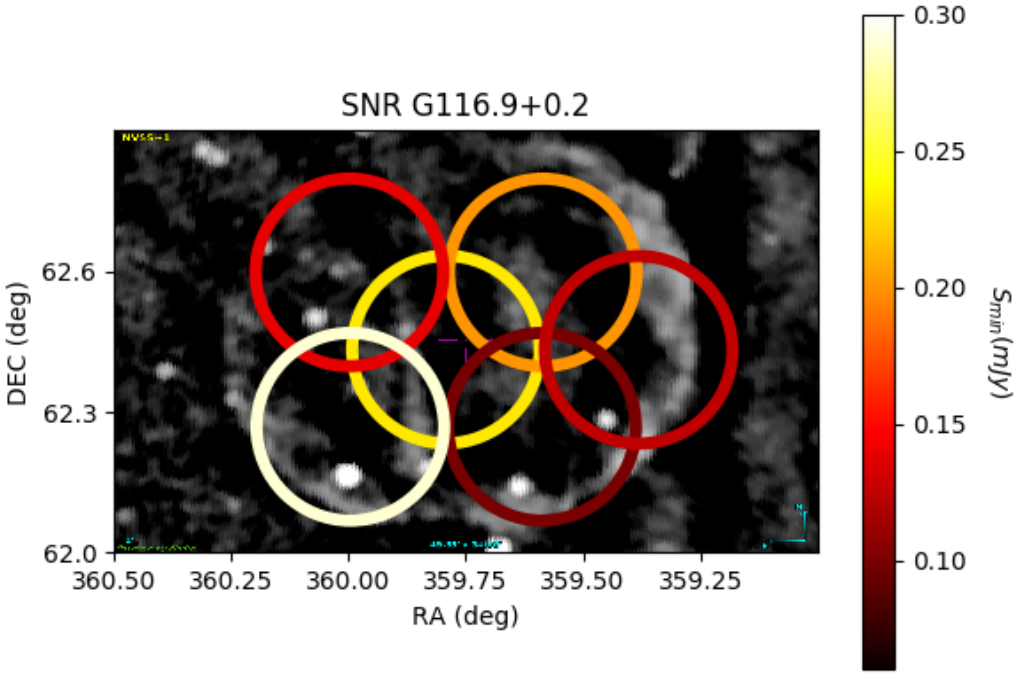

Figure 4.9: SNR G116.9+0.2. It has 6 pointings represented by circles overlaid on the VLA radio image covering the whole remnant. The size of the circles represent the beam width at half power. This remnant has a wide range of flux density thresholds. One of the pointings has a very low flux density and is the msot sensitive while two have medium flux density. One of them, marked in yellow have a moderately high flux density and the pointing marked in white has a very high flux density and hence least sensitive. These variations can be accounted for by either the varying observation time or the varying minimum detectable signal to noise ratio.

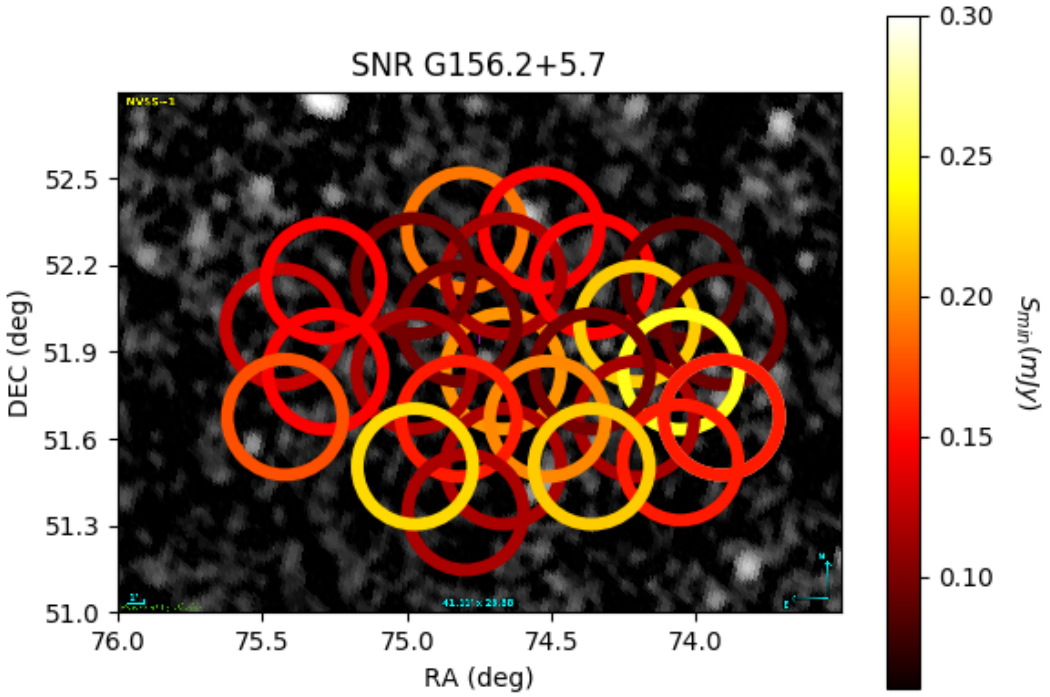

Figure 4.10: SNR G156.2+5.7. It has 27 pointings represented with circles overlaid on the VLA radio image covering the whole remnant. The size of the circles represent the beam width at half power. Most of the pointings have a flux density threshold range of small to medium. Three of the pointings have a moderately high flux density and are the least sensitive.

In figure 4.6 to 4.10 , we can see that the five remnants require different number of pointings to cover the area of the SNRs. The number of pointings needed depend on the size of the remnant. We can clearly see that G53.6-2.2 needed lesser pointings as compared to G156.2+5.7 because of larger size of the latter.

We take an average of S_{min} of the pointings for the SNR in order to report a average flux density of the survey for each remnant.

SNR	Number of pointings	Total observation time (hr)	Average S_{min} (mJy)
53.6-2.2	2	4.5	0.11
78.2+2.1	5	6.8	0.15
89.0+4.7	10	7.0	0.14
116.9+0.2	7	2.3	0.19
156.2+5.7	27	7.3	0.16

Table 4.5: This shows us the number of pointings, total observation time and the average flux density threshold of the supernova remnants studied in the survey.

Table 4.5 shows the remnant along with the number of pointings and the average flux sensitivity for each of the remnant. The comparison of the flux sensitivity of our surveys with selected previous surveys of the remnants is discussed in 5.2.

Chapter 5

Discussion and conclusion

In this chapter, we discuss the various results stated in chapter 4.

5.1 Comparison of calculated flux densities with the known flux densities of the pulsars.

5.1.1 J2021+4026

The flux sensitivity limit is calculated as 0.08 mJy as shown in 4.4.1. The pulsar has been studied earlier in various papers. We present the comparison between (Becker et al., 2004) and (Trepl et al., 2010).

(Becker et al., 2004) performed a deep search of radio pulsation from J2021+4026 using GBT. The observations were made at a center frequency of 820 MHz with a total bandwidth of 48 MHz. The 4 hr data was dedispersed upto a DM of 300 pc cm^{-3}. The sensitivity limit of the survey was found to be 0.2 mJy with a pulsar duty cycle of 0.04. The sensitivity limit of the survey is higher than that of the sensitivity limit of our survey.

(Trepl et al., 2010) performed a radio pulsation search for J2021+4026 with the 25-m radio telescope at Nanshan with an effective bandwidth of 42 MHz. The VLA sky survey database was also searched for any radio counterpart of the pulsar. The sensitivity of the survey is found to be 0.1 mJy for a pulsar duty cycle of 0.05. The sensitivity is lower than that of our survey.

5.1.2 J2047+5029

The flux density of the pulsar is calculated in section 4.4.1 and is 0.294 mJy. (Janssen et al., 2009) has studied the pulsar with the Westerbork Synthesis Radio Telescope at a frequency of 328 MHz. The flux density of the pulsar is found out to be 2.5 mJy which is very high as compared to that of our survey and hence our survey was ten times more sensitive towards the pulsar.

5.2 Comparison of flux density limits of the SNRs in this survey with previous surveys

The flux density of the five supernova remnants studied in our survey are calculated in section 4.4.2. In this section, we compare the calculated flux sensitivity limit of our survey with four successful previous surveys of supernova remnants, namely, (Gorham et al., 1996), (Biggs and Lyne, 1996), (Kaspi et al., 1996) and (Lorimer et al., 1998).

(Gorham et al., 1996) performed a survey of 18 supernova remnants using 305m Arecibo telescope. The duration of the observations varied from 20 minutes to 2 hours. The observing frequency was 430 MHz which was sometimes changed to 1420 MHz due to radio interference problems. The observation was sensitive to pulsars with minimum flux densities of 0.2 mJy. The values for pulsar parameters for determining the limits are P = 30 ms, DM = 300 pc cm^{-3} and duty cycle of 0.1. Comparing the sensitivity limit of the survey by (Gorham et al., 1996) with the sensitivity limit of our survey as calculated in section 4.4.2, we can clearly see that our survey is twice as sensitive as the survey by (Gorham et al., 1996).

(Biggs and Lyne, 1996) performed a targeted search for radio pulsars in 29 supernova remnants with the 76 m Lovell Telescope at 610 MHz. The SNRs were observed for 75 minutes. All the remnants in this survey have a minimum flux density more than 2 mJy at 400 MHz assuming a pulsar duty cycle of 5 % of the period of the pulsar. Comparing the sensitivity limit of the survey in (Biggs and Lyne, 1996), we can clearly see that our survey was two times more sensitive.

(Kaspi et al., 1996) searched 40 southern Galactic supernova remnant for radio pulsars at 436, 660 and 1520 MHz. Observations were made with the 64 m radio telescope at Parkes. The flux density of the survey was calculated assuming the minimum signal to noise ratio as 8, pulsar duty cycle as 5 %. The lowest flux density detected in the survey is

0.6 mJy which is higher than our survey which is capable of detecting flux density of 0.11 mJy. Hence our survey is five times more sensitive than (Kaspi et al., 1996).

(Lorimer et al., 1998) carried out a sensitive search for young pulsars associated with supernova remnants with the 76-m Lovell telescope at 606 mHz with a bandwidth of 8 MHz. The survey targeted 33 remnants in the northern hemisphere. The estimated flux sensitivity is 1 mJy with a 4 % duty cycle and is much more than that of our survey. It clearly shows that our survey is ten times more sensitive than (Lorimer et al., 1998).

5.3 Significance of redetection of pulsar and its possible association with the remnant

The redetection of pulsar J2047+5029 helped us to confirm that our survey was sensitive enough to detect a pulsar within the range of our observations. However, the association of PSR J2047+5029 with the remnant HB 21 seems unlikely even though the pulsar is located along the line of sight of the supernova remnant. The reasons discussed by Janssen et al. (2009) that disfavours the association of the pulsar with the remnant are discussed below.

Distance : As discussed in section 2.5 distance of SNR HB 21 is 1.7 kpc. Using the Cordes et al. (2002) model, a distance of 4.4 kpc is derived for the pulsar. The distance estimates for the pulsar and the remnant are at least different by a factor of 3. This argues in favour of an association.

Age : The age of the remnant as mentioned in section 2.5 is estimated to be 8000-15000 yr. However, the characteristic age of the pulsar is about 1.7 Myr; about two order of magnitudes larger. This is another evident reason for the pulsar to not be associated with the remnant. If a dipole braking model is assumed, the characteristic age is only considered as an upper limit to the real age of the pulsar. However, if we require the age of the pulsar to be consistent with the age of the SNR, we can conclude that the birth period of the pulsar would have been similar to the current period. The measured spin period of 0.445s for PSR J2047+5029 is not likely to be close to its spin period at birth unless the pulsar was born at a very slow period. Therefore, even though the characteristic age may not be considered as the real age of the pulsar, it has to be quite old to have slowed down to this period and hence strongly disfavours the association with the remnant.

5.4 Reasons behind the undetection of pulsar in the remnant

After careful analysis of the data with the help of graphs and folded profiles, we conclude that the five remnants do not have any radio pulsar associated with them at our observing frequency. However, they have at least two gamma-ray pulsar associations. Various reasons can be given for the unassociation of pulsars with supernova remnants. Some of the main reasons are discussed below.

It is possible that a pulsar lies in the remnant but the radiation may not be beamed towards the observer. The beaming fraction of a pulsar is the fraction of the sky covered by the radiation beam. It is assumed to be ≈ 20 % in the radio band (Manchester, 2007). A larger beaming fraction for the younge population of pulsar (Frail and Moffett, 1993) would make it more difficult for the pulsar to miss us in all five SNRs. However, observations show that the beams can be patchy and therefore the pulsar may be undetectable along our line of sight. However, it may be possible that the pulsar is visible in gamma ray due to its different beaming direction. We searched for any unidentified gamma-ray source associated with the five SNRs studied in our survey in the FERMI LAT catalogue of supernova remnants (Acero et al., 2016) and was unable to find any such source which could be classified as a pulsar other than the two gamma-ray pulsar associations already known.

Another possibility is that the pulsar magnetic field may take a considerable amount of time to develop. If the growth timescale is decades, then even a rapidly spinning neutron star could still be undetectable (Bonanno et al., 2005) (Blandford and Romani, 1988).

Another possible explanation can be that the neutron stars that are born in these processes are very faint. This is only possible if the cooling in these neutron stars is much more rapid than the standard cooling process assumed to operate in typical neutron

stars. Appearance of superfluidity in cooling stars when the internal temperature falls leads to a powerful neutrino emission which accelerates the neutron star cooling (Yakovlev et al., 2005). It would mean that the neutron star will be visible in X-ray as a source of emission. However, no unidentified X-ray emission from a point source has been associated with the five remnants studied in the survey (Seward, 2009). We can conclude that, any pulsar if present in these SNRs are too faint to be observed and has a different cooling process that the young, bright X-ray sources whose luminosities can be easily produced by standard cooling as shown in 5.1.

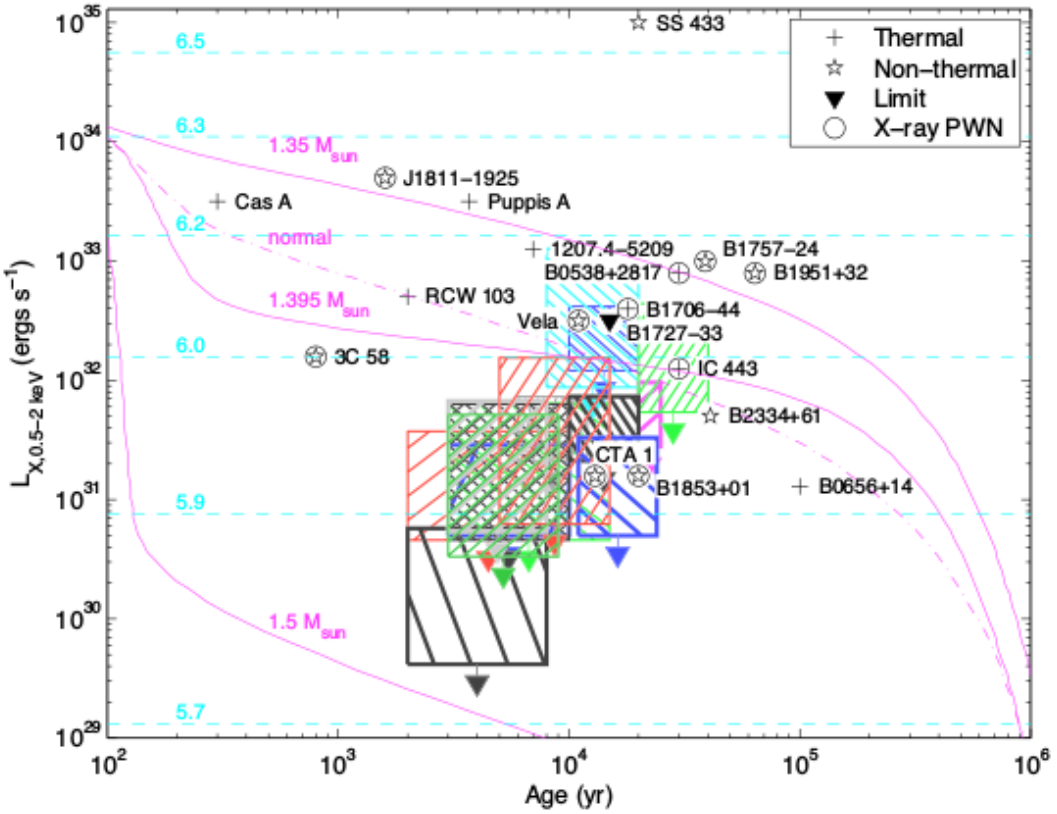

Figure 5.1: This figure shows the X-ray luminosities as a function of age for known neutron stars in SNRs (Shporer et al., 2010). Pluses indicate sources with primarily thermal emission. Stars indicate the sources with primarily non-thermal emission. Triangles are the upper limits. Sources with X-ray pulsar wind nebula are circled. The boxes show limits to blackbody emission in sources in empty SNRs. The solid lines show cooling curves for a range of masses in a 1p proton superfluid model and the dot-dashed line show a standard non-superfluid cooling for M = 1.35$\dot{M}$.

It may also happen that the particle acceleration mechanism in the neutron star never activated, thus rendering it permanently radio quiet. The neutron star may not be able

to emit any radiation because the magnetic field is too large (Baring, 2001). Conversely, it may be radio quiet because the polar cap potential drop is too low (Chen and Ruderman, 1993). The inability to produce electron-poisitron pair can also be a possible explanation for the absense of radio waves (Chen and Ruderman, 1993).

Even though most of the remnants studied are transparent at radio wavelengths, it is possible that the immediate environment of the central star has a relatively high gas density which would cause scattering and absorption of the emission from the central star (Staveley-Smith et al., 2014).

Another plausible explanation is that the neutron star formed in the supernova explosion has undergone a large velocity kick and is not in our viewing field anymore. The asymmetric form of a supernova is an explanation for such a velocity kick to the nascent pulsar. Such kicks may make it hard to associate the pulsar with a nearby supernova remnant (Lai, 2004). The velocity of the pulsar such that it escapes the remnant can be calculated from the angular size, distance and age of the remnant. Table 5.1 shows the velocities that a pulsar should have in every remnant for it to completely escape the remnant and not be detectable in our field of view.

SNR	Distance (pc)	Age (10^3 yr)	Velocity (km/s)
53.6-2.2	13.3	7	1900
78.2+2.1	13.087	7	1800
89.0+4.7	25.959	16	1600
116.9+0.2	7.912	7	1100
156.2+5.7	20.7935	15	1400

Table 5.1: It shows the velocity required by the pulsar to escape the remnant.

Typical velocities for young pulsars are about 1000 km s^{-1}. All the pulsar velocities stated in table 5.1 are higher than 1000 km s^{-1}. A pulsar may attain these high velocities as a result of supernova explosion during its formation. These large velocities may result in the pulsar escaping our field of view of observation.

5.5 Conclusions and future work

In this project, we studied nearby, young five supernova remnants in order to detect radio pulsars associated with them. The survey was done with the Green Bank Telescope at an observing frequency of 820 MHz with 200 MHz bandwidth. The data was corrected for radio frequency interference and carefully analysed for dispersion measures up to 2000 pc cm^{-3} with the help of the pulsar searching suite, PRESTO, developed by Ransom (2001). Our search was sensitive to isolated pulsars only as we searched at zero acceleration value. Resulting candidates were folded and analysed with the help of prepfold plots as well as profile significance test with the help of corner plots. Candidates with a high sigma value were folded again in order to recheck our input parameters for our data processing.

We were able to redetect, PSR J2047+5029, at a DM of 107.104 pc cm^{-3}. However, we were unable to associate the pulsar with the supernova remnant G89.0+4.7. We were unable to detect any other radio pulsar at our observing frequency in any of the remnants in our survey. The reasons for such unassociation are that the pulsar may not be beamed towards us, or the magnetic field of the pulsar is not strong enough to be detected yet. It may also happen that the pulsar is permanently radio quiet or the immediate environment of the pulsars absorbs or scatters the emission. Another possible explanation is that the pulsar may have acquired a velocity during the explosion and is not in our field of view anymore. These reasons are discussed in detail in 5.4 .

The flux density limits for the known pulsars in our field of view are calculated in section 4.4.1 and compared with the known flux density limits of the pulsars in section 5.1. The flux density of the SNR with the pointings and an overall flux density estimate for each SNR is calculated in section 4.4.2 and compared with the previous successful SNR surveys in section 5.2. We can conclude from the comparison that our survey is at least twice as sensitive than the previous targeted surveys of the five supernova remnants.

As discussed before, our analysis was sensitive to only isolated pulsars. Due to time constraints, we were unable to run an acceleration search which is sensitive to binary pulsars. We aim to perform an acceleration search in order to provide completeness to the whole survey.

Appendix A

A brief overview of the theory of supernova remnants

In this chapter we present a brief overview of the radio morphology of supernova remnant.

A.1 Radio morphology of SNR

The vast majority of SNRs in our Galaxy were first detected by radio observations. The morphology and brightness distribution in SNRs contain important information about the nature of the SNR and its possible hydrodynamical evolution. In effect, in radio waves SNRs exhibit an ample variety of shapes. For example, *blow out* : in which part of the shell appears to have expanded more rapidly than the rest or *barrel-shaped or bilateral* : SNRs characterized by a clear axis of symmetry, low level of emission along this axis, and two bright limbs on either sides (Kavanagh, P. J. et al., 2013). In the investigation of SNR morphologies, an additional complication is that the observed shape is a two-dimensional projection of a three-dimensional object and depends on their orientation with respect to the line of sight and projection effects.

A challenging question for decades is whether the SN type be determined by the radio morphology of the remnant. The great diversity of shapes observed in radio SNRs, reflects not only different properties of the progenitor star and of explosion mechanisms, but also echoes the properties of the ambient magnetic field and the matter distribution in the circumstellar and interstellar medium. Several attempts have been made to infer the type of supernovae on the basis of the observed remnants. In X-ray domain, Lopez et al. (2009) developed an observational method to characterize the type of explosion of young SNRs by measuring global and local morphological properties of the X-ray line and ther- mal emission in numerous young SNRs in our Galaxy and in the Large Magellanic Cloud, finding that the remnants of Type Ia SNe have statistically more spherical and mirror-symmetric thermal X-ray emission than SNRs coming from core-collapse origin.

The morphological criteria that seems to work for X-rays and IR to infer the SN type from the SNRs characteristics are not applicable to radio SNRs. One important reason that complicates the connection of a radio SNR with its precursor is that while X-rays may retain information about the characteristics of the exploded star, the complexity of the interaction between the shock front and the ejecta, circumstellar and interstellar matter,

can soon mask this information in the radio emission. Once the shock front sweeps up a certain amount of ambient gas, the radio synchrotron emission ignores the explosion properties and it is mostly conditioned by inhomogeneities in the surrounding medium, hydrodynamic instabilities in the flow, turbulence behind the shock, effects of magnetic fields, etc (Chevalier, 1982). Hence, the radio morphology alone does not provide a useful tool to distinguish between different types of SNe.

Appendix B

Some of the corner plots of the five remnants

In this chapter, we present the corner plots that were created by obtaining the values of dispersion measure, period, signal to noise ratio and sigma values of all the candidates of each pointing for the five remnants. The corner plots for each pointing are given in the sections below.

B.1 53.6-2.2

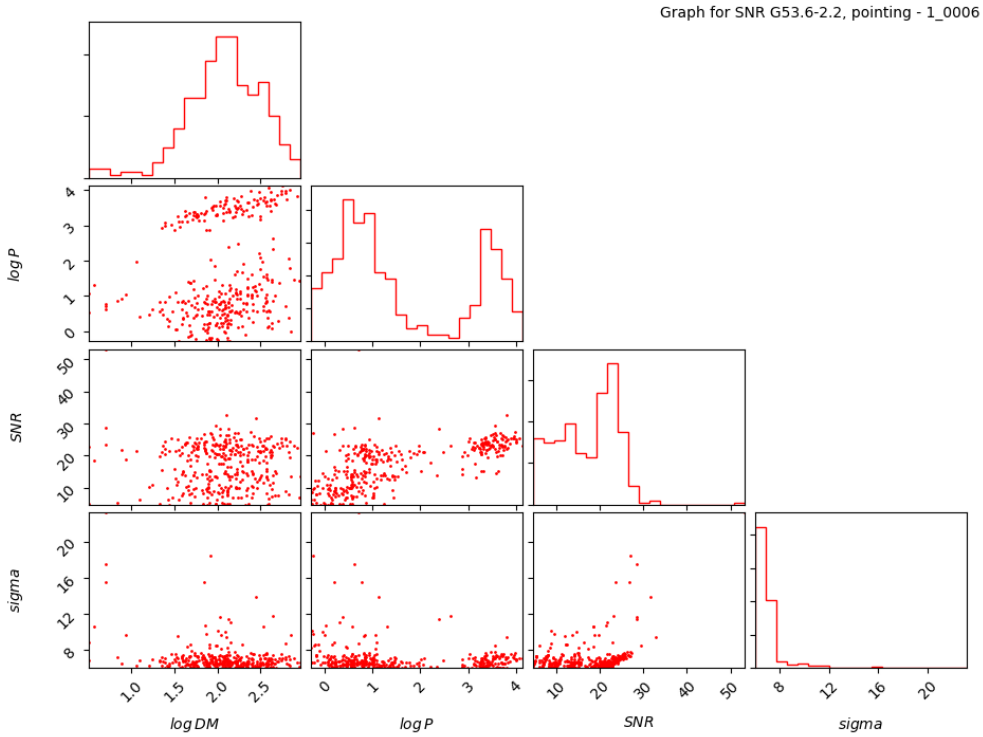

(a) Corner plot of G53.6-2.2, pointing 1_0006

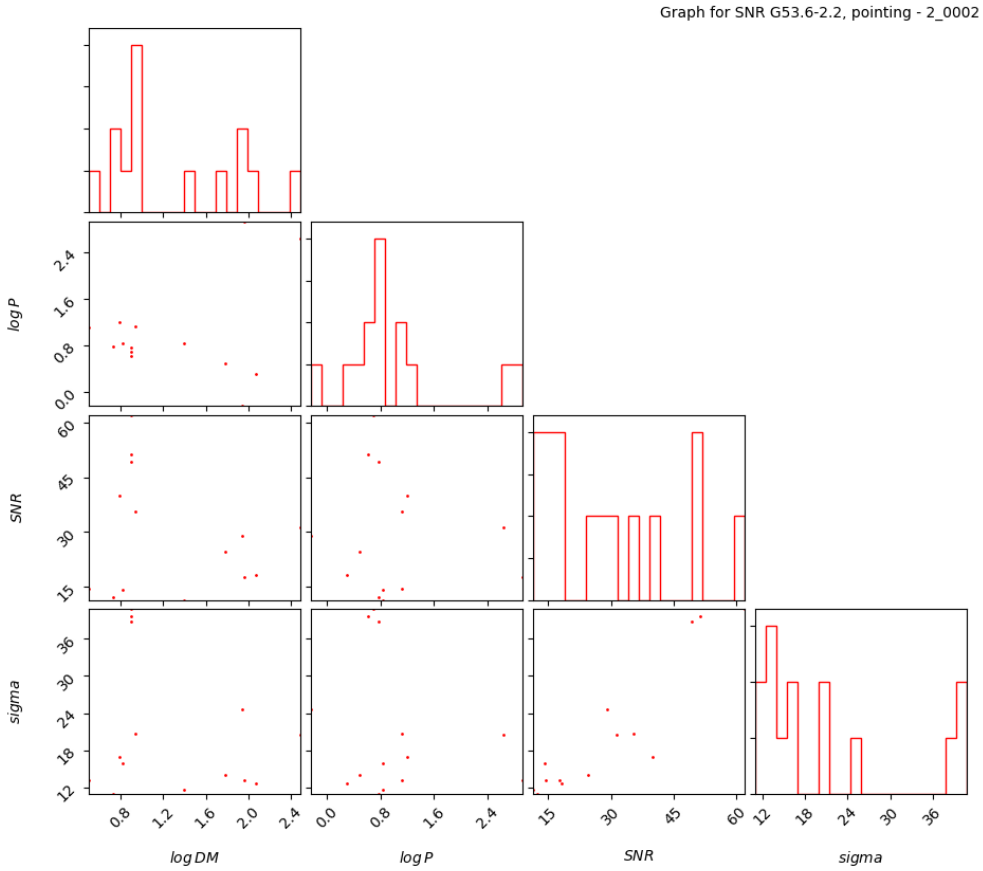

(b) Corner plot of G53.6-2.2, pointing 2_0002

B.2 78.2+2.1

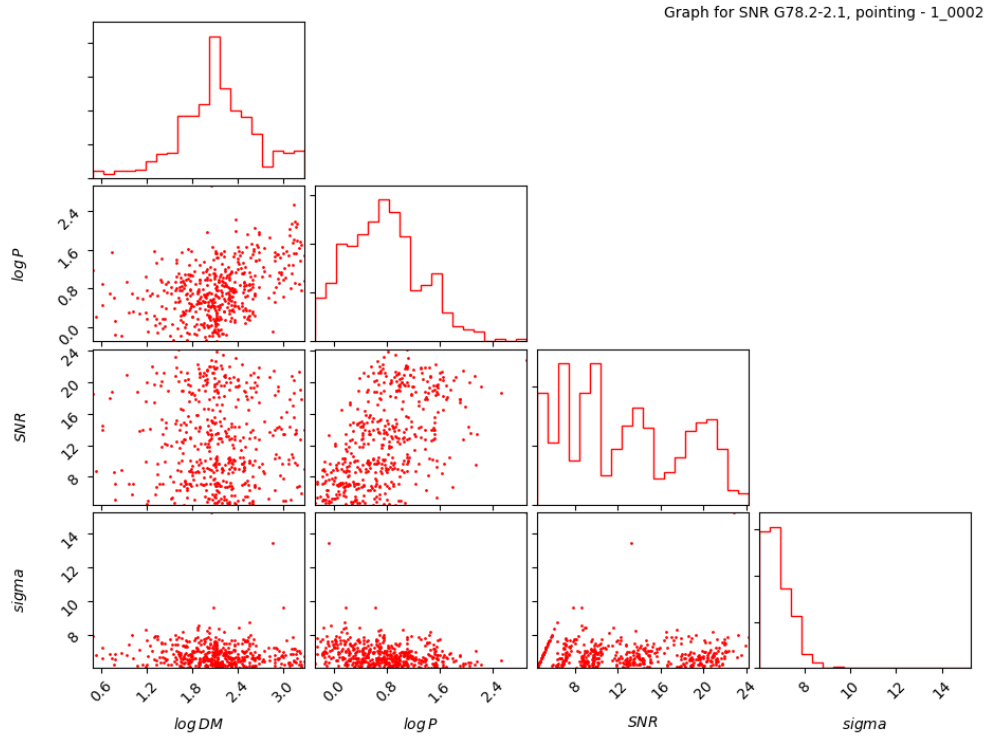

(a) Corner plot of G78.2+2.1, pointing 1_0002

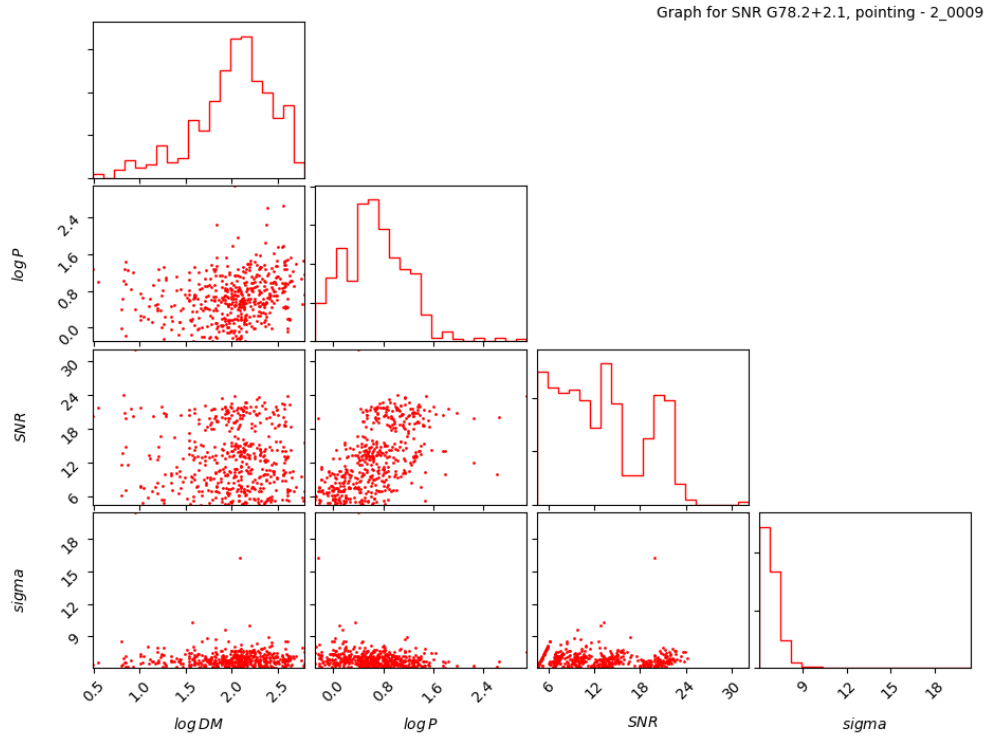

(b) Corner plot of G78.2+2.1, pointing 2_0009

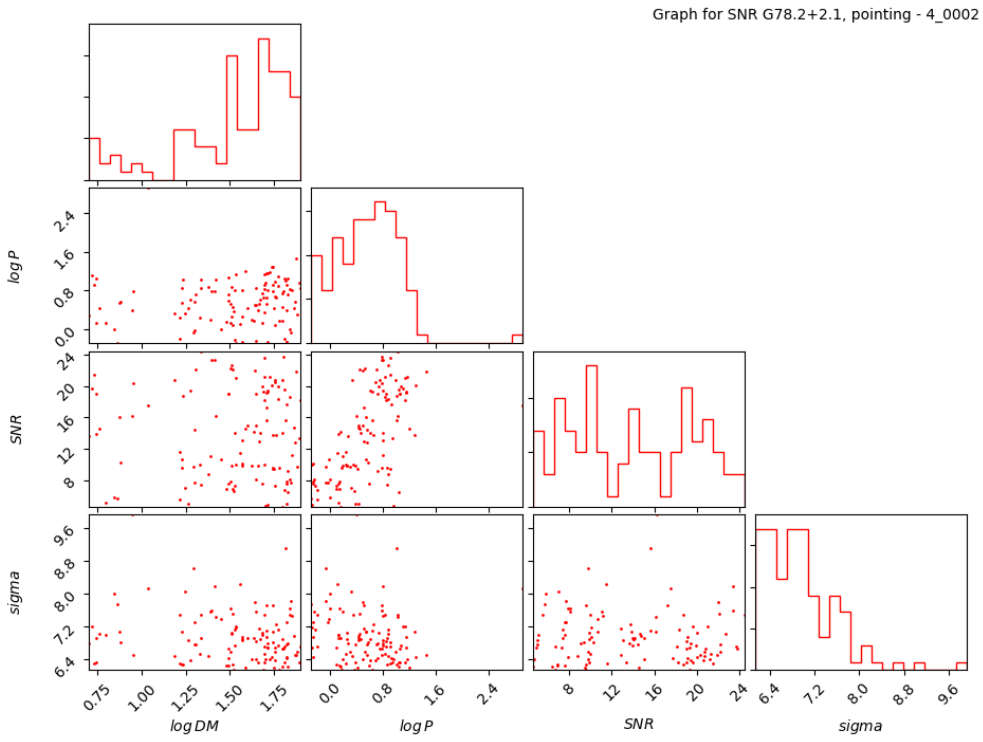

(a) Corner plot of G78.2+2.1, pointing 4_0002

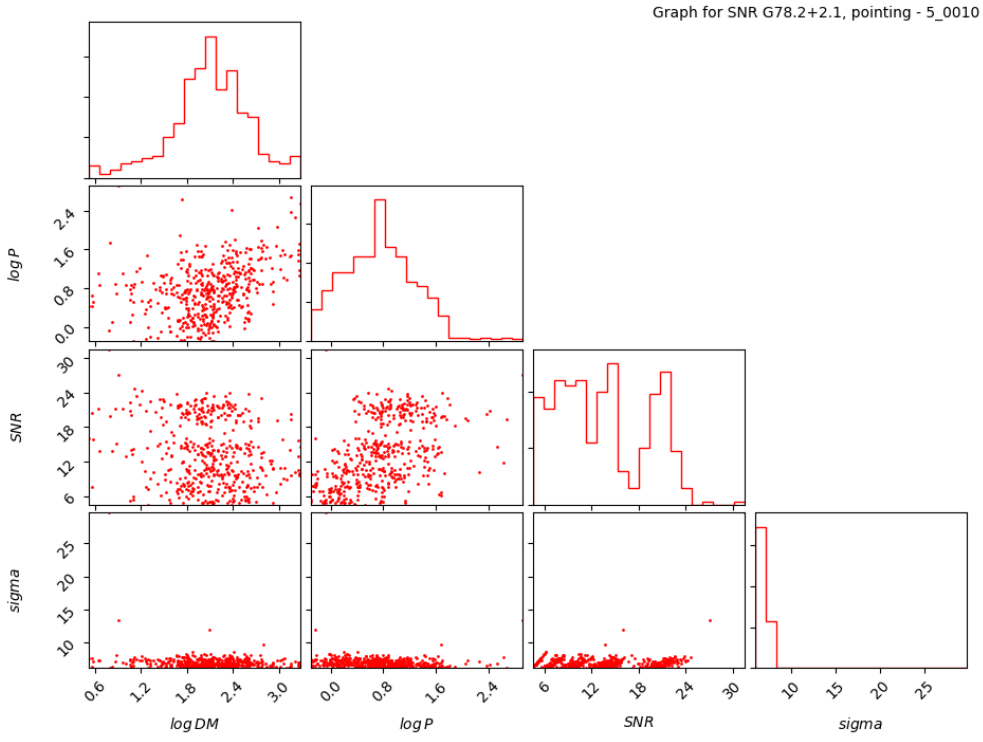

(b) Corner plot of G78.2+2.1, pointing 5_0010

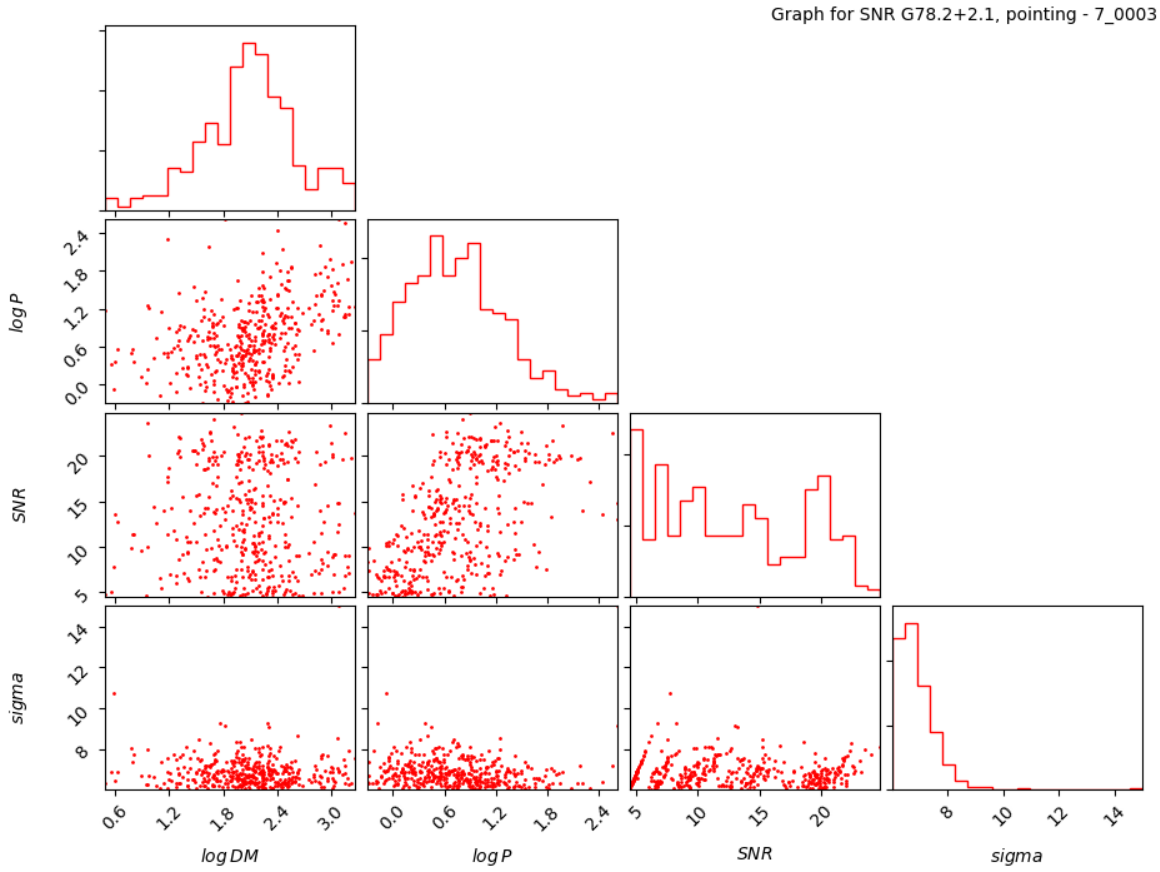

Figure B.4: Corner plot of G78.2+2.1, pointing 5_0003

B.3 89.0+4.7

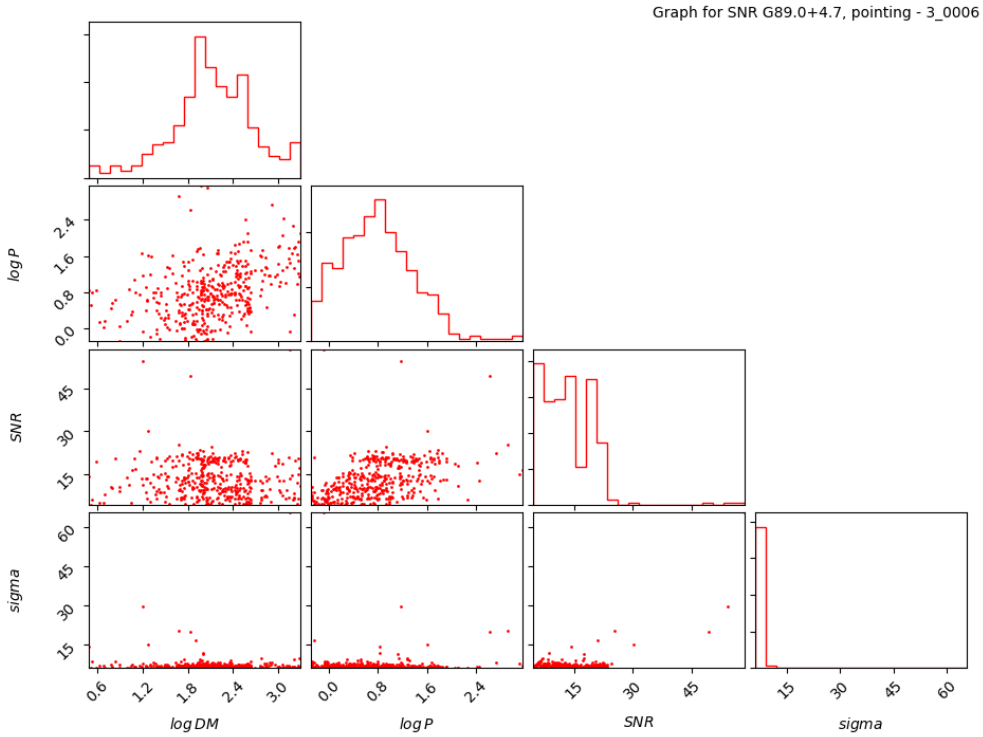

(a) Corner plot of G89.0+4.7, pointing 3_0006

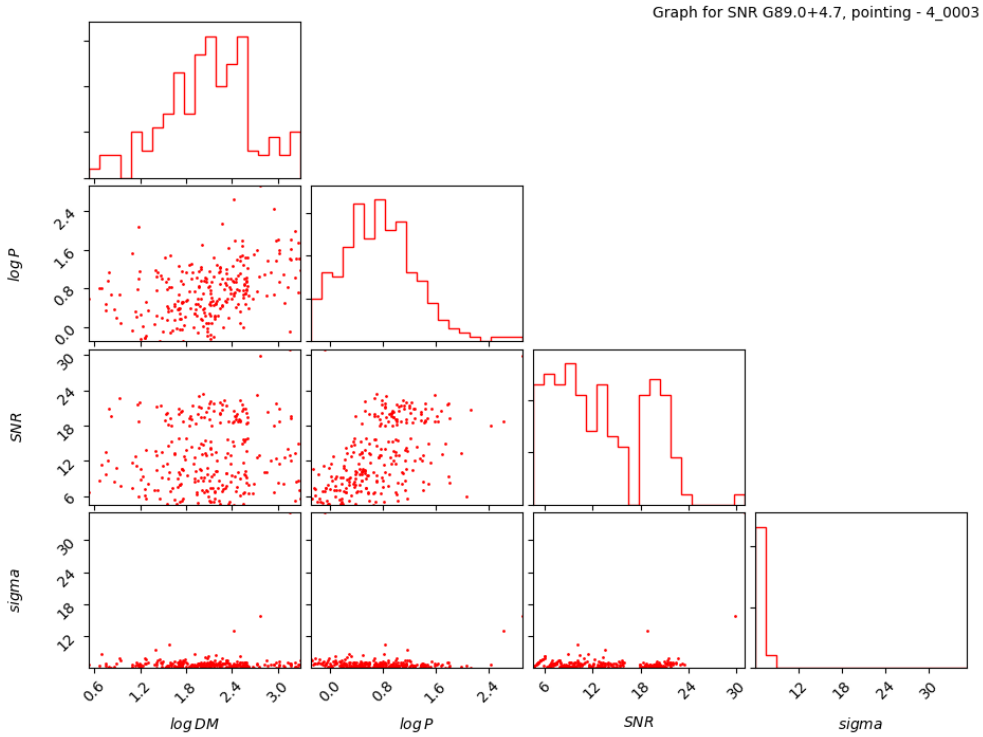

(b) Corner plot of G89.0+4.7, pointing 4_0003

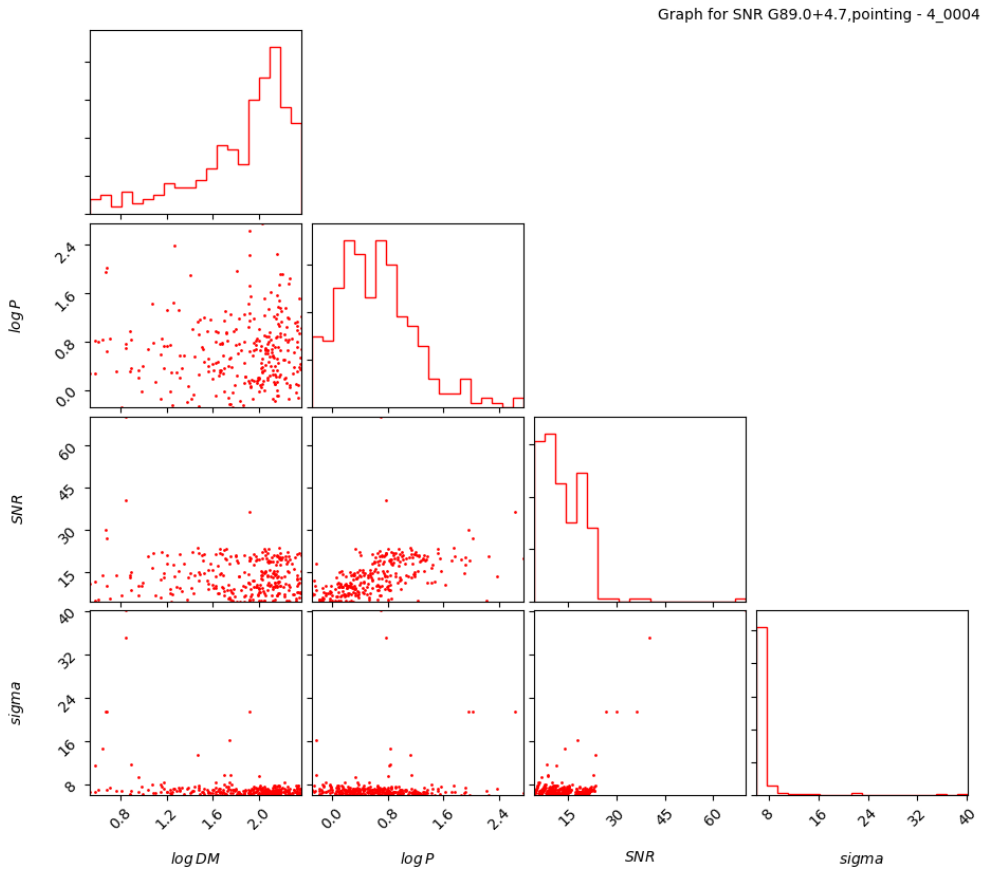

(a) Corner plot of G89.0+4.7, pointing 4_0004

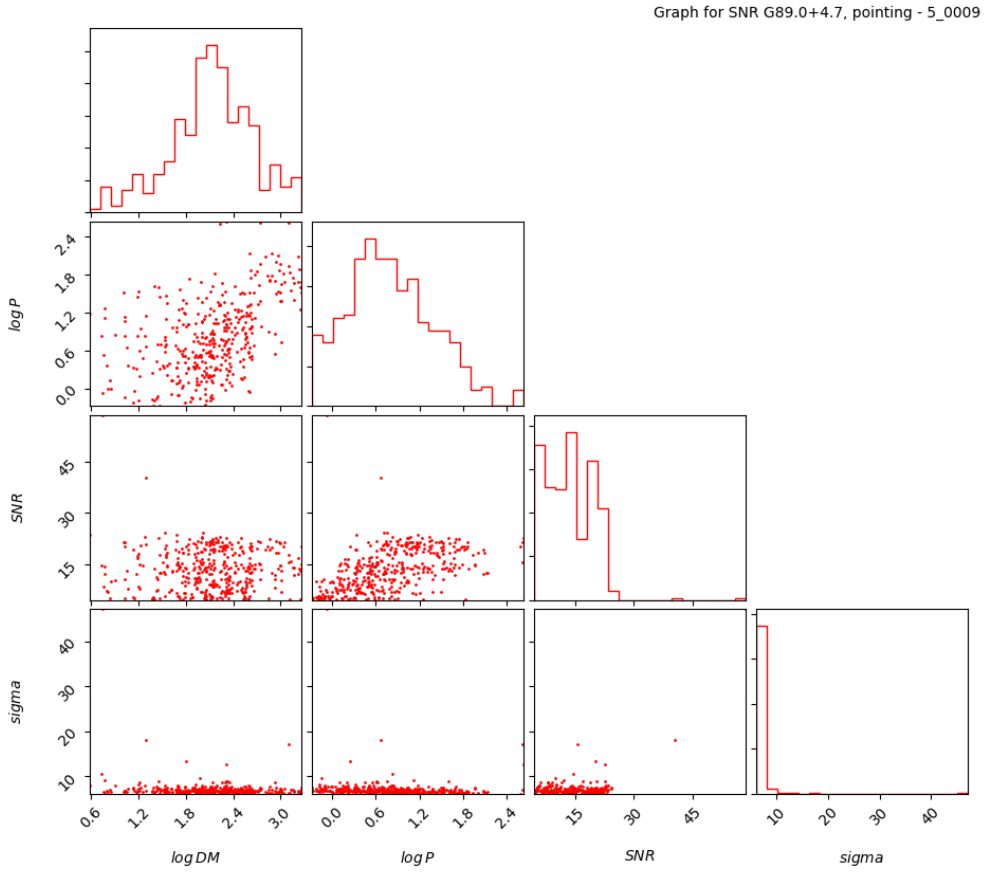

(b) Corner plot of G89.0+4.7, pointing 5_0009

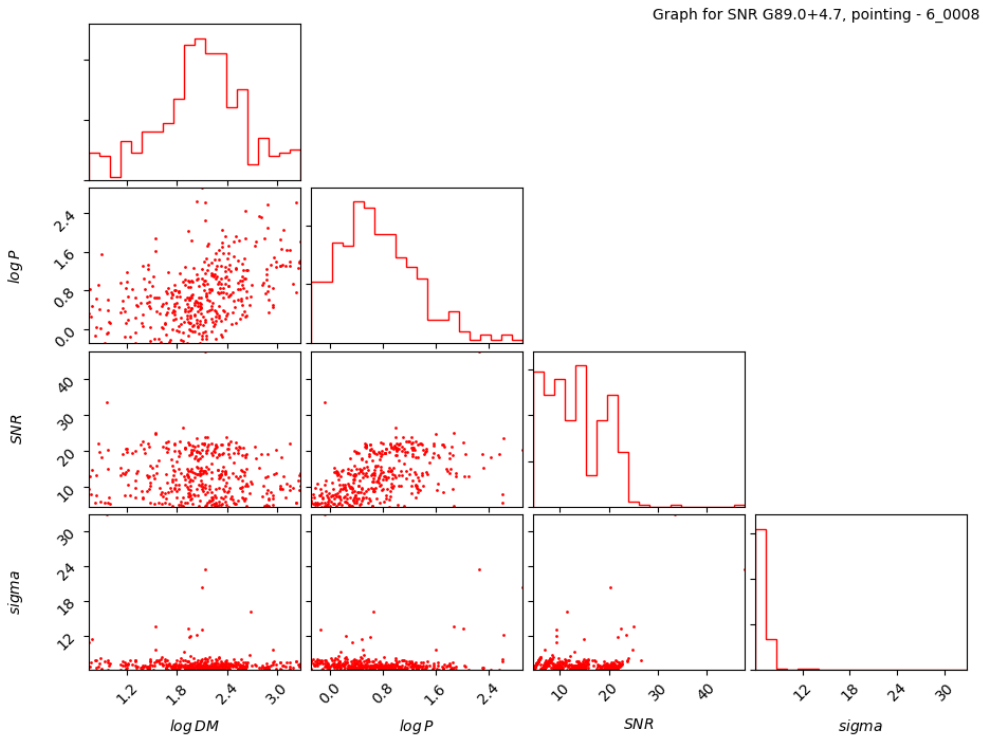

(a) Corner plot of G89.0+4.7, pointing 6_0008

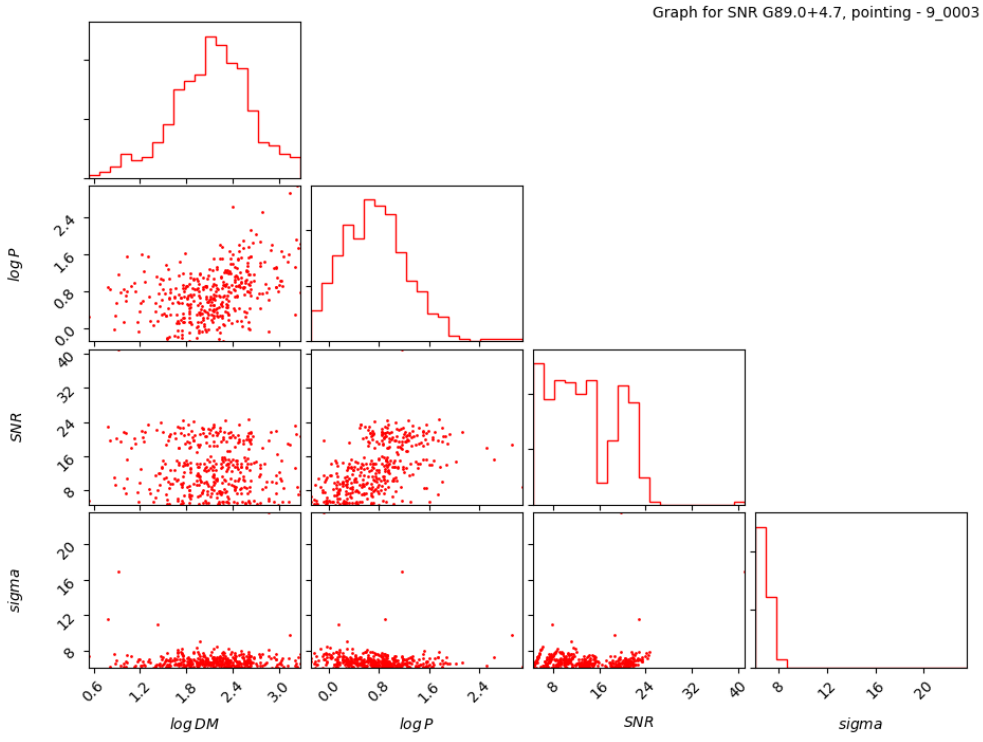

(b) Corner plot of G89.0+4.7, pointing 9_0003

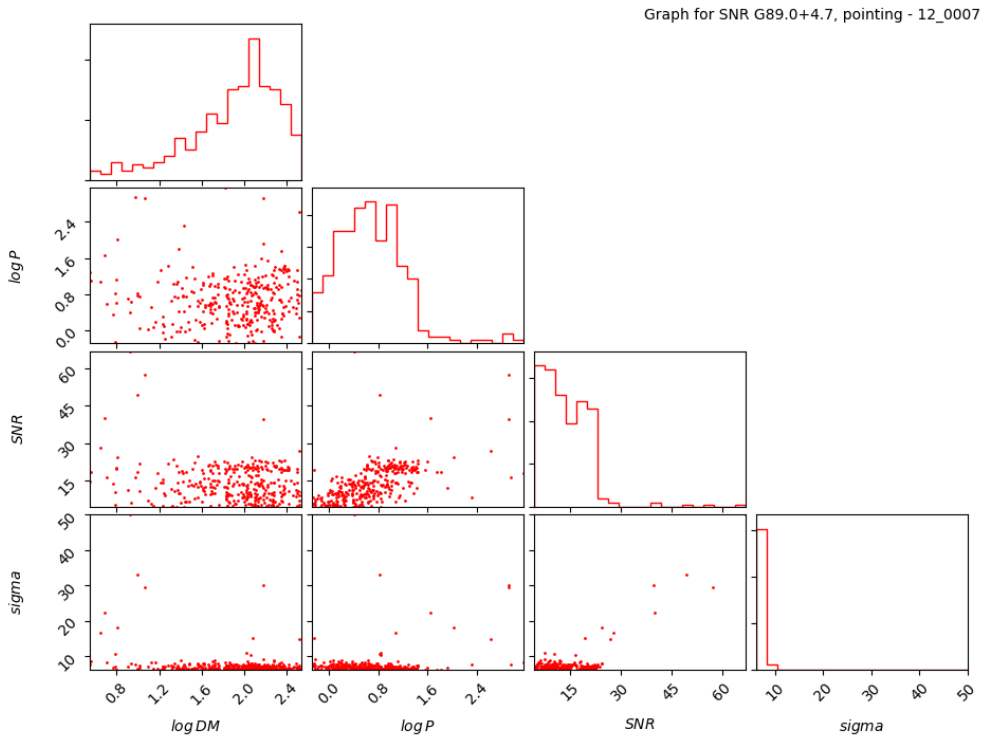

(a) Corner plot of G89.0+4.7, pointing 12_0007

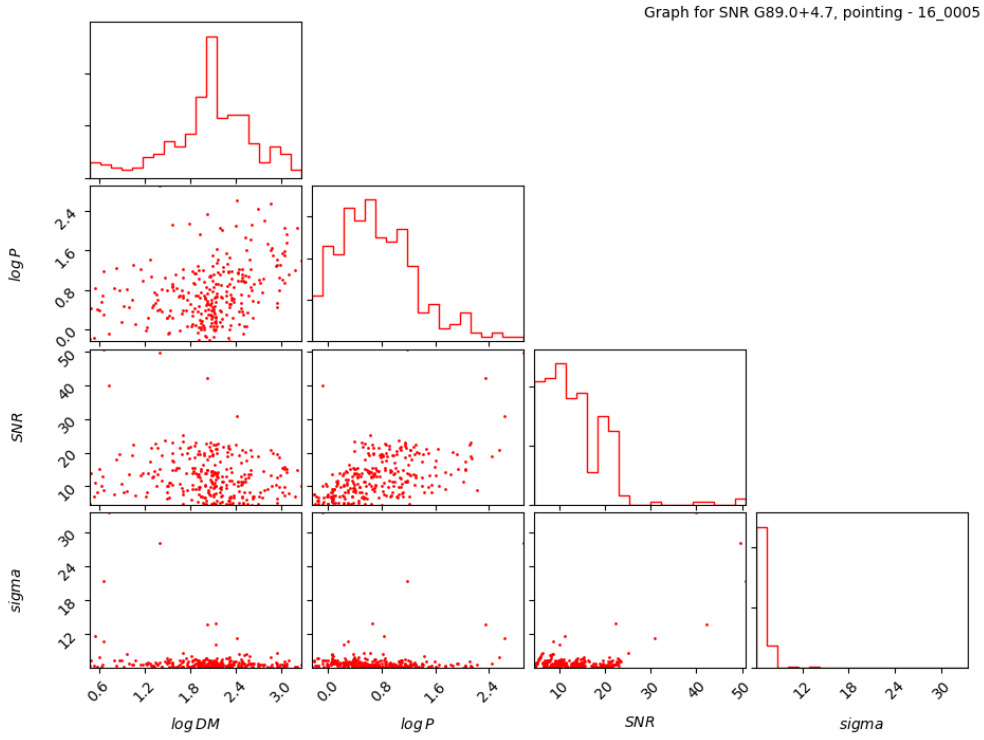

(b) Corner plot of G89.0+4.7, pointing 16_0005

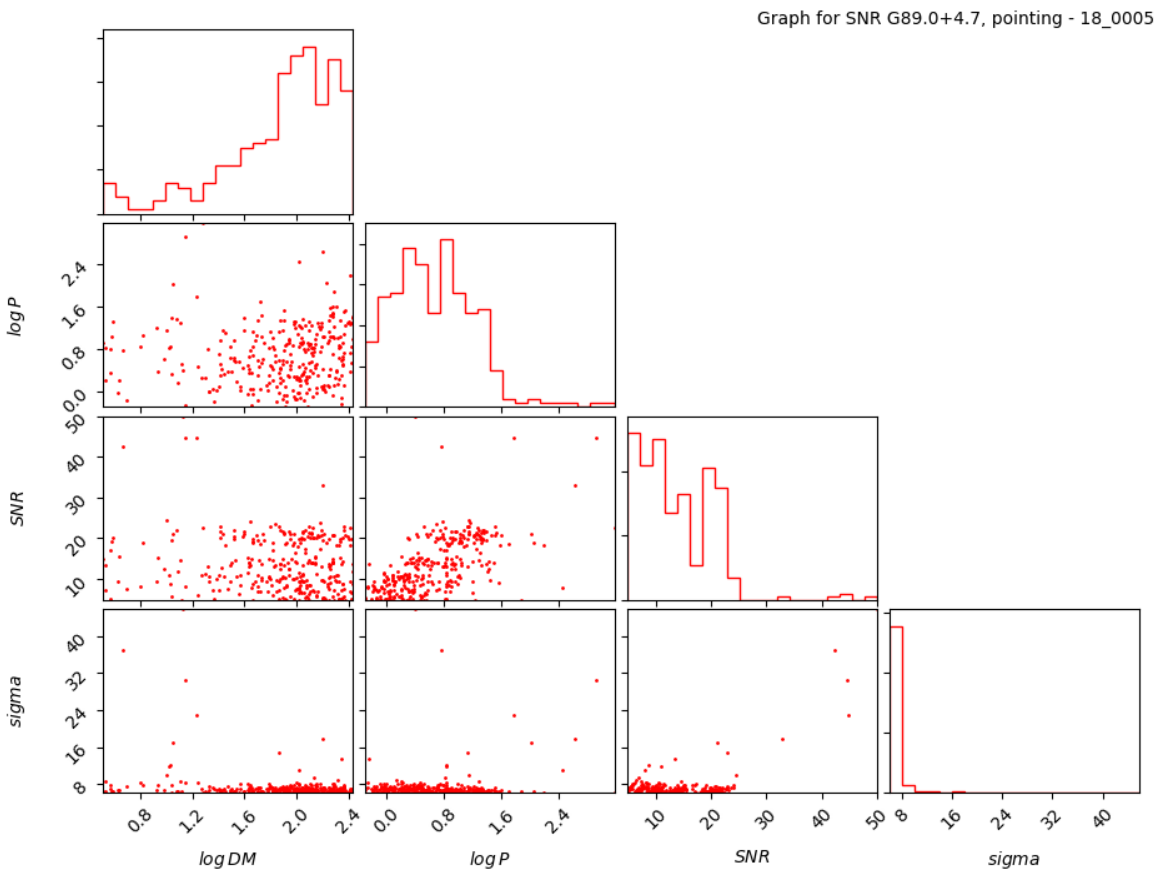

(a) Corner plot of G89.0+4.7, pointing 18_0005

B.4 116.9+0.2

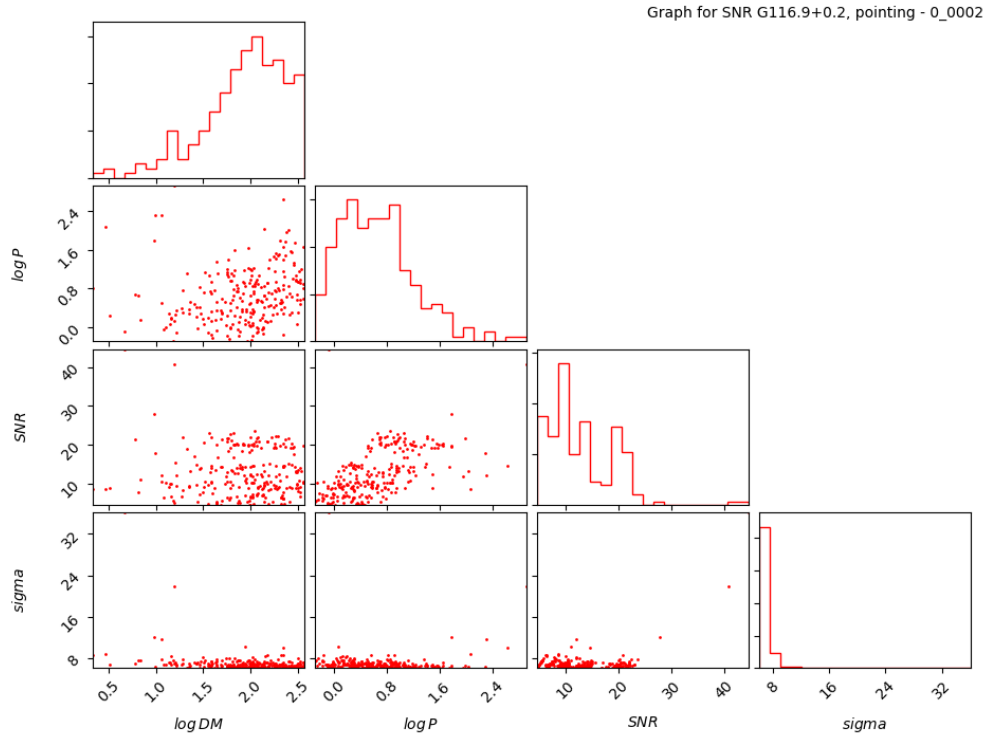

(a) Corner plot of G116.9+0.2, pointing 0_0002

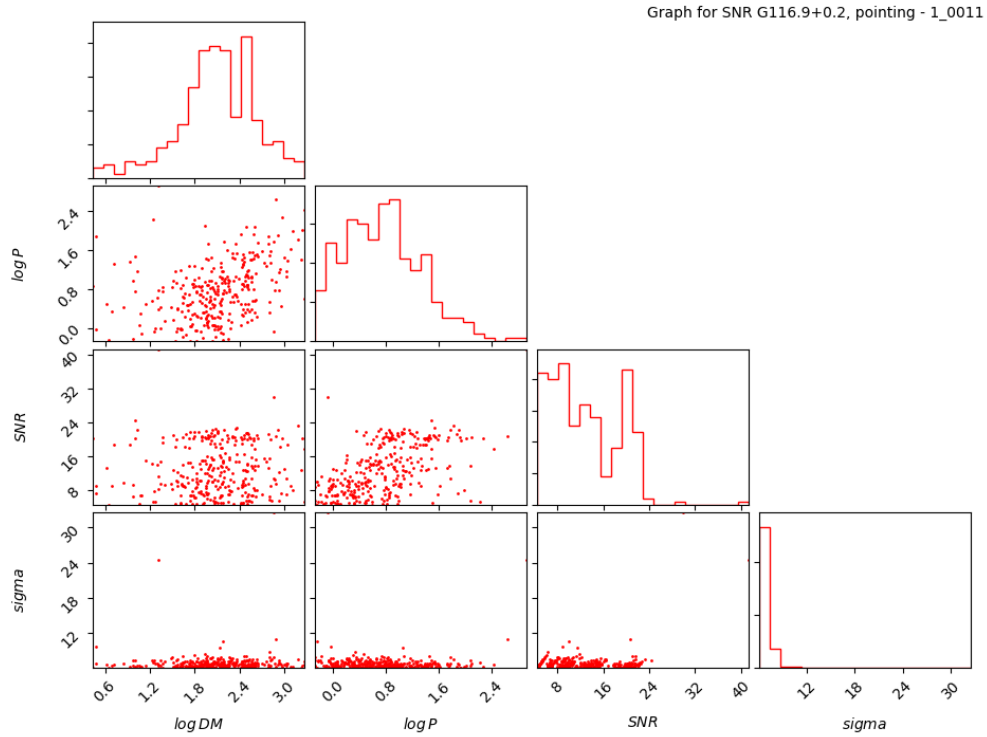

(b) Corner plot of G116.9+0.2, pointing 1_0011

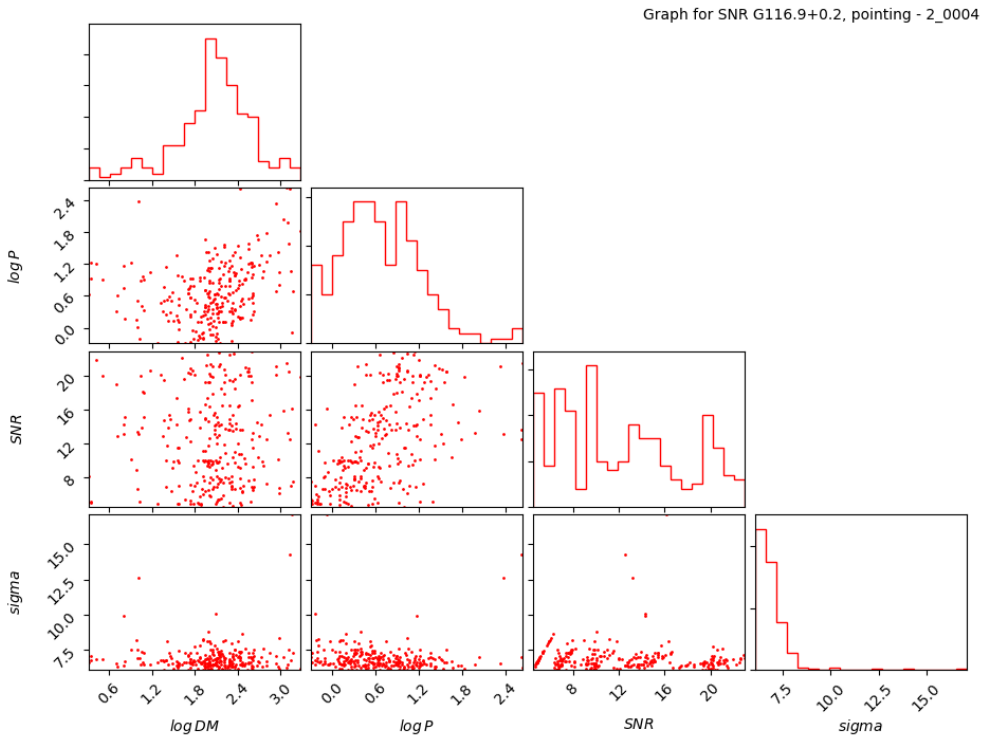

(a) Corner plot of G116.9+0.2, pointing 2_0004

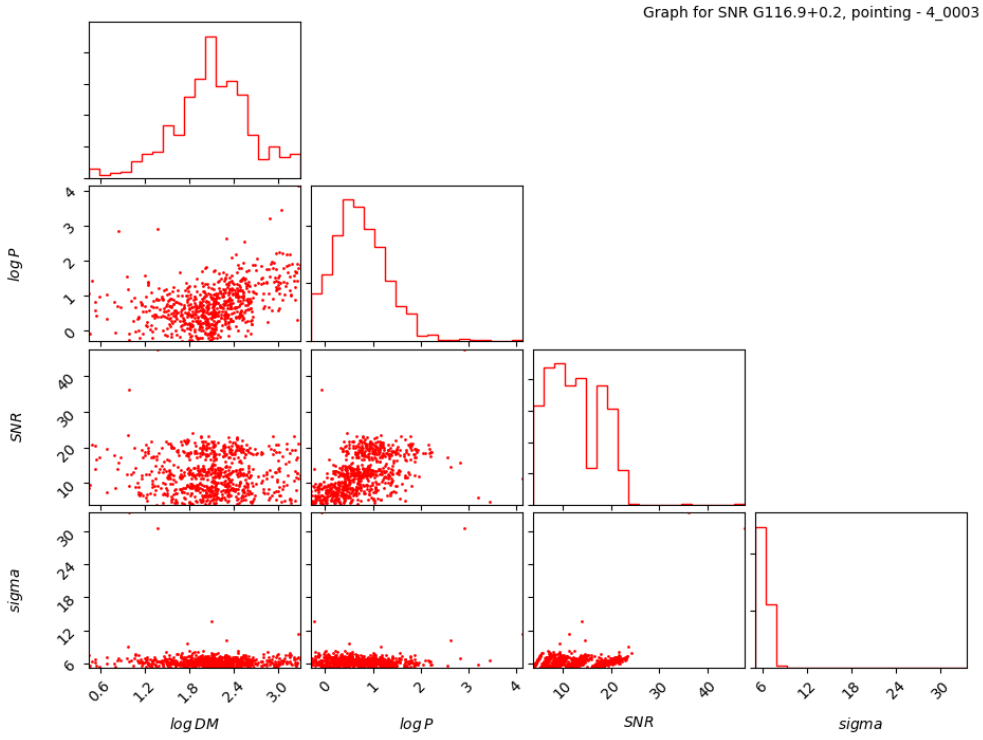

(b) Corner plot of G116.9+0.2, pointing 4_0003

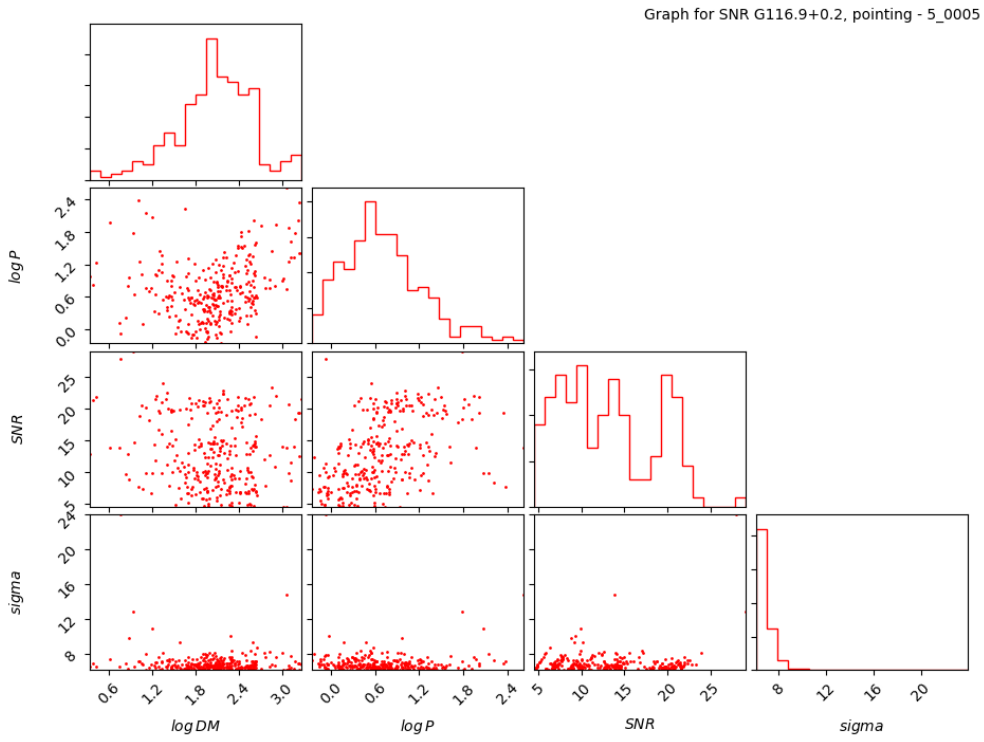

(a) Corner plot of G116.9+0.2, pointing 5_0005

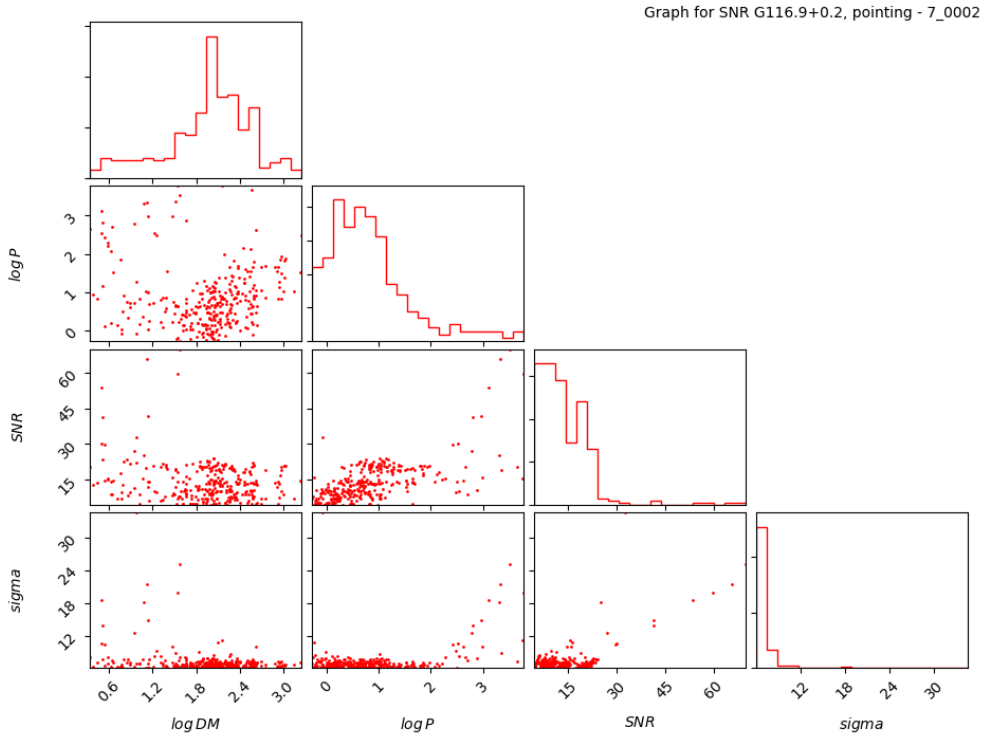

(b) Corner plot of G116.9+0.2, pointing 7_0002

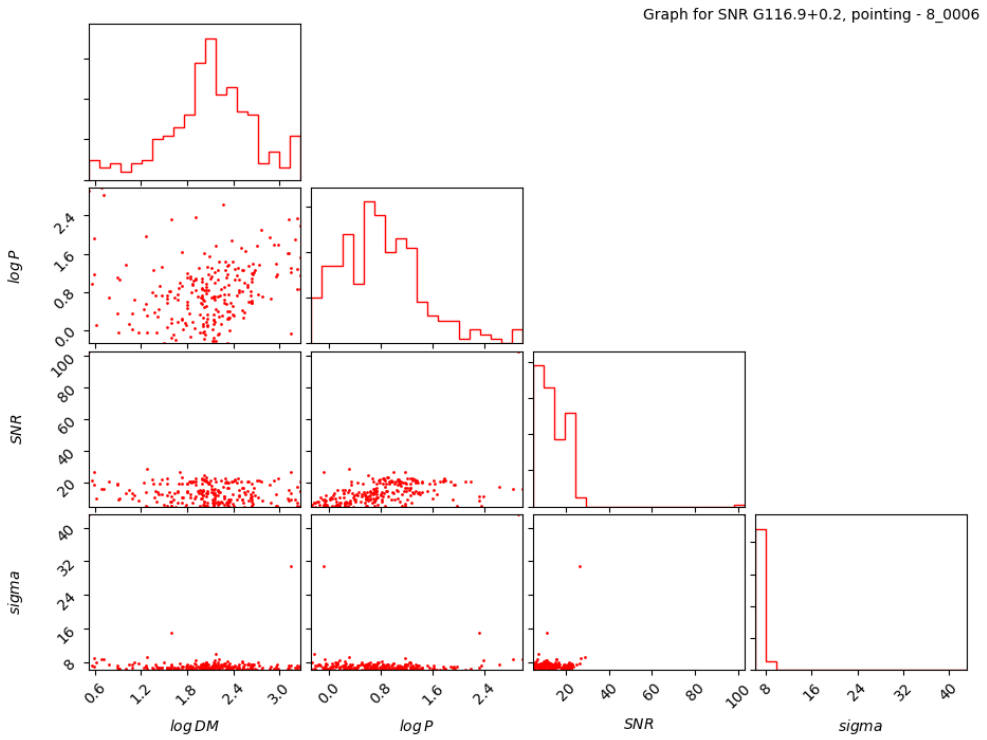

(a) Corner plot of G116.9+0.2, pointing 8_0006

B.5 156.2+5.7

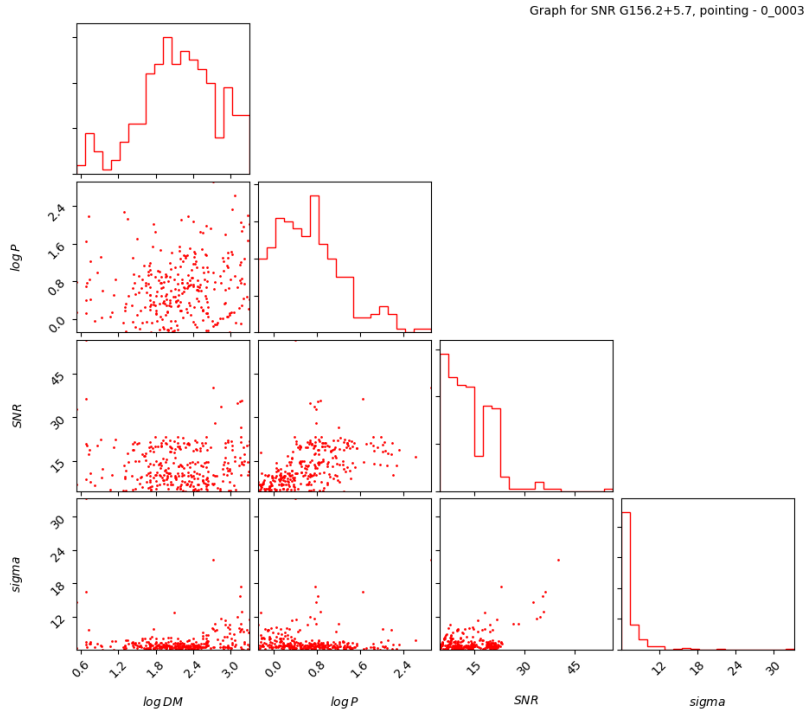

(a) Corner plot of G156.2+5.7, pointing 3_0003

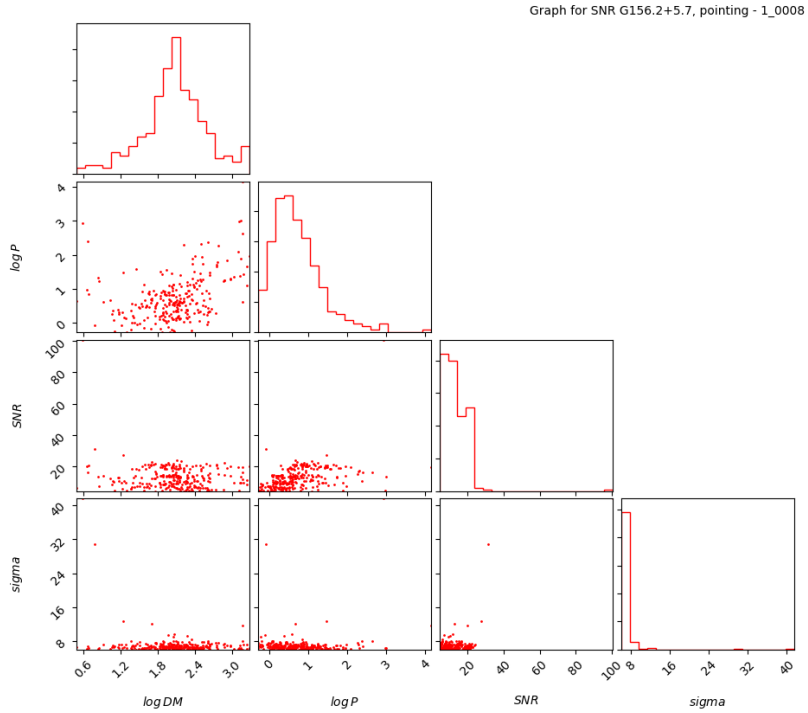

(b) Corner plot of G156.2+5.7, pointing 1_0008

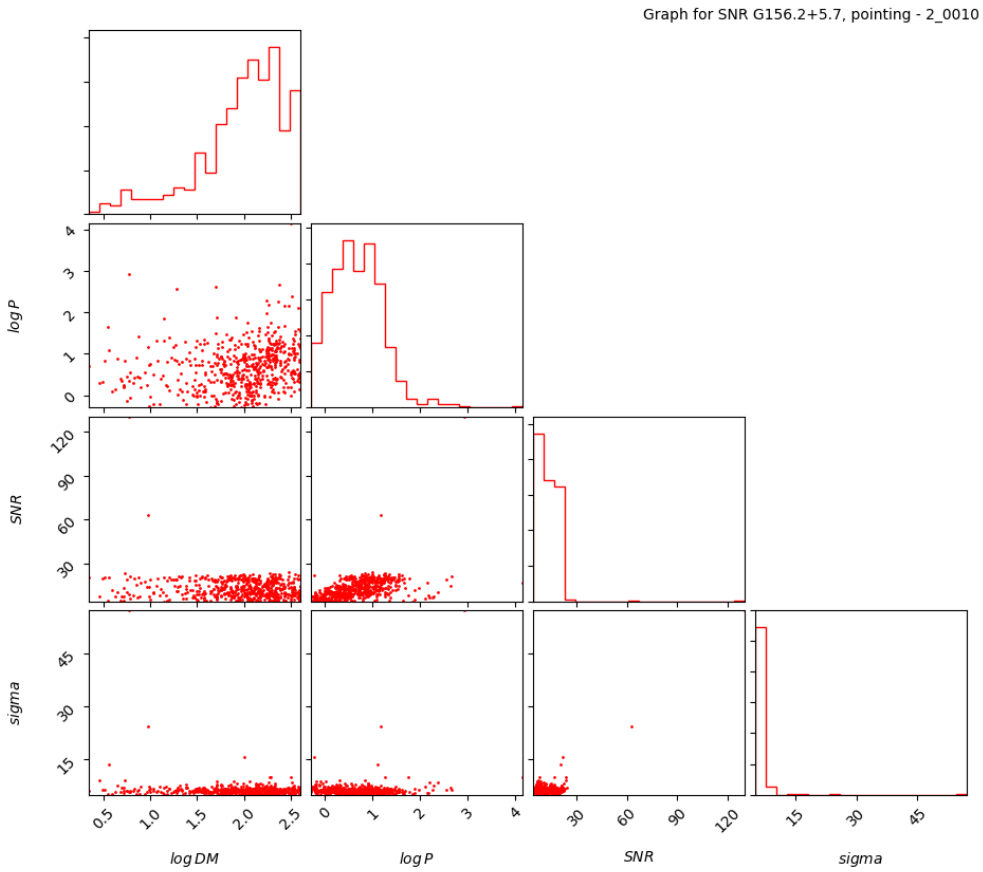

(a) Corner plot of G156.2+5.7, pointing 2_0010

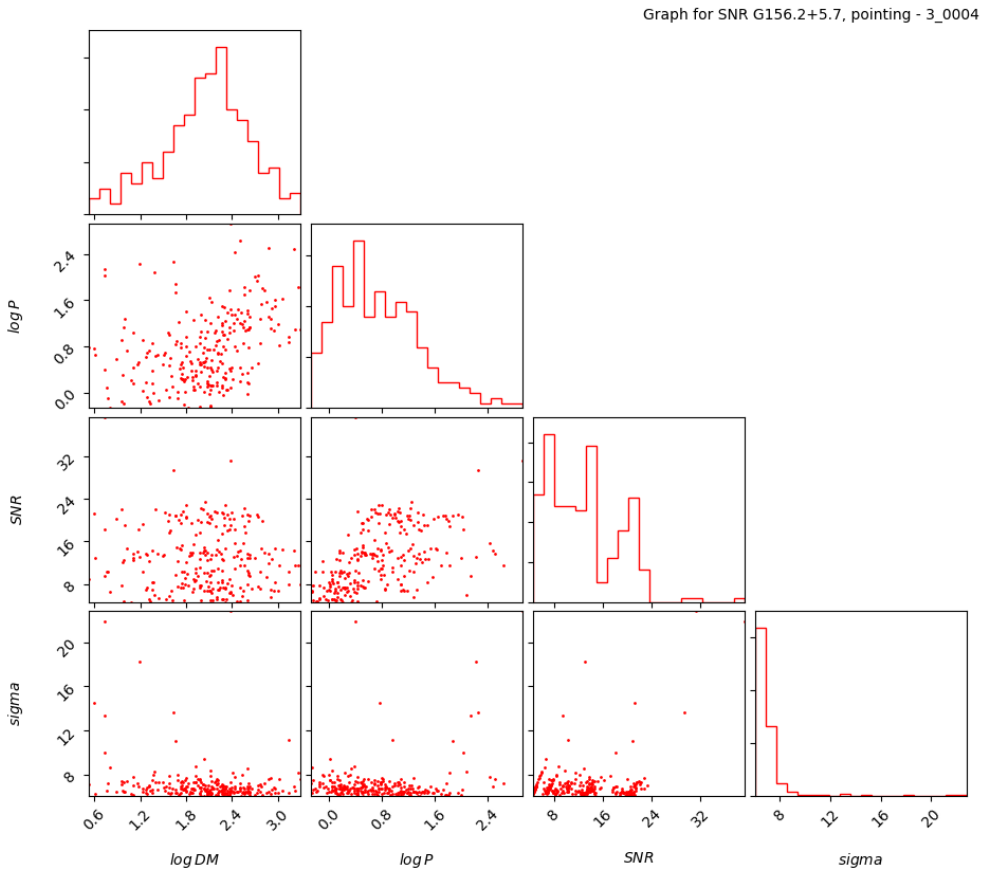

(b) Corner plot of G156.2+5.7, pointing 3_0004

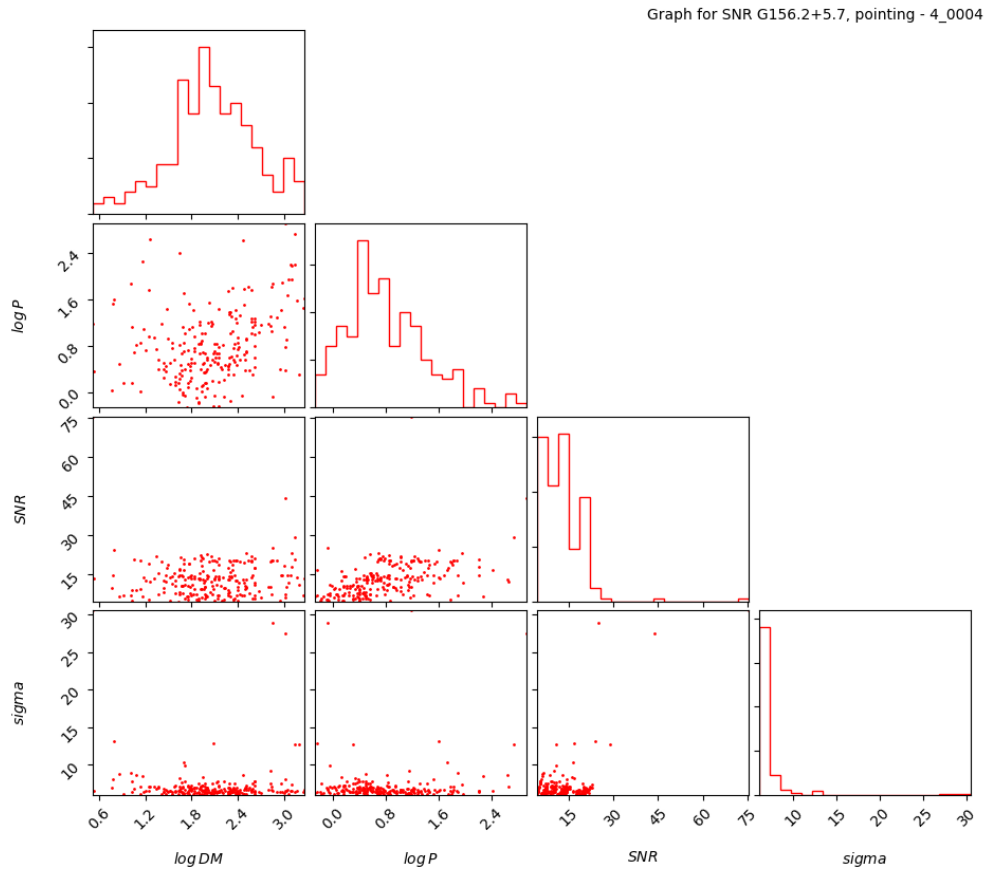

(a) Corner plot of G156.2+5.7, pointing 4_0004

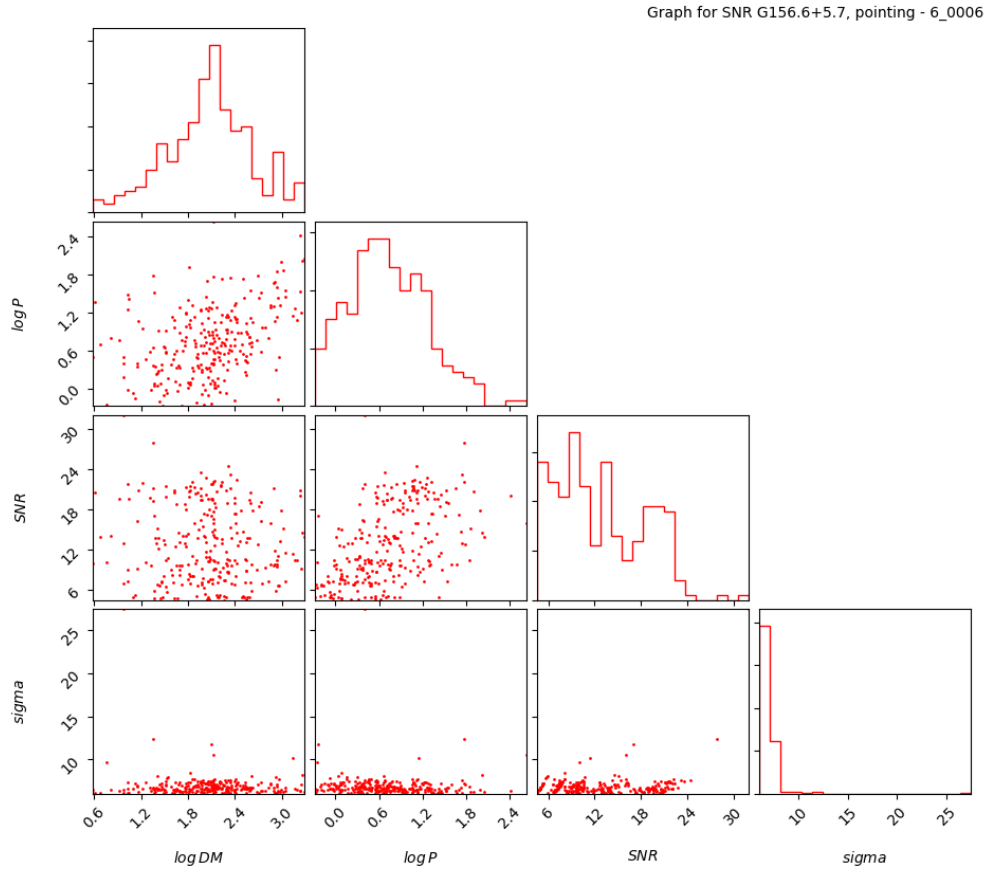

(b) Corner plot of G156.2+5.7, pointing 6_0006

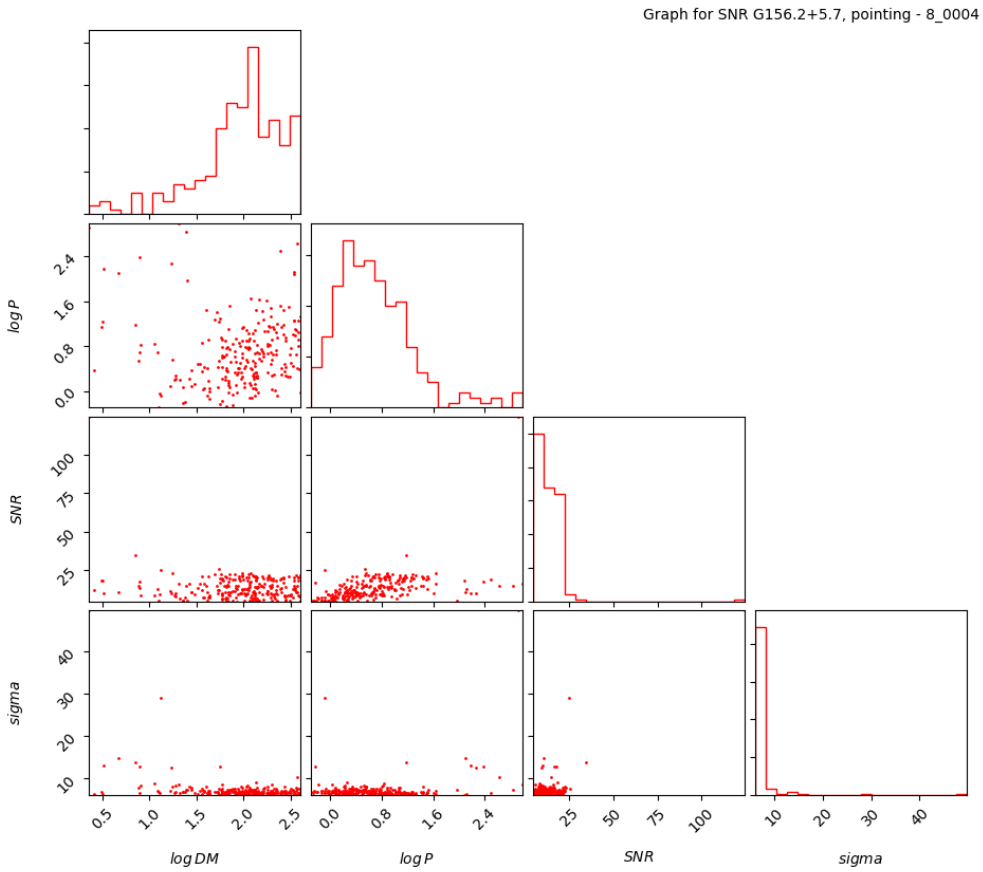

(a) Corner plot of G156.2+5.7, pointing 8_0004

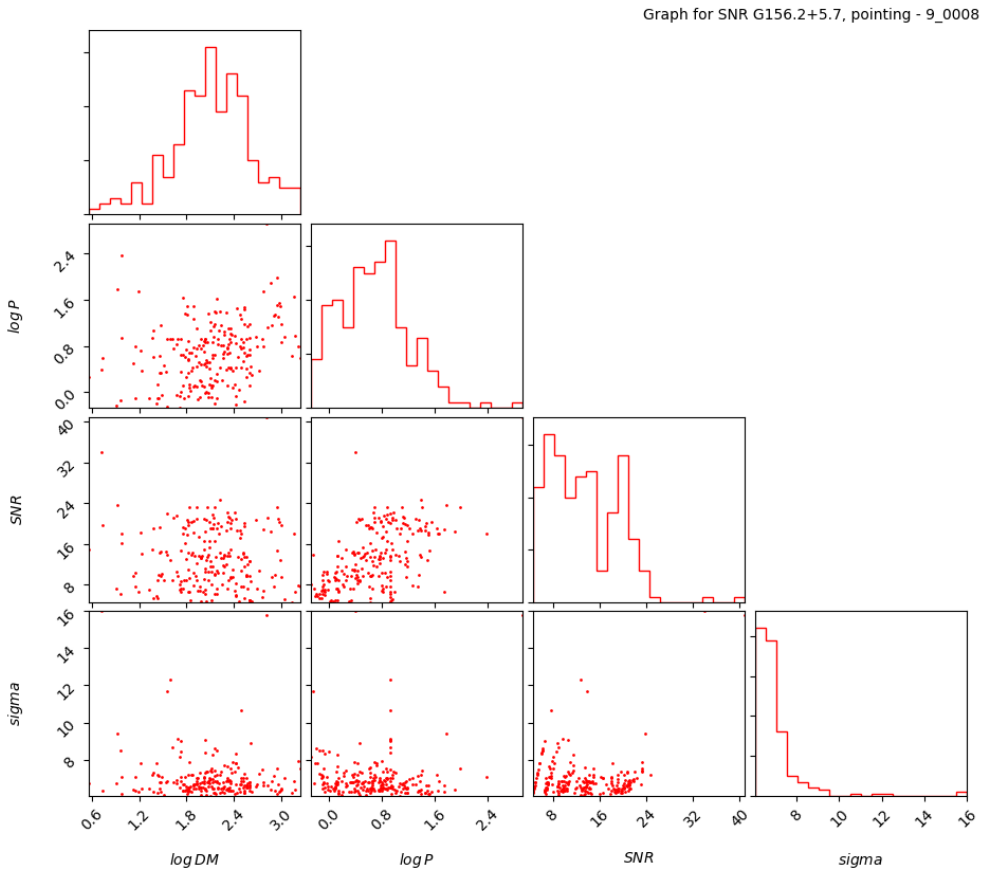

(b) Corner plot of G156.2+5.7, pointing 9_0008

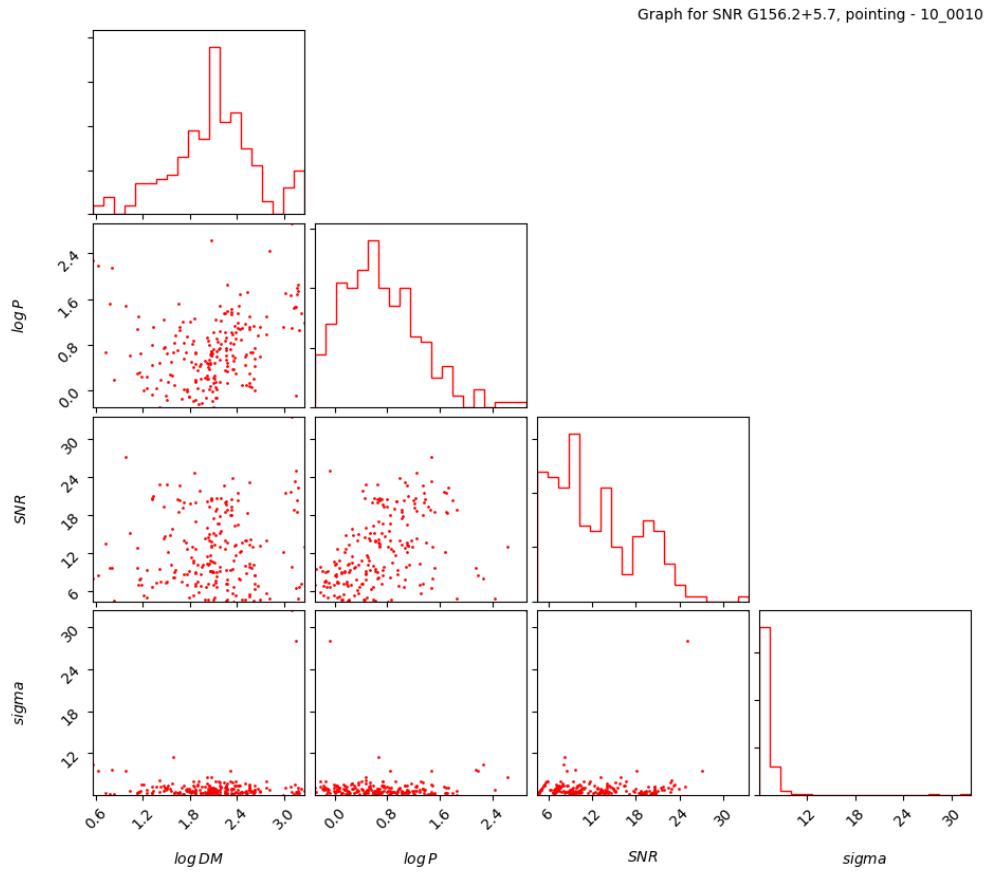

(a) Corner plot of G156.2+5.7, pointing 10_0010

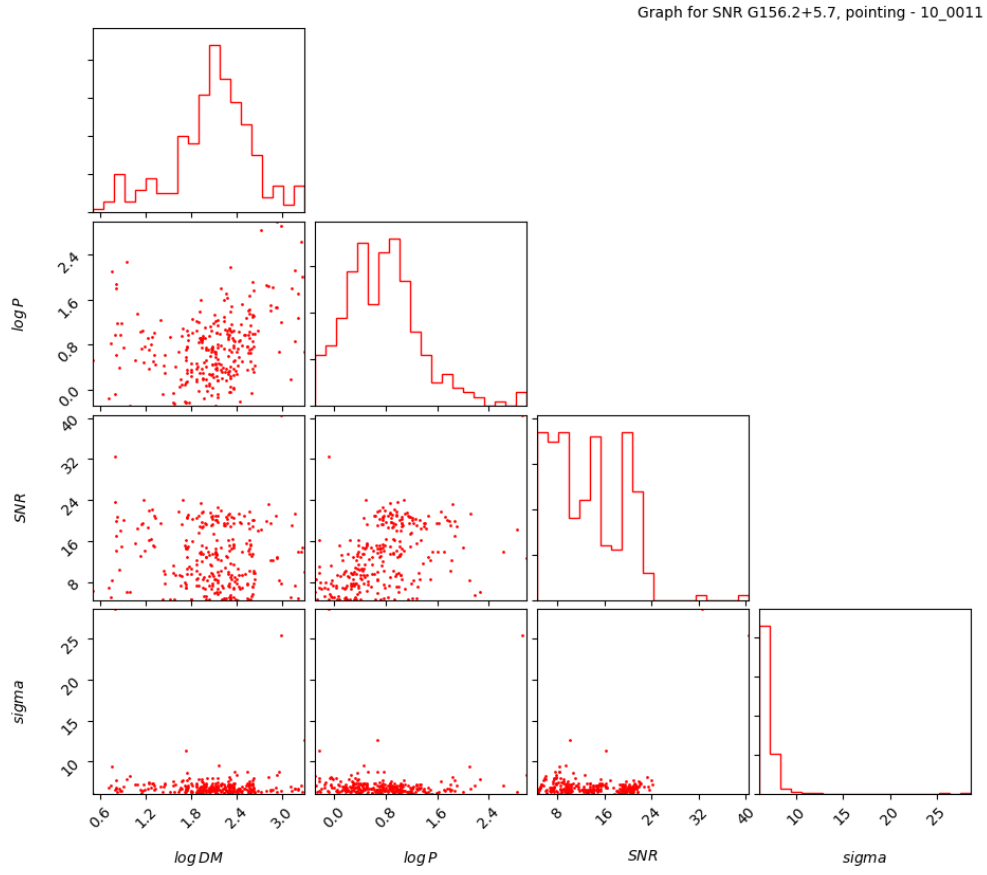

(b) Corner plot of G156.2+5.7, pointing 10_0011

Appendix C

Calculation of the velocity of the pulsar

The angular size, θ (in radian) of the remnant, the distance of the remnant from our line of sight, d(in pc) and the age, t (in yr) of the remnant is known. From θ and d we can calculate the distance of the remnant, r, by using :

$$r = \theta x d \tag{C.1}$$

The velocity of the pulsar, v is given as:

$$v = \frac{r}{t} \tag{C.2}$$

This gives the velocity a pulsar should attain in order to escape the supernova remnant.

For example, SNR G53.6-2.2, has angular size, θ as 0.00475 radian, distance from our line of sight, d as 2800 pc and age, t as 7×10^3. We get r as 26.6 pc. Putting the above values in equation C.2, we get 1859.03 km s^{-1}. Similarly, we can calculate the velocity of the puslar for the rest of the supernova remnant also.

Bibliography

(1950). The formation of a blast wave by a very intense explosion i. theoretical discussion. *Proceedings of the Royal Society of London A: Mathematical, Physical and Engineering Sciences*, 201(1065):159–174.

Abdo, A. A., Ackermann, M., Ajello, M., et al. (2009). Detection of 16 Gamma-Ray Pulsars Through Blind Frequency Searches Using the Fermi LAT. *Science*, 325:840.

Abolfathi, B., Aguado, D. S., Aguilar, G., Allende Prieto, C., Almeida, A., Ananna, T. T., Anders, F., Anderson, S. F., Andrews, B. H., Anguiano, B., and et al. (2018). The Fourteenth Data Release of the Sloan Digital Sky Survey: First Spectroscopic Data from the Extended Baryon Oscillation Spectroscopic Survey and from the Second Phase of the Apache Point Observatory Galactic Evolution Experiment. *The Astrophysical Journal Supplement Series*, 235:42.

Acero, F., Ackermann, M., Ajello, M., et al. (2016). The First Fermi LAT Supernova Remnant Catalog. *The Astrophysical Journal Supplement Series*, 224:8.

Ambrocio-Cruz, P., Rosado, M., and de La Fuente, E. (2006). The Composite Form of the Supernova Remnant 3C 400.2: Two Interacting Supernova Remnants or a Single Supernova Remnant with a Blow-Out? *Revista Mexicana de Astronomia y Astrofisica*, 42:241–249.

Arons, J. (1996). Pulsars as gamma ray sources. *Astronomy and Astrophysics, Supplement*, 120:49–60.

Baade, W. and Zwicky, F. (1934). On Super-novae. *Proceedings of the National Academy of Science*, 20:254–259.

Backer, D. C. and Chandran, B. D. G. (2000). Probing the Anisotropy of MHD Turbulence in the Local ISM with Diffractive Scintillation of Pulsars. In *American Astronomical Society Meeting Abstracts*, volume 197 of *Bulletin of the American Astronomical Society*, page 1402.

Backer, D. C., Kulkarni, S. R., Heiles, C., Davis, M. M., and Goss, W. M. (1982). A millisecond pulsar. *Nature*, 300:615–618.

Baring, M. G. (2001). Resonant Compton Upscattering in Magnetars. In *American Astronomical Society Meeting Abstracts*, volume 33 of *Bulletin of the American Astronomical Society*, page 1484.

Bates, S. D., Lorimer, D. R., and Verbiest, J. P. W. (2013). The pulsar spectral index distribution. *Monthly Notices of the Royal Astronomical Society*, 431:1352–1358.

Becker, W., Weisskopf, M. C., Arzoumanian, Z., Lorimer, D., Camilo, F., Elsner, R. F., Kanbach, G., Reimer, O., Swartz, D. A., Tennant, A. F., and O'Dell, S. L. (2004). A Multiwavelength Search for a Counterpart of the Brightest Unidentified Gamma-Ray Source 3EG J2020+4017 (2CG 078+2). *The Astrophysical Journal*, 615:897–907.

Bell Burnell, S. J. (2004). So few pulsars, so few females. *Science*, 304(5670):489–489.

Benvenuto, O. G., Clocchiatti, A., and Méndez, M. (1987). Expansion model for the external envelopes of the SN 1987A. *Boletin de la Asociacion Argentina de Astronomia La Plata Argentina*, 33:385.

Bhat, N. D. R., Tremblay, S. E., Kirsten, F., Meyers, B. W., Sokolowski, M., van Straten, W., McSweeney, S. J., Ord, S. M., Shannon, R. M., Beardsley, A., Crosse, B., Emrich, D., Franzen, T. M. O., Horsley, L., Johnston-Hollitt, M., Kaplan, D. L., Kenney, D., Morales, M. F., Pallot, D., Steele, K., Tingay, S. J., Trott, C. M., Walker, M., Wayth, R. B., Williams,

A., and Wu, C. (2018). Observations of Low-frequency Radio Emission from Millisecond Pulsars and Multipath Propagation in the Interstellar Medium. *The Astrophysical Journal Supplement Series*, 238:1.

Biggs, J. D. and Lyne, A. G. (1996). A Search for Radio Pulsars in Globular Clusters, Supernova Remnants and Transient X-Ray Sources. *Monthly Notices of the Royal Astronomical Society*, 282:691–698.

Blandford, R. D. and Romani, R. W. (1988). On the interpretation of pulsar braking indices. *Monthly Notices of the Royal Astronomical Society*, 234:57P–60P.

Bonanno, A., Urpin, V., and Belvedere, G. (2005). Protoneutron star dynamos and pulsar magnetism. *Astronomy and Astrophysics*, 440:199–205.

Breen, A. and McCarthy, D. (1995). A Re-evaluation of the Eastern and Western Records of the Supernova of 1054. *Vistas in Astronomy*, 39:363–379.

Broersen, S. and Vink, J. (2015). A Chandra X-ray study of the mixed-morphology supernova remnant 3C 400.2. *Monthly Notices of the Royal Astronomical Society*, 446:3885–3894.

Bykov, A. M., Chevalier, R. A., Ellison, D. C., and Uvarov, Y. A. (2000). Nonthermal Emission from a Supernova Remnant in a Molecular Cloud. *The Astrophysical Journal*, 538:203–216.

Byun, D.-Y., Koo, B.-C., Tatematsu, K., and Sunada, K. (2006). Interaction between the Supernova Remnant HB 21 and Molecular Clouds. *The Astrophysical Journal*, 637:283–295.

Caswell, J. L. and Lerche, I. (1979). Galactic supernova remnants - Dependence of radio brightness on galactic height and its implications. *Monthly Notices of the Royal Astronomical Society*, 187:201–216.

Chen, K. and Ruderman, M. (1993). Pulsar death lines and death valley. *The Astrophysical Journal*, 402:264–270.

Chevalier, R. A. (1982). Are young supernova remnants interacting with circumstellar gas. *Astrophysical Journal, Letters*, 259:L85–L89.

Clark, C. J., Wu, J., Pletsch, H. J., Guillemot, L., Allen, B., Aulbert, C., Beer, C., Bock, O., Cuéllar, A., Eggenstein, H. B., Fehrmann, H., Kramer, M., Machenschalk, B., and Nieder, L. (2017). The Einstein@Home Gamma-ray Pulsar Survey. I. Search Methods, Sensitivity, and Discovery of New Young Gamma-Ray Pulsars. *The Astrophysical Journal*, 834:106.

Clark, D. H. and Caswell, J. L. (1976). A study of galactic supernova remnants, based on Molonglo-Parkes observational data. *Monthly Notices of the Royal Astronomical Society*, 174:267–305.

Condon, J. J., Cotton, W. D., Greisen, E. W., Yin, Q. F., Perley, R. A., Taylor, G. B., and Broderick, J. J. (1998). The nrao vla sky survey. *The Astronomical Journal*, 115(5):1693.

Cordes, J., Lazio, T., Chatterjee, S., Arzoumanian, Z., and Chernoff, D. (2002). A new pulsar distance model and some implications for pulsar velocities, populations and searches. In *34th COSPAR Scientific Assembly*, volume 34 of *COSPAR Meeting*, page 2305.

Cordes, J. M. and Lazio, T. J. W. (2002). NE2001.I. A New Model for the Galactic Distribution of Free Electrons and its Fluctuations. *ArXiv Astrophysics e-prints*.

Demorest, P. B., Pennucci, T., Ransom, S. M., Roberts, M. S. E., and Hessels, J. W. T. (2010). A two-solar-mass neutron star measured using Shapiro delay. *Nature*, 467:1081–1083.

Dimoudi, S. and Armour, W. (2015). Pulsar Acceleration Searches on the GPU for the Square Kilometre Array. *ArXiv e-prints*.

Dubner, G. and Giacani, E. (2015). Radio emission from supernova remnants. *Astronomy and Astrophysics Reviews*, 23:3.

Dubner, G. M., Giacani, E. B., Goss, W. M., and Winkler, P. F. (1994). VLA observations of the supernova remnant 3C400-2 at 327 MHz and 1465 MHz. *Astronomical Journal*, 108:207–213.

Dyer, K. K. and Reynolds, S. P. (1999). Multifrequency studies of bright radio supernova remnants. iii. x-ray and radio observations of 3c 397. *The Astrophysical Journal*, 526(1):365.

Eatough, R. P., Kramer, M., Lyne, A. G., et al. (2013). A coherent acceleration search of the Parkes multibeam pulsar survey - techniques and the discovery and timing of 16 pulsars. *Monthly Notices of the Royal Astronomical Society*, 431:292–307.

Erkes, J. W. and Dickel, J. R. (1969). Radio Observations of the Supernova Remnant HB 21. *Astronomical Journal*, 74:840–845.

Frail, D. A. and Moffett, D. A. (1993). Deep VLA imaging of pulsar-powered nebulae and the beaming fraction of young pulsars. *The Astrophysical Journal*, 408:637–645.

Gaensler, B. M. (2001). Plerions and pulsar-powered nebulae. In Holt, S. S. and Hwang, U., editors, *Young Supernova Remnants*, volume 565 of *American Institute of Physics Conference Series*, pages 295–304.

Gaisser, T. K., Protheroe, R. J., and Stanev, T. (1998). Gamma-Ray Production in Supernova Remnants. *The Astrophysical Journal*, 492:219–227.

Ghosh, P. and White, N. E. (1999). Low-mass X-ray Binaries, Millisecond Radio Pulsars and the Cosmic Star-formation Rate. In *AAS/High Energy Astrophysics Division #4*, volume 31 of *Bulletin of the American Astronomical Society*, page 741.

Giacani, E. B., Dubner, G., Cappa, C., and Testori, J. (1998). The structure of atomic gas around the supernova remnant 3C 400.2. *Astronomy and Astrophysics, Supplement*, 133:61–70.

Gorham, P. W., Ray, P. S., Anderson, S. B., Kulkarni, S. R., and Prince, T. A. (1996). A Pulsar Survey of 18 Supernova Remnants. *The Astrophysical Journal*, 458:257.

Goss, W. M., Siddesh, S. G., and Schwarz, U. J. (1975). A high resolution map of the supernova remnant 3C 400.2 at 610 MHz. *Astronomy and Astrophysics*, 43:459–463.

Green, D. A. (2014). A catalogue of 294 Galactic supernova remnants. *Bulletin of the Astronomical Society of India*, 42:47–58.

Gupta, Y. (2002). Pulsars and the ISM. In Pramesh Rao, A., Swarup, G., and Gopal-Krishna, editors, *The Universe at Low Radio Frequencies*, volume 199 of *IAU Symposium*, page 363.

Hailey, C. J. and Craig, W. W. (1995). Discovery of a Candidate Isolated Neutron Star in a New Supernova Remnant near CTB 1. *Astrophysical Journal, Letters*, 455:L151.

Hanbury Brown, R. and Hazard, C. (1953). An Extended Radio-frequency Source of Extra-galactic Origin. *Nature*, 172:997–998.

Haslam, C. G. T., Salter, C. J., Stoffel, H., and Wilson, W. E. (1982). A 408 MHz all-sky continuum survey. II - The atlas of contour maps. *Astronomy and Astrophysics, Supplement*, 47:1.

Hewish, A., Bell, S. J., Pilkington, et al. (1968). Observation of a Rapidly Pulsating Radio Source. *Nature*, 217:709–713.

Higgs, L. A., Landecker, T. L., and Roger, R. S. (1977). The true extent of the Gamma Cygni supernova remnant. *Astronomical Journal*, 82:718–724.

Holden, D. J. and Caswell, J. L. (1969). 178 mhz observations of galactic radio sources. *Monthly Notices of the Royal Astronomical Society*, 143(4):407–435.

Hui, C. Y., Seo, K. A., Lin, L. C. C., Huang, R. H. H., Hu, C. P., Wu, J. H. K., Trepl, L., Takata, J., Wang, Y., Chou, Y., Cheng, K. S., and Kong, A. K. H. (2015). A Detailed X-Ray Investigation of PSR J2021+4026 and the γ-Cygni Supernova Remnant. *The Astrophysical Journal*, 799:76.

Ilovaisky, S. A. and Lequeux, J. (1972). A Study of Galactic Supernova Remnants. I. Distances, Radio Luminosity Function and Galactic Distribution. *Astronomy and Astrophysics*, 18:169–185.

Jackson, J. D. (1962). *Classical Electrodynamics*.

Jaffe, A. H. and Backer, D. (2003a). Gravitational Radiation from Massive Black Hole Binaries. In *IAU Joint Discussion*, volume 1 of *IAU Joint Discussion*.

Jaffe, A. H. and Backer, D. C. (2003b). Gravitational Waves Probe the Coalescence Rate of Massive Black Hole Binaries. *The Astrophysical Journal*, 583:616–631.

Janssen, G. H., Stappers, B. W., Braun, R., van Straten, W., Edwards, R. T., Rubio-Herrera, E., van Leeuwen, J., and Weltevrede, P. (2009). Discovery and timing of the first 8gr8 Cygnus survey pulsars. *Astronomy and Astrophysics*, 498:223–231.

Johnston, S. and Karastergiou, A. (2017). Pulsar braking and the P-dot{P} diagram. *Monthly Notices of the Royal Astronomical Society*, 467:3493–3499.

Kaspi, V. M. and Beloborodov, A. M. (2017). Magnetars. *Annual review of Astron and Astrophysics*, 55:261–301.

Kaspi, V. M., Manchester, R. N., Johnston, S., Lyne, A. G., and D'Amico, N. (1996). A Search for Radio Pulsars in Southern Supernova Remnants. *Astronomical Journal*, 111:2028.

Kavanagh, P. J., Sasaki, M., Points, S. D., Filipovi´c, M. D., Maggi, P., Bozzetto, L. M., Crawford, E. J., Haberl, F., and Pietsch, W. (2013). Multiwavelength study of the newly confirmed supernova remnant mcsnr j0527-7104 in the large magellanic cloud. *A&A*, 549:A99.

Keane, E. F. and McLaughlin, M. A. (2011). Rotating radio transients. *Bulletin of the Astronomical Society of India*, 39:333–352.

Koo, B.-C., Rho, J., Reach, W. T., Jung, J., and Mangum, J. G. (2001). Shocked Molecular Gas in the Supernova Remnant HB 21. *The Astrophysical Journal*, 552:175–188.

Kramer, M., Stairs, I. H., Manchester, R. N., McLaughlin, M. A., Lyne, A. G., Ferdman, R. D., Burgay, M., Lorimer, D. R., Possenti, A., D'Amico, N., Sarkissian, J. M., Hobbs, G. B., Reynolds, J. E., Freire, P. C. C., and Camilo, F. (2006). Tests of General Relativity from Timing the Double Pulsar. *Science*, 314:97–102.

Kundu, M. R., Becker, R. H., and Velusarny, T. (1973). Polarization of the supernova remnant HB21 at 11-cm wavelength. *Astronomical Journal*, 78:170–173.

Lai, D. (2004). Neutron star kicks and supernova asymmetry. In Höflich, P., Kumar, P., and Wheeler, J. C., editors, *Cosmic explosions in three dimensions*, page 276.

Landecker, T. L., Roger, R. S., and Higgs, L. A. (1980). Atomic hydrogen in a field in Cygnus X containing the supernova remnant G78.2+2.1. *Astronomy and Astrophysics, Supplement*, 39:133–151.

Lazarus, P. (2015). *Pulsar discoveries and their exploitation*. PhD thesis, Bonn University.

Lazendic, J. S. and Slane, P. O. (2006). Enhanced Abundances in Three Large-Diameter Mixed-Morphology Supernova Remnants. *The Astrophysical Journal*, 647:350–366.

Leahy, D. A. (1987). Einstein X-ray observations of the supernova remnant HB21. *Monthly Notices of the Royal Astronomical Society*, 228:907–913.

Leahy, D. A. and Aschenbach, B. (1996). ROSAT X-ray observations of the supernova remnant HB 21. *Astronomy and Astrophysics*, 315:260–264.

Leahy, D. A., Green, K., and Ranasinghe, S. (2013). X-ray and radio observations of the γ Cygni supernova remnant G78.2+2.1. *Monthly Notices of the Royal Astronomical Society*, 436:968–977.

Liang, Z.-X., Liang, Y., and Weisberg, J. M. (2014). Testing the rotating lighthouse model with the double pulsar system PSR J0737-3039A/B. *Monthly Notices of the Royal Astronomical Society*, 439:3712–3718.

Lin, L. C. C., Hui, C. Y., Hu, C. P., Wu, J. H. K., Huang, R. H. H., Trepl, L., Takata, J., Seo, K. A., Wang, Y., Chou, Y., and Cheng, K. S. (2013). Discovery of X-Ray Pulsation from the Geminga-like Pulsar PSR J2021+4026. *Astrophysical Journal, Letters*, 770:L9.

Lopez, L. A., Ramirez-Ruiz, E., Badenes, C., Huppenkothen, D., Jeltema, T. E., and Pooley, D. A. (2009). Typing supernova remnants using x-ray line emission morphologies. *The Astrophysical Journal Letters*, 706(1):L106.

Lorimer, D. R. and Kramer, M. (2004). *Handbook of Pulsar Astronomy*.

Lorimer, D. R., Lyne, A. G., and Camilo, F. (1998). A search for pulsars in supernova remnants. *Astronomy and Astrophysics*, 331:1002–1010.

Lozinskaya, T. A., Pravdikova, V. V., and Finoguenov, A. V. (2000). The Supernova Remnant G78.2+2.1: New Optical and X-ray Observations. *Astronomy Letters*, 26:77–87.

Manchester, R. N. (2007). Searching for a Pulsar in SN1987A. In Immler, S., Weiler, K., and McCray, R., editors, *Supernova 1987A: 20 Years After: Supernovae and Gamma-Ray Bursters*, volume 937 of *American Institute of Physics Conference Series*, pages 134–143.

Maron, O., Kijak, J., Kramer, M., et al. (2000). Pulsar spectra analysis. In Kramer, M., Wex, N., and Wielebinski, R., editors, *IAU Colloq. 177: Pulsar Astronomy - 2000 and Beyond*, volume 202 of *Astronomical Society of the Pacific Conference Series*, page 227.

McLaughlin, M. (2006). Where are the RRATs in the Neutron Star Zoo? XMM-Newton Proposal.

Milne, D. K. (1970). Supernova Remnants, Pulsars and X-Ray Sources. *Proceedings of the Astronomical Society of Australia*, 1:333–334.

Ng, C., Champion, D. J., Bailes, M., et al. (2015). The High Time Resolution Universe Pulsar Survey - XII. Galactic plane acceleration search and the discovery of 60 pulsars. *Monthly Notices of the Royal Astronomical Society*, 450:2922–2947.

Pacini, F. (1968). Rotating Neutron Stars, Pulsars and Supernova Remnants. *Nature*, 219:145–146.

Pfeffermann, E., Aschenbach, B., and Predehl, P. (1991). Discovery of a galactic supernova remnant with ROSAT. *Astronomy and Astrophysics*, 246:L28–L31.

Porayko, N. K., Noutsos, A., Tiburzi, C., Verbiest, J. P. W., Horneffer, A., Künsemöller, J., Osłowski, S., Kramer, M., Schnitzeler, D. H. F. M., Anderson, J. M., Brüggen, M.,

Grießmeier, J.-M., Hoeft, M., Schwarz, D. J., Serylak, M., and Wucknitz, O. (2019). Testing the accuracy of the ionospheric Faraday rotation corrections through LOFAR observations of bright northern pulsars. *Monthly Notices of the Royal Astronomical Society*, 483:4100–4113.

Press, B. (1998). "Fast" Statistical Methods for Interpolation and Model Fitting in One-Dimensional Data. In *Astrophysics and Algorithms*.

Ransom, S. M. (2001). *New search techniques for binary pulsars*. PhD thesis, Harvard University.

Ransom, S. M., Eikenberry, S. S., and Middleditch, J. (2002). Fourier Techniques for Very Long Astrophysical Time-Series Analysis. *Astronomical Journal*, 124:1788–1809.

Reich, W., Fuerst, E., and Arnal, E. M. (1992). Radio observations of the bright X-ray supernova remnant G156.2+5.7. *Astronomy and Astrophysics*, 256:214–224.

Rengelink, R. B., Tang, Y., de Bruyn, A. G., Miley, G. K., Bremer, M. N., Roettgering, H. J. A., and Bremer, M. A. R. (1997). The Westerbork Northern Sky Survey (WENSS), I. A 570 square degree Mini-Survey around the North Ecliptic Pole. *Astronomy and Astrophysics, Supplement*, 124:259–280.

Rho, J. and Petre, R. (1998). Mixed-morphology supernova remnants. *The Astrophysical Journal Letters*, 503(2):L167.

Rosado, M. (1983). The Optical Emission of the Supernova Remnant 3C400.2. *Revista Mexicana de Astronomia y Astrofisica*, 8:59.

Saken, J. M., Long, K. S., Blair, W. P., and Winkler, P. F. (1995). ROSAT observations of the supernova remnant 3C 400.2. *The Astrophysical Journal*, 443:231–237.

Schneiter, E. M., De La Fuente, E., and Velázquez, P. F. (2006). Simulated x-ray emission from a single-explosion model for a supernova remnant 3c 400.2. *Monthly Notices of the Royal Astronomical Society*, 371(1):369–374.

SEDOV, L. (1959). Chapter v - application to astrophysical problems. In SEDOV, L., editor, *Similarity and Dimensional Methods in Mechanics*, pages 305 – 353. Academic Press.

Seward, F. (2009). Chandra Supernova Remnant Catalog Update. Chandra Proposal.

Shapiro, S. L., Teukolsky, S. A., and Lightman, A. P. (1983). Black Holes, White Dwarfs, and Neutron Stars: The Physics of Compact Objects. *Physics Today*, 36:89.

Shklovskii, I. S. (1960). The Nature of Supernovae. *Soviet Astronomy*, 4:355.

Shporer, A., Kaplan, D. L., Steinfadt, J. D. R., Bildsten, L., Howell, S. B., and Mazeh, T. (2010). A ground-based measurement of the relativistic beaming effect in a detached double white dwarf binary. *The Astrophysical Journal Letters*, 725(2):L200.

Staveley-Smith, L., Potter, T. M., Zanardo, G., Gaensler, B. M., and Ng, C.-Y. (2014). Radio Observations of Supernova 1987A. In Ray, A. and McCray, R. A., editors, *Supernova Environmental Impacts*, volume 296 of *IAU Symposium*, pages 15–22.

Sturner, S. J., Skibo, J. G., Dermer, C. D., and Mattox, J. R. (1997). Temporal Evolution of Nonthermal Spectra from Supernova Remnants. *The Astrophysical Journal*, 490:619–632.

Swanenburg, B. N. (1981). Gamma ray astronomy with COS-B. *Annals of the New York Academy of Sciences*, 375:381–390.

Tatematsu, K., Fukui, Y., Landecker, T. L., and Roger, R. S. (1990). The interaction of the supernova remnant HB 21 with the interstellar medium - CO, H I, and radio continuum observations. *Astronomy and Astrophysics*, 237:189–200.

Taylor, J. H. and Weisberg, J. M. (1982). A new test of general relativity - Gravitational radiation and the binary pulsar PSR 1913+16. *The Astrophysical Journal*, 253:908–920.

Temim, T., Slane, P., Kolb, C., Blondin, J., Hughes, J. P., and Bucciantini, N. (2015). Late-Time Evolution of Composite Supernova Remnants: Deep Chandra Observations and Hydrodynamical Modeling of a Crushed Pulsar Wind Nebula in SNR G327.1-1.1. *The Astrophysical Journal*, 808:100.

Tian, W. W. and Leahy, D. A. (2008). The distances of supernova remnants Kes 69 and G21.5-0.9 from HI and ^{13}CO spectra. *Monthly Notices of the Royal Astronomical Society*, 391:L54–L58.

Trepl, L., Hui, C. Y., Cheng, K. S., Takata, J., Wang, Y., Liu, Z. Y., and Wang, N. (2010). Multiwavelength properties of a new Geminga-like pulsar: PSRJ2021+4026. *Monthly Notices of the Royal Astronomical Society*, 405:1339–1348.

Uchida, H., Tsunemi, H., Katsuda, S., Mori, K., Petre, R., and Yamaguchi, H. (2012). A Suzaku Study of Ejecta Structure and Origin of Hard X-Ray Emission in the Supernova Remnant G156.2+5.7. *Publications of Astronomical Society of Japan*, 64:61.

Uchiyama, Y., Takahashi, T., Aharonian, F. A., and Mattox, J. R. (2002). ASCA View of the Supernova Remnant γ Cygni (G78.2+2.1): Bremsstrahlung X-Ray Spectrum from Loss-flattened Electron Distribution. *The Astrophysical Journal*, 571:866–875.

Ueda, Y. (1999). Results from X-ray Surveys with ASCA. *ArXiv Astrophysics e-prints*.

van den Bergh, S. (1960). An Optical Search for Possible Supernova Remnants. *Zeitschrift fuer Astrophysik*, 51:15.

Voelk, H. J. (2006). Shell-type Supernova Remnants. *ArXiv Astrophysics e-prints*.

Voges, W., Aschenbach, B., Boller, T., Bräuninger, H., Briel, U., Burkert, W., Dennerl, K., Englhauser, J., Gruber, R., Haberl, F., Hartner, G., Hasinger, G., Kürster, M., Pfeffermann, E., Pietsch, W., Predehl, P., Rosso, C., Schmitt, J. H. M. M., Trümper, J., and Zimmermann, H. U. (1999). The ROSAT all-sky survey bright source catalogue. *Astronomy and Astrophysics*, 349:389–405.

Weisskopf, M. C., Swartz, D. A., Carramiñana, A., Carrasco, L., Kaplan, D. L., Becker, W., Elsner, R. F., Kanbach, G., O'Dell, S. L., and Tennant, A. F. (2006). A Search for the X-Ray Counterpart of the Unidentified γ-Ray Source 3EG J2020+4017 (2CG078+2). *The Astrophysical Journal*, 652:387–400.

Wielebinski, R. (2002). The Characteristics of (Normal) Pulsars. In Becker, W., Lesch, H., and Trümper, J., editors, *Neutron Stars, Pulsars, and Supernova Remnants*, page 167.

Willis, A. G. (1973). Erratum; Observations of Galactic Supernova Remnants at 1.7 and 2.7 GHz. *Astronomy and Astrophysics*, 27:483.

Willis, A. G. and Dickel, J. R. (1971). The Radio Source CTB 1. *Astrophysics Letters*, 8:203–207.

Wilson, R. W. and Bolton, J. G. (1960). A Survey of Galactic Radiation at 960 Mc/s. *Publications of the ASP*, 72:331.

Woltjer, L. (1972). Supernova remnants. *Annual Review of Astronomy and Astrophysics*, 10(1):129–158.

Wu, J., Clark, C. J., Pletsch, H. J., et al. (2018). The Einstein@Home Gamma-ray Pulsar Survey. II. Source Selection, Spectral Analysis, and Multiwavelength Follow-up. *The Astrophysical Journal*, 854:99.

Yakovlev, D. G., Gnedin, O. Y., Gusakov, M. E., Kaminker, A. D., Levenfish, K. P., and Potekhin, A. Y. (2005). Neutron star cooling. *Nuclear Physics A*, 752:590–599.

Yao, J. M., Manchester, R. N., and Wang, N. (2017). A New Electron-density Model for Estimation of Pulsar and FRB Distances. *The Astrophysical Journal*, 835:29.

Zhang, S.-B., Dai, S., Hobbs, G., Staveley-Smith, L., Manchester, R. N., Russell, C. J., Zanardo, G., and Wu, X.-F. (2018). Search for a radio pulsar in the remnant of supernova 1987A. *Monthly Notices of the Royal Astronomical Society*, 479:1836–1841.

Zhu, Y.-S. (2008). On Statistical Significance of Signal. *ArXiv e-prints*.

Zyuzin, D. A., Karpova, A. V., and Shibanov, Y. A. (2018). X-ray counterpart candidates for six new γ-ray pulsars. *Monthly Notices of the Royal Astronomical Society*, 476:2177–2185.